From Periodic to Dilute Anderson Models

Inaugural-Dissertation

zur

Erlangung des Doktorgrades

der Mathematisch-Naturwissenschaftlichen Fakultäit

der Universität zu Köln

vorgelegt von

Lucas Hollender

aus Köln

Köln 2012

Abstract

Actinide- and Lanthanide based compounds are often considered as heavy Fermion (HF) systems. The essential ingredient for these systems is a localized d- or f-shell electron per lattice site which hybridizes with a non-interacting conduction band of p- or d-shell electrons. For temperatures below the so called coherence temperature T_c, the localized electrons stop to act like magnetic scatterers known from the Kondo effect. There the conduction band electrons screen the local magnetic moments coherently. As a main effect the conduction electrons build a Fermi liquid (FL) of quasiparticles with strongly enhanced masses which exceed 10-1000 times the mass of the original electrons. These enhancements can be seen experimentally in an increased heat capacity coefficient and Pauli susceptibility.

In this work we employ the periodic Anderson model (PAM) to describe the paramagnetic phase of the heavy Fermion compounds. To solve the complicated many body problem the dynamical mean-field theory is adopted with the numerical renormalization group technique as impurity solver.

We find that for low conduction band fillings T_c decreases drastically, which is in accordance with the exhaustion effect predicted by Nozières [5]. Additionally we find, that the form of the free conduction band density of states is decisive to obtain a FL or a Mott insulating (MI) phase for strongly depleted conduction band fillings.

Furthermore we investigate the PAM on a bipartite lattice, the coherence temperatures for each sublattice and especially the case of vanishing hybridization for one sublattice. In the latter case the system resembles a conduction band with only half the localized moment sites coupled to it. Our results show that it depends strongly on the chosen parameters if there is only one scale for the whole lattice or two distinct scales for each sublattice. Especially decoupling one sublattice leads to two separated scales.

In the last part the attention is focused on the two-impurity Anderson model and its solution via the DMFT method. We investigate the Anderson model and compare results to direct NRG calculations. Importantly, the two-impurity DMFT method can be easier extended to multi-impurity systems than the NRG on its own. This might lead to a method to efficiently examine multi-impurity systems.

Kurzzusammenfassung

Materialien, die auf Elementen der Actinoide und Lanthanoide basieren, bezeichnet man häufig als schwere Fermionen (HF) Systeme. Im wesentlichen sind dafür die in einem dichten Gitter angeordneten lokalisierten d- oder f-Schalen Elektronen verantwortlich, welche mit einem wechselwirkungsfreien Leitungsband aus p- oder d-Schalen Elektronen hybridisieren. Unterhalb einer bestimmten Temperatur, der sogenannten Kohärenztemperatur T_c, hören die lokalisierten Elektronen auf sich wie magnetische Streuquellen zu verhalten, ähnlich wie man es vom Kondo Effekt her kennt. Hier fangen die Leitungsbandelektronen an die lokalen magnetischen Momente kohärent abzuschirmen. Einer der wesentlichsten folgen daraus ist, dass die Leitungsbandelektronen eine Fermi Flüssigkeit (FL) aus Quasiteilchen mit stark erhöhten Massen bilden, welche das 10-1000-fache der Elektronenmasse übersteigen können. Experimentell kann man diese erhöhten Quasiteilchenmassen an einem vergrößerten Koeffizienten der Wärmekapazität oder einer erhöhten Pauli Suszeptibilität nachweisen.

Wir verwenden das periodische Anderson Modell (PAM) um die paramagnetische Phase von schweren Fermionenverbindungen zu beschreiben. Um dieses komplexe Vielteilchenproblem zu lösen setzen wir die dynamische Mean-Field Theorie (DMFT) ein, wobei die numerische Renormierungsgruppenmethode zum lösen des dabei entstehenden Störstellenproblems genutzt wird.

Wir werden sehen das für niedrige Leitungsbandfüllungen T_c drastisch sinkt, was mit dem sogenannten Exhaustion-Effekt im Einklang steht, der von Nozières [5] geprägt wurde. Außerdem finden wir, dass die funktionale Form der Zustandsdichte des freien Leitungsbandes eine entscheidende Rolle dabei spielt ob wir eine FL oder eine Mott-Isolator (MI) Phase für ein stark entleertes Leitungsband finden.

Des weiteren untersuchen wir das PAM auf einem bipartiten Gitter, die Kohärenztemperaturen für die einzelnen Untergitter und insbesondere den Fall einer verschwindenden Hybridisierung auf einem der Untergitter. Im letzteren Fall entspricht das System einem Leitungsband, an welchem nur noch die Hälfte der lokalisierten Momente koppeln. Unsere Ergebnisse zeigen, dass es stark von der Wahl der Parameter abhängt, ob nur eine Energieskala für das gesamte System existiert oder ob zwei verschiedene Skalen für die jeweiligen Untergitter existieren. Insbesondere das Entkoppeln eines Untergitters führt

zu einer Trennung der Energieskalen.

Im letzten Kapitel untersuchen wir das Zwei-Impurity Anderson Modell mithilfe der DMFT. Wir vergleichen diese Ergebnisse mit direkten Rechnungen der NRG. Hierbei ist von besonderer Bedeutung, dass sich die DMFT leichter auf Multi-Impurity Systeme ausdehnen lässt als die NRG. Dies führt womöglich zu einer Methode mit der sich Mulit-Impurity Systeme effizient untersuchen lassen.

Contents

1. Introduction

One of the most exciting problems for Condensed matter physicists for more than 30 years has been to understand the rich physics of the heavy Fermion (HF) compounds. They are a paradigm of strongly correlated systems and show a plethora of different low temperature phases, such as paramagnetic heavy Fermi liquid- or non-Fermi liquid phases, different kinds of long-range magnetic order, unconventional superconductivity or coexistent magnetism and superconductivity, which goes beyond the BCS theory of superconductivity.

The interest in HF compounds began in 1975, when Andres, Graebner and Ott [1] discovered enormous magnitudes of the specific heat in $CeAl_3$. This large specific heat coefficient stems from a huge quasiparticle mass which is up to 1000 times the mass of the bare electrons. Therefore the term "heavy Fermions" was coined by Steglich, Aarts et al. [2] in 1976. It was realized that the HF compounds usually consist of actinide- and lanthanide based compounds with partially filled 4f- or 5f-shells. The localized spin-$\frac{1}{2}$ electrons of the inner f-shell hybridize with the electrons of the conduction band and thus build a dense lattice version of the single impurity Anderson model (SIAM) which shows for a half filled f-band and a localized spin the well known Kondo effect [3, 4]. The local moment develops due to the strong Coulomb interaction between two f-electrons at the same impurity site. Therefore materials which show the Kondo effect, and thus also the HF compounds, belong to the class of strongly correlated electron systems.

The Kondo effect describes the physics of a single localized spin-$\frac{1}{2}$ moment coupled to a conduction band. For high temperatures the spin is free and we find a Curie magnetic susceptibility, whereas for low temperatures the spin gets screened by the conduction band electrons and just acts as a spinless scattering center. The crossover from the free local moment state at high temperatures to the screened state at much lower temperatures is continuous and occurs at a characteristic, exponentially small energy scale T_K, the so called Kondo scale. Below T_K the screened moment acts as a strong potential scatterer and thus

gives rise to an increased resistivity.

In the case of the HF compounds, the local moments are dense but can still be coherently screened at a temperature much lower than the Kondo temperature, the so called coherence scale T_c. The metallic behaviour below T_c can be described within the Fermi liquid (FL) theory with effective quasiparticles which have the same behaviour and quantum numbers as the original electrons but with a strongly increased quasiparticle mass. But Nozières [5] raised the question whether the local moments can still be screened in the case of low conduction band filling, especially in the case where the number of f-band electrons is much larger than the number of conduction band electrons, because then there might be not enough conduction band electrons to screen all local moments. This is known as the exhaustion problem. Nozières argued [5, 6] then that the local moments can still be screened by the conduction electron spins but with a reduced coherence scale for low fillings. His phenomenological estimate relates the coherence scale with the Kondo scale, $T_c \propto T_k^2/\rho(0)$, with $\rho(0)$ the bare density of states at the Fermi energy.

The thesis is structured as follows:

The next chapter, Chap. 2, introduces impurity physics, the single impurity Anderson model (SIAM) and the numerical renormalization group (NRG) method as a numerically exact tool to solve the SIAM.

In Chap. 3 first the periodic Anderson model (PAM) is introduced, which is assumed to capture the main physics of the paramagnetic heavy Fermi liquid phase of the HF materials. Then the dynamical mean-field theory (DMFT) is introduced, which is used to solve this model in the paramagnetic phase.

In Chap. 4 the Mott metal-insulator transition and its possible connection to the exhaustion effect in the PAM is studied within the DMFT. We investigate the coherence scale upon vanishing conduction band filling while the filling of the f-orbitals is kept fix. We also inspect the influence of the bare density of states on the coherence scale.

Chap. 5 is concerned about the PAM with a bipartite hypercubic lattice structure. The main interest is the development of the coherence scale upon reducing the hybridization between the local magnetic moments and the conduction band electrons on one of the sublattices. In the extreme case of a vanishing hybridization the system represents a diluted system with half the number of magnetic ions. This represents the first step in diluting the system until it becomes a SIAM and is associated with the question how the coherence scale evolves from the PAM to the SIAM.

In the last part, Chap. 6, our focus turns, in principle, to systems with multiple magnetic moments, which contrasts the idea of the previous chapter. Namely we investigate the development of the Kondo scale upon increasing the number of impurities in the system. The idea is to perform DMFT calculations for n-impurity Anderson models. The DMFT calculations will be compared to exact NRG results and it will be discussed if it is a proper approximation to treat multi-impurity systems within DMFT.

2. Kondo effect

2.1. Metals at extremely low temperatures

In the beginning of the last century most physicists where convinced that for vanishing temperatures metals show a monotonically decreasing resistivity because it is dominated by phonon scattering which rapidly decreases for low temperatures ($\propto T^5$). But in 1934 de Haas et al. [11] found a resistance minimum in gold, which could not be explained for the following 30 years (Fig. 2.1 a)). It was realized that 3d transition metal residues such as Fe are responsible for the experimental results, since the temperature where the minimum occurs does change upon varying the impurity concentration with $T_{min} \propto n_{imp}^{\frac{1}{5}}$ and a resistance minimum is accompanied by a Curie-Weiß behaviour in the susceptibility (Fig. 2.1 b)). Thus the term impurity physics emerged.

2.2. Single impurity Anderson model

In 1961 Anderson [12] put forward the Anderson impurity model (also known as single impurity Anderson model (SIAM)) where he modeled the gold with a non-interacting conduction band and the 3d transition metal ions as independent magnetic impurities. It is assumed that the electrons in the conduction band have extended wave functions such that their Coulomb interaction is screened and can be absorbed into an effective dispersion. The resulting quasiparticles behave like electrons with short range interactions and the interactions are neglected. The d-electrons of the impurities (in lanthanide and actinide based compounds the f-electrons) are closer to the nucleus, have short ranged wave functions and thus the Coulomb interaction plays a crucial role. In second quantized form the Hamiltonian Anderson considered is

$$H = \sum_{\mathbf{k},\sigma} \left(\varepsilon_{\mathbf{k}} - \mu \right) c_{\mathbf{k}\sigma}^{\dagger} c_{\mathbf{k}\sigma} + \sum_{\sigma} \varepsilon^f n_{\sigma}^f + U n_{\uparrow}^f n_{\downarrow}^f + \sum_{\mathbf{k}\sigma} \left(V_{\mathbf{k}} f_{\sigma}^{\dagger} c_{\mathbf{k}\sigma} + V_{\mathbf{k}}^* c_{\mathbf{k}\sigma}^{\dagger} f_{\sigma} \right),$$
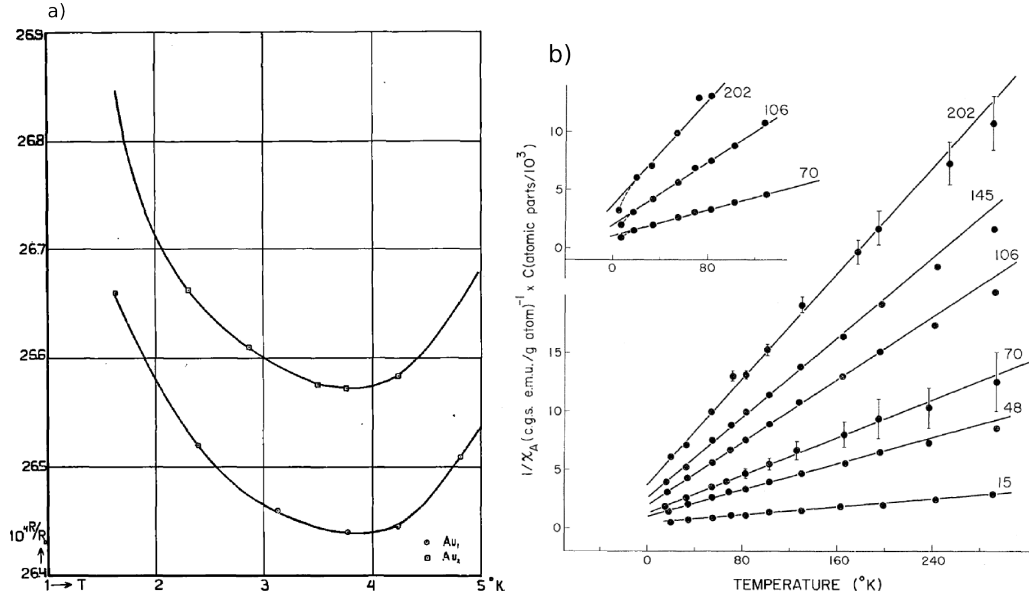
$$(2.1)$$

Figure 2.1.: Figure a) shows the resistivity in gold as a function of temperature with an unpredicted upturn for low temperatures measured by de Haas et al. [11]. The two curves correspond to two different resistances deriving from a small deformation in one of the wires. Figure b) depicts a Curie-Weiß behaviour for the susceptibility of iron alloyed copper in ppm as indicated at the curves. The inset shows small deviations at very low temperatures. Measured by Hurd [19].

where $f_\sigma^{(\dagger)}$ are the annihilation (creation) operators for an electron at the impurity site with spin σ, $n_\sigma^f = f_\sigma^\dagger f_\sigma$ is the particle number operator for the impurity, $c_{\mathbf{k}\sigma}^{(\dagger)}$ the annihilation (creation) operator for an electron with momentum $\mathbf{k}$ and spin σ in the conduction band. $\varepsilon_{\mathbf{k}}$ is the dispersion and μ the chemical potential of the conduction band; ε^f the on-site energy for an electron on the impurity site and $V_{\mathbf{k}}$ is the tunneling matrix element between the impurity and the conduction band which allows electron hopping to and from the impurity site. U is the Coulomb interaction energetically penalizing double occupancy of the impurity site.

For zero or double occupancy the impurity site contributes just as potential scattering center which leads to a finite and essentially temperature independent low temperature conductivity. This effect can not explain the resistance minimum in Fig. 2.1. The more important case is where the impurity is singly occupied, such that it acts as a magnetic moment. To expose the low energy features in the spinful case it is useful to write down an effective theory. This can be achieved by the Schrieffer-Wolf (SW) [13] transformation, which projects the Anderson Hamiltonian onto a Hamiltonian, which is singly occupied. Excitations into empty or doubly occupied states are treated in second

order perturbation theory in the hybridization, so called virtual excitations. More detailed information can be found in [14]. For half filling, i.e. $\varepsilon^f = -\frac{U}{2}$, single occupancy $|\varepsilon_{\mathbf{k}}| \ll |\varepsilon_F - \varepsilon^f|$ and $|\varepsilon_{\mathbf{k}}| \ll |\varepsilon_F - \varepsilon^f - U|$ and assuming the hybridization to be momentum independent and real, i.e. $V_{\mathbf{k}} = V$, the SIAM reduces to the famous Kondo model

$$H = \sum_{\mathbf{k},\sigma} \varepsilon_{\mathbf{k}} c_{\mathbf{k}\sigma}^{\dagger} c_{\mathbf{k}\sigma} + J\,\mathbf{S} \cdot \mathbf{s}(\mathbf{r} = 0), \tag{2.2}$$

with

$$\varepsilon_F \text{ the Fermi energy,}$$

$$J = \frac{V^2}{U},$$

$$\mathbf{S} = \sum_{\sigma\sigma'} f_{\sigma}^{\dagger} \boldsymbol{\sigma}_{\sigma\sigma'} f_{\sigma'} \text{ and}$$

$$\mathbf{s}(\mathbf{r} = 0) = \frac{1}{2} \sum_{\mathbf{k}\mathbf{k}'\sigma\sigma'} c_{\mathbf{k}\sigma}^{\dagger} \boldsymbol{\sigma}_{\sigma\sigma'} c_{\mathbf{k}'\sigma'}.$$

Here $\sigma_{\mu,\nu}$ are the components of the Pauli matrices. One important fact is that the virtual excitations lead to an effective antiferromagnetic coupling J.

Kondo [4] assumed that the impurity concentration is small enough such that the impurities have no influence on each other and extended the calculation of the resistivity for the Kondo model to third order perturbation theory in J. He found the resistivity increasing logarithmically for vanishing temperature

$$R_{mag}(T) \propto n_{imp} J^2 \left[1 + 2J\rho_0(\varepsilon_F) \ln\left(\frac{D}{k_B T}\right) \right],$$

where $\rho_0(\varepsilon_F)$ is the conduction band density of states at the Fermi energy ε_F, n_{imp} the impurity concentration, D the bandwidth and k_B the Boltzmann constant.

Combining the phonon scattering effect to the resistivity $R_{phonon} \propto T^5$ and the scattering effect from the magnetic impurity $R_{mag}(T) = n_{imp} R_0 + n_{imp} R_1 \ln\left(\frac{D}{k_B T}\right)$, Kondo was able to explain the resistance minimum in systems with small amounts of impurities. Although these results explain the resistance minimum very well, it is not consistent with experiments for very low temperatures where a saturation of the resistance was found. In contrast, the theoretical result predicted a divergent resistivity for $T \to 0$. Calculation of thermodynamic properties as the susceptibility, entropy or specific heat revealed that perturbation theory breaks down when the logarithm becomes of

the order of one, i.e.

$$2J\rho_0(\varepsilon_F)\ln\left(\frac{D}{k_B T_K}\right) \approx \mathcal{O}(1)$$

$$\Rightarrow T_K := \frac{D}{k_B}e^{-\frac{1}{2J\rho_0(\varepsilon_F)}}, \tag{2.3}$$

which defines the Kondo temperature T_K. The unphysical divergences below the Kondo temperature became known as the Kondo problem. Attempts to incorporate higher order terms in perturbation theory could not solve this issue.

There have been numerous attempts to overcome the problem with the logarithmic divergence. In the following we want to concentrate on the renormalization group and the numerical renormalization group method to solve the Kondo problem. For a survey of methods being used to solve the Kondo model or the SIAM see e.g. [14] and [15] chapter 2.3.

In the next section the renormalization group concept is discussed and within this context the solution of the Kondo problem will be explained.

2.3. Concept of the Renormalization Group technique

Here we want to introduce just the general idea of the renormalization group (RG) concept. Later on we give a more profound introduction to the numerical renormalization group technique, which is employed as impurity solver for the dynamical mean-field theory introduced in Chap. 3.

Concept of the Renormalization Group

The renormalization group (RG) approach in condensed matter physics was largely put forward by Wilson in the beginning of the 1970s [16].

The basic idea of the RG is easy to grasp but is mathematically involved. E.g. for critical phenomena in thermodynamic systems one is usually interested in the systems behaviour on large length scales and in quantities no longer depending on all the microscopic parameters. Large length scales mean also long wavelength whereas the short range fluctuations are of no interest. The goal is to incorporate the high energy states into an effective low energy theory. Thus the idea is to define some cutoff parameter $\Lambda > 1$ and integrate out the high energy degrees of freedom at the band edges $[-D, -D\Lambda^{-1}]$

and $[D\Lambda^{-1}, D]$ to determine an effective Hamiltonian depending on effective parameters. Successive repetition of this procedure with the reduced energy band keeps track of the influence of the high energy states on the low energy properties of the model and produces an effective low energy Hamiltonian. In more mathematical terms the RG is a mapping

$$R_\Lambda\{H(\mathbf{K})\} = H(\mathbf{K}')$$

which maps a Hamiltonian, depending on parameters $\mathbf{K} = (K_1, \ldots, K_n)$, onto an equivalent Hamiltonian with renormalized parameters $\mathbf{K}' = (K_1', \ldots, K_n')$. The index Λ determines the change in length scale from one RG step to the next. Despite its name, the renormalization group mapping does not build a group but a semi-group since there exists no inverse element, more precisely due to the integration we lose the detailed information of the high energy states.

A key concept of the RG is that of fixed points (FP), i.e. points $\mathbf{K}^*$ which are invariant under the RG flow

$$R_\Lambda\{H(\mathbf{K}^*)\} = H(\mathbf{K}^*).$$

Except the case where one is exactly at a FP, each RG step changes the couplings, i.e. repeated RG mapping will by definition lead to a flow of the coupling constants. Depending on the flow in the vicinity of a fixed point they can be classified in three categories:

1. Stable fixed points: Fixed points where all flows are directed towards the FP. These FPs represent stable phases of matter, because when the system is released in the vicinity of such a FP it will always flow to the fixed point. E.g. the paramagnetic phase of a Heisenberg model at high Temperatures.

2. Unstable fixed points: Fixed points where all flows are directed away. These are ideal fixed points, which cannot be reached, i.e. zero temperature FPs.

3. Marginal fixed points: FPs where there exist some couplings flowing towards and others away from the fixed point. These FPs are related to phase transitions and thus are the most important ones.

For further details on the general concept and explicit application of the renormalization group see e.g. [7] chapter 8 or [16, 17].
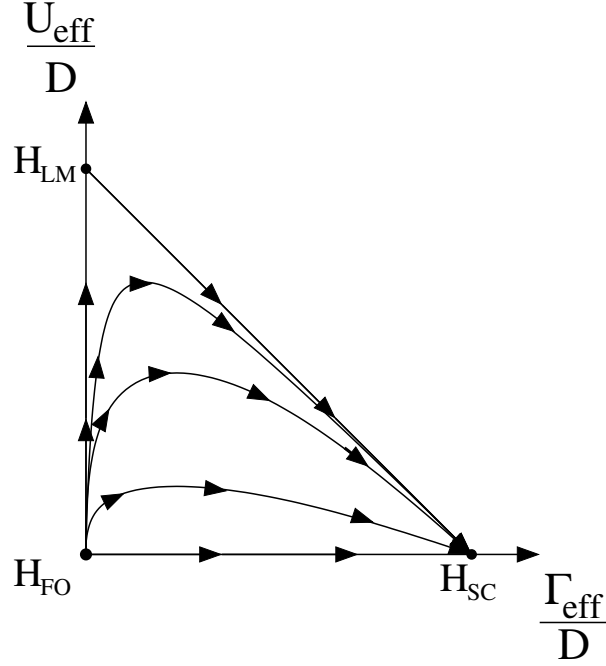
Figure 2.2.: RG flow of the coupling constants for the symmetric SIAM. With $\Gamma_{eff} = \pi V_{eff}^2 \rho(\varepsilon^f)$, H_{FO} the free orbital fixed point (FP), H_{LM} the local moment FP and H_{SC} the strong coupling FP. Figure from Krishna-murthy et al. [18].

RG results for the SIAM

Figure 2.2 shows the flow diagram for the symmetric SIAM calculated by Krishna-murthy et al. [18]. U_{eff} and $\Gamma_{eff} = \pi \rho_0(\varepsilon_F) V_{eff}^2$ are the effective couplings, D is the band width of the conduction band and $\rho_0(\varepsilon_F)$ is the bare density of states of the conduction band at the Fermi energy ε_F. The flow diagram shows three distinct fixed points:

H_{FO} : At high energies the symmetric SIAM is close to the free orbital FP. In this case the effective Coulomb interaction and hybridization are zero, $\tilde{U} = \tilde{V} = 0$, and the impurity is decoupled from the conduction electrons. The symmetry of the model requires $2U + \varepsilon^f = 0 \rightarrow \varepsilon^f = U = 0$ such that the impurity site is four-fold degenerate ($|0\rangle$, $|\uparrow\rangle$, $|\downarrow\rangle$, $|\uparrow\downarrow\rangle$) and shows a local entropy of $S = 2\ln(2)$.

H_{LM} : Lowering the temperature starting out from high energies for $U > \pi V \rho_0(\varepsilon_F)$, the local moment FP is approached at intermediate temperatures. This point corresponds to a SIAM with effective couplings $\tilde{V} \rightarrow 0$ and $\tilde{U} \rightarrow \infty$ and due to half filling the impurity site is thus occupied with exactly one electron. This case realizes the Kondo model with a local moment interacting with the bath only via virtual magnetic scattering

processes. A Shrieffer-Wolff transformation gives the effective coupling $\tilde{J} = \frac{4|\tilde{V}^2|}{\tilde{U}}$. The spin at the impurity site can be $|\uparrow\rangle$ or $|\downarrow\rangle$, thus the local entropy is given by $S = \ln(2)$.

H_{SC} : At lowest temperatures, $T \ll T_K$, the system always flows to the strong coupling FP. In this case the effective couplings approach $\tilde{U} \to 0$ and $\tilde{V} \to \infty$. Due to the strong hybridization, or after a Shrieffer-Wolff transformation due to a strong antiferromagnetic coupling $\tilde{J}$, the spin at the impurity induces a many body 'Kondo singlet' state with the conduction electrons such that the local moment is effectively screened. The Kondo singlet is associated with a cloud of conduction electrons which screen the impurity, the 'Kondo screening cloud'. Since only electrons within the range of $k_B T_K$ around the Fermi energy can participate in the local moment screening, the length scale associated with the Kondo cloud is $\xi_K = \frac{\hbar v_F}{k_B T_K}$. Here v_F is the Fermi velocity and k_B the Boltzmann constant. Given that a singlet state has evolved, the entropy at the impurity site is zero, $S = \ln(1)$ and the resulting non-magnetic singlet acts as a potential scatterer. The potential scattering yields a finite resistivity and a local Fermi-liquid which solves the Kondo problem. At this point universality sets in since T_K is the only relevant energy scale.

2.4. Numerical Renormalization Group

The numerical renormalization group (NRG) method was developed by Wilson [16] in 1975 to calculate static quantities for the Kondo model, e.g. entropy or magnetic susceptibility. In 1980 the NRG was extended to also incorporate the SIAM by Krishna-murthy et al. [18, 20]. Later on physicists improved the NRG method to calculate dynamic quantities as spectral functions, Green functions, etc. at zero temperature [21, 22, 23] and also for finite temperatures [24]. Literature for more recent developments of the NRG can be found in the review article by Bulla et al. [25]. Its most important advantage is that it is non-perturbative in all system parameters and it incorporates all energies from the band edges down to exponentially small energies. But the price to pay is that the calculations can only be performed numerically and it is very demanding to include multi-orbital physics, multi-impurity physics or increase the number of independent bath's coupled to the impurities. It should also be mentioned that due to the logarithmic discretization it is much more difficult

to obtain accurate high temperature results than for low temperatures.

The general procedure of the NRG consists of four main steps:

1. Its starting point is a logarithmic discretization of the conduction band to incorporate all energy scales. Assuming a bandwidth of $2W$, a discretization parameter $\Lambda > 1$ is introduced, such that the band is divided into $2n$ intervals of decreasing width $\left[-\Lambda^{-n}W, -\Lambda^{-(n+1)}W\right]$ and $\left[\Lambda^{-(n+1)}W, \Lambda^{-n}W\right]$.

2. The second step is to map the impurity Hamiltonian onto a semi-infinite chain Hamiltonian with the first site represented by the impurity.

3. In the third step of the NRG the semi-infinite chain is diagonalized iteratively, i.e. the impurity coupled to the first site of the conduction band is diagonalized, then the next site is coupled to the diagonalized system and so on. Since the Hilbert space is growing exponentially, it is truncated and only a certain number of lowest-lying many-particle states are kept. This approximation is justified, because the logarithmic discretization of the conduction band gives rise to an exponential fall off of the hopping parameters along the semi-infinite chain and allows for a clear separation of the energy scales.

4. In the last step the calculated eigenenergies and matrix elements are used to determine static and dynamic properties of the impurity system.

Let us give an idea of how to work out the aforementioned steps. For more information and further description we refer to the original work of Wilson and Krishna-murthy et al. [16, 18, 20] or the review article by [25].

Logarithmic discretization

The Hamiltonian for a general impurity model has the form

$$H = H_{imp} + H_{bath} + H_{hyb},$$

where H_{imp} describes the impurity degrees of freedom, H_{bath} a non-interacting bath and H_{hyb} the coupling between the impurity and the bath. We will consider the SIAM only (see Eq. 2.1) because it serves as impurity solver for

the DMFT,

$$H_{imp} = \sum_\sigma \varepsilon^f f_\sigma^\dagger f_\sigma + U f_\uparrow^\dagger f_\uparrow f_\downarrow^\dagger f_\downarrow,$$

$$H_{bath} = \sum_{\mathbf{k},\sigma} \left(\varepsilon_{\mathbf{k}} - \mu \right) c_{\mathbf{k}\sigma}^\dagger c_{\mathbf{k}\sigma} \quad \text{and}$$

$$H_{hyb} = \sum_{\mathbf{k},\sigma} \left(V_{\mathbf{k}} f_\sigma^\dagger c_{\mathbf{k}\sigma} + V_{\mathbf{k}}^* c_{\mathbf{k}\sigma}^\dagger f_\sigma \right).$$

Usually the hybridization $V_{\mathbf{k}}$ is assumed to be real valued and momentum independent. For the NRG only the impurity physics is of interest, i.e. to proceed, the bath degrees of freedom are integrated out. This leads to the hybridization function

$$\Delta(\omega) = \pi \sum_{\mathbf{k}} |V_{\mathbf{k}}|^2 \delta(\omega - \varepsilon_{\mathbf{k}}) = \pi V^2 \rho(\omega),$$

which gives a full description of the influence of the bath on the impurity physics. Here $\rho(\omega) = \sum_{\mathbf{k}} \delta(\omega - \varepsilon_{\mathbf{k}})$ is the bare density of states of the conduction band. For convenience, the band width is set to $[-1, 1]$, i.e. $W = 1$. Then, as already mentioned, the interval is divided logarithmically with a discretization parameter $\Lambda > 1$ into shrinking intervals $\left[-\Lambda^{-n}, -\Lambda^{-(n+1)} \right]$ and $\left[\Lambda^{-(n+1)}, \Lambda^{-n} \right]$ with $n \in \mathbb{N}$, see Fig. 2.3 (a).

Discretization of the conduction band and the semi-infinite chain

For the mapping of the SIAM onto a semi-infinite chain it is useful to write down an energy representation of the SIAM Hamiltonian,

$$H = H_{imp} + \sum_\sigma \int_{-1}^{1} d\varepsilon \, g(\varepsilon) a_{\varepsilon\sigma}^\dagger a_{\varepsilon\sigma} + \sum_\sigma \int_{-1}^{1} d\varepsilon \, h(\varepsilon) (f_\sigma^\dagger a_{\varepsilon\sigma} + a_{\varepsilon\sigma}^\dagger f_\sigma), \quad (2.4)$$

where $g(\varepsilon)$ and $h(\varepsilon)$ are related by

$$\Delta(\omega) = \pi \frac{d\varepsilon}{d\omega} h[d\varepsilon(\omega)]^2 \quad \text{and} \quad g[\varepsilon(\omega)] = \omega \quad (2.5)$$

and $a_{\varepsilon\sigma}^\dagger$ and $a_{\varepsilon\sigma}$ are fermionic operators. The functions $\varepsilon(\omega)$ and $h[\varepsilon(\omega)]$ are not unique but have to be chosen such that they fulfill Eq. 2.5 (see Bulla et al. [26]).

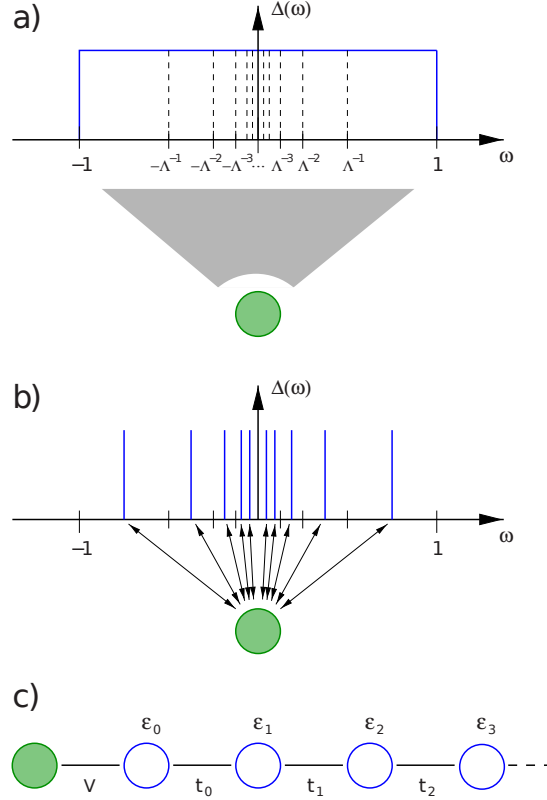Introducing a complete set of orthonormal functions in each interval n,

Figure 2.3.: The Figures illustrate the first steps of the NRG for the SIAM, where an impurity, filled circle, is coupled to a continuous conduction band via the hybridization function $\Delta(\omega)$: a) logarithmic discretization of the band via a discretization parameter $\Lambda > 1$, b) introduction of discrete states approximating the continuous spectrum and c) mapping of the discretized spectrum onto a semi-infinite chain with ε_n the on-site energies and t_n are the hoppings of the corresponding tight-binding model. Figure taken from [25].

$\psi^\pm_{np}(\varepsilon)$, the conduction band operators can be rewritten as

$$a_{\varepsilon\sigma} = \sum_{np} \left[a_{np\sigma} \psi^+_{np}(\varepsilon) + b_{np\sigma} \psi^-_{np}(\varepsilon) \right] \quad \text{with}$$

$$\psi^\pm_{np}(\varepsilon) = \begin{cases} \frac{1}{\sqrt{d_n}} e^{\pm i\omega_n p\varepsilon}, & \text{for } x_{n+1} < \pm\varepsilon < x_n \\ 0, & \text{else} \end{cases},$$

$$x_n = \pm\Lambda^{-n}, n \in \mathbb{N}, \ d_n = \Lambda^{-n}(1 - \Lambda^{-1}), p \in \mathbb{Z} \quad \text{and} \quad \omega_n = 2\pi/d_n.$$

The Hermitian conjugate operator $a^\dagger_{\varepsilon\sigma}$ is defined accordingly and the operators $a_{np\sigma}$, $b_{np\sigma}$, $a^\dagger_{np\sigma}$, $b^\dagger_{np\sigma}$ also fulfill the fermionic commutation relations.

By rewriting the Hamilton operator for the SIAM with the new operators, only the $p = 0$ terms are taken into account. This approximation is motivated by

(i) the $p \neq 0$ states are only coupled indirectly to the impurity via the $p = 0$ state,

(ii) the coupling between the $p = 0$ and the $p \neq 0$ states is reduced by $1 - \Lambda^{-1}$, such that in the limit $\Lambda \to 1$ the approximation can be assumed as a lowest order perturbation.

The resulting Hamiltonian has the form

$$
\begin{aligned}
H = H_{imp} &+ \sum_{n\sigma} \left(\xi_n^+ a_{n\sigma}^\dagger a_{n\sigma} + \xi_n^- b_{n\sigma}^\dagger b_{n\sigma} \right) \\
&+ \left[\frac{1}{\sqrt{\pi}} \sum_\sigma f_\sigma^\dagger \sum_n \left(\gamma_n^+ a_{n\sigma} + \gamma_n^- b_{n\sigma} \right) + h.c. \right],
\end{aligned} \tag{2.6}
$$

where the index for $p = 0$ has been skipped and $\xi_n^\pm$ and $\gamma_n^\pm$ are given in detail in [25]. We achieved to represent the SIAM Hamiltonian in a discretized form as depicted in Fig. 2.3 b).

To reduce oscillation effects in the thermodynamic expectation values, introduced by the discretization procedure, Oliveira and Oliveira [27] proposed a z averaging (or z-Trick). They supposed to use several discretization schemes with $x_n = \Lambda^{-n+z}$, $z \in [0, 1)$ and perform one NRG calculation for each z. The NRG results are then averaged to minimize the oscillation effects. It is especially interesting for $\Lambda \gg 1$, because in that case the number of discretization points is small and the artificial oscillation effects are stronger. Importantly, the z averaging is not the same as the continuum limit $\Lambda \to 1$.

Campo and Oliveira [28] introduced a renormalization of the hybridization function $\Delta(\omega)$

$$
\Delta(\omega) \to \frac{1}{2} \frac{\Lambda + 1}{\Lambda - 1} \ln(\Lambda) \Delta(\omega) \,,
$$

because in the discretized model $\Delta(\omega)$ is systematically underestimated.

As illustrated in Fig. 2.3 the next step is to perform a basis transformation to tridiagonalize (2.6) to a tight-binding Hamiltonian on a semi-infinite chain. The result is

$$
\begin{aligned}
H_{TD} = H_{imp} &+ \sqrt{\frac{\xi_0}{\pi}} \sum_\sigma \left(f_\sigma^\dagger c_{0\sigma} + c_{0\sigma}^\dagger f_\sigma. \right) \\
&+ \sum_{\sigma, n=0}^\infty \left[\varepsilon_n c_{n\sigma}^\dagger c_{n\sigma} + t_n \left(c_{n\sigma}^\dagger c_{n+1\sigma} + c_{n+1\sigma}^\dagger c_{n\sigma}. \right) \right],
\end{aligned} \tag{2.7}
$$

where ξ_0, the hopping t_n and on-site energies ε_n can be calculated numerically, for details see [29]. For a symmetric hybridization function all ε_n are zero and

for an additionally constant $\Delta(\omega)$ in the interval $[-1, 1]$ the hoppings are

$$t_n = \frac{\left(1 + \Lambda^{-1}\right)\left(1 - \Lambda^{-n-1}\right)}{2\sqrt{1 - \Lambda^{-2n-1}}\sqrt{1 - \Lambda^{-2n-3}}} \Lambda^{-n/2},$$

which in the limit of large n reduces to

$$t_n \to \frac{1}{2}\left(1 + \Lambda^{-1}\right)\Lambda^{-n/2},$$

see again Wilson [16].

The exponentially decreasing hopping strength with increasing distance from the impurity site is a general property of the NRG calculations and is important for the iterative diagonalization.

Iterative diagonalization

Starting with

$$H_0 = \Lambda^{-1/2}\left(H_{imp} + \sum_\sigma \varepsilon_0 c_{0\sigma}^\dagger c_{0\sigma} + \sqrt{\frac{\xi_0}{\pi}}\sum_\sigma \left(f_\sigma^\dagger c_{0\sigma} + h.c.\right)\right),$$

the Hamiltonian (2.7) can be defined iteratively via

$$
\begin{aligned}
H_{N+1} = {} & \sqrt{\Lambda} H_N + \Lambda^{N/2}\sum_\sigma \varepsilon_{N+1} c_{N+1\sigma}^\dagger c_{N+1\sigma} \\
& + \Lambda^{N/2}\sum_\sigma t_N \left(c_{N\sigma}^\dagger c_{N+1\sigma} + c_{N+1\sigma}^\dagger c_{N\sigma}\right),
\end{aligned}
\tag{2.8}
$$

with the identity

$$H_{TD} = \lim_{N \to \infty} H_N.$$

Beginning with the impurity coupled to the first site of the chain, we diagonalize the four state system. Then we adopt the iterative diagonalization scheme as depicted in Fig. 2.4:

We assume that we have a diagonal system H_N, consisting of the impurity coupled to N conduction band sites with basis $|r\rangle$. Then we add a further site $|s(N+1)\rangle$ along the chain and diagonalize the new system numerically. This procedure is repeated iteratively.

Fig. 2.5 shows the development of the eigenenergies of the Hamiltonians H_N with increasing chain length N. In (a) we have the diagonal system with discrete eigenenergies for H_N. For convenience, the ground state is chosen to be zero. Then (b) the energy levels are rescaled by $\sqrt{\Lambda}$ according to equation 2.8. In the following (c) the next site of the chain is added and diagonalized.
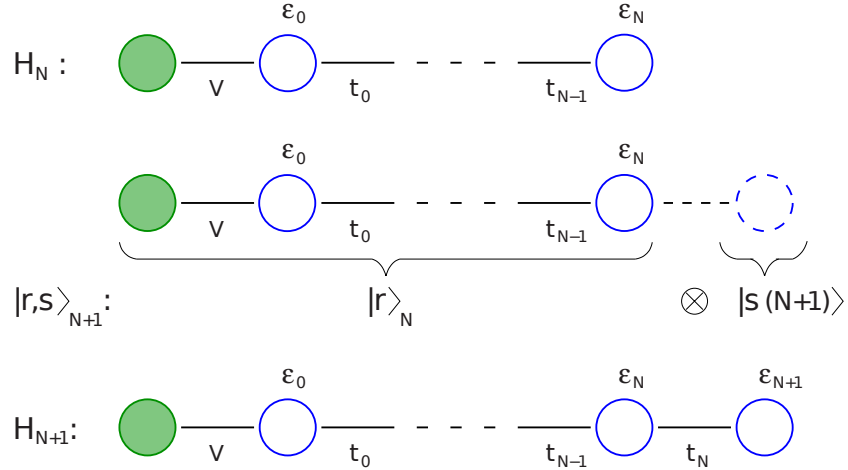
Figure 2.4.: The figure illustrates the iterative diagonalization. Starting from Hamiltonian H_N, it is diagonalized and the new basis is $|r\rangle$. The tensor product of $|r\rangle$ and the basis of the newly added site $|s(N+1)\rangle$ build the basis for the next step Hamiltonian H_N. Figure taken from [25].

Since the Hilbert space grows by a factor of four in each step and we have to diagonalize it numerically, a truncation scheme is needed (d), e.g. keeping only a certain number of eigenstates or keeping only the states up to a certain energy. The truncation is a valid approximation since each new site added to the chain comes with a prefactor $\Lambda^{-1/2}$ and can be seen as a small perturbation. So on the one hand Λ must not be to small, because then one has to keep to many eigenstates, on the other hand Λ must not be to large otherwise the approximation that only the $p = 0$ states are kept becomes erroneous. At last the ground state energy is again shifted to zero.

The whole procedure can be understood as a renormalization group transformation R, i.e.

$$H_{N+1} = R(H_N).$$

Example for an energy flow diagram

Fig. 2.6 shows the flow for the lowest-lying many-particle levels $E_N(r)$ for the SIAM during the iterative diagonalization. The NRG program therefore was provided by Priv.-Doz. Dr. Ralf Bulla. It keeps 500 states and uses 120 chain sites for the iterative diagonalization. The parameters for a) are $U = 0.001$, $\varepsilon = -U/2$, $V = 0.004$ and $\Lambda = 2$. Due to even-odd oscillations, which always appear in fermionic finite-size systems, the flow is shown only for odd iterations.
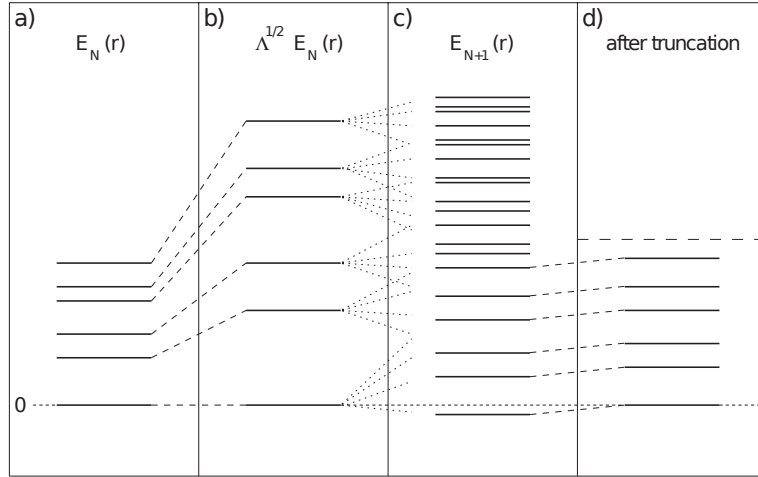
Figure 2.5.: Steps for the iterative diagonalization. (a) Many-particle spectrum in the N-th iteration, ground state set to zero, (b) rescaling of the spectrum Eq. 2.8, (c) adding the next site of the chain and diagonalization yields the spectrum $E_{N+1}(r)$ for next step, (d) truncation of the spectrum and shifting the ground state to zero again. Figure taken from [25].

The flow diagram exhibits three fixed points. The first fixed point (FP) is the free orbital FP for $N \lesssim 10$, the second FP between $15 \lesssim N \lesssim 40$ is the local moment FP, and the third FP above $N \sim 50$ is the strong coupling FP. Between these fixed points, i.e. $10 \lesssim N \lesssim 15$ and $40 \lesssim N \lesssim 50$, there is a crossover region. Using that each iteration step is related to a temperature, we can estimate the Kondo temperature $T_K \approx W\Lambda^{\bar{N}/2} = \Lambda^{\bar{N}/2}$ with $\bar{N} \approx 55$.

Fig. 2.6 b) shows the flow of the same energy levels, but with different parameters, $U = 0.0001$, $\varepsilon = -U/2$, $V = 0.004$ and $\Lambda = 3$. Here the diagram shows again the free orbital fixed point for $N \lesssim 10$. Differently here is a single but broad crossover region, $10 \lesssim N \lesssim 25$, directly to the strong coupling FP.

These two figures illustrate the two cases where in a) the flow of the couplings approximates the local moment FP before converging to the strong coupling FP while in b) the SC FP is approached directly, compare to Fig. 2.2.

Physical properties

Using the fact, that each iteration step corresponds to a energy scale given by $T \propto \Lambda^{-N/2}$ and assuming that enough energy states per iteration are kept, it is possible to calculate thermodynamic quantities. For example the impurity
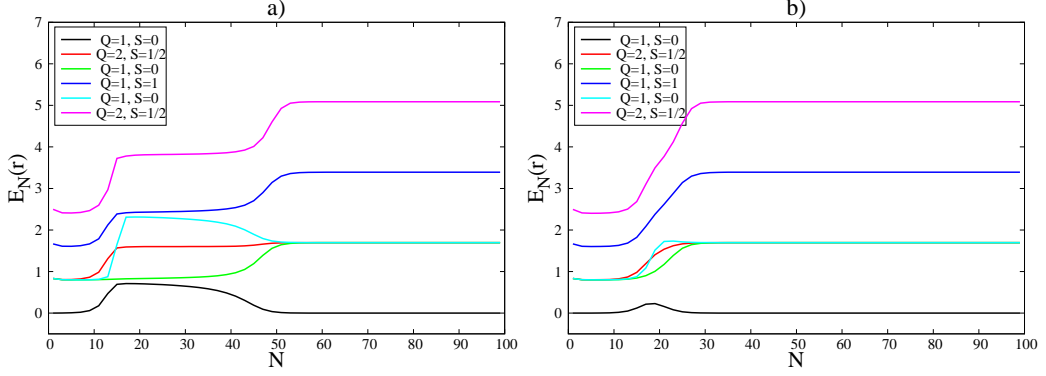
Figure 2.6.: Flow diagram for some of the lowest-lying many-particle levels of the SIAM for a) $U = 0.001$, $\varepsilon = -U/2$, $V = 0.004$ and $\Lambda = 2$ and b) $U = 0.0001$, $\varepsilon = -U/2$, $V = 0.004$ and $\Lambda = 2$. Q is the quantum number for the total charge and S for the total spin.

contribution to the entropy $S_{tot}(T)$ can be calculated via

$$S_{imp}(T) = S_{tot}(T) - S_{tot}^{(0)}(T)$$

$$S^{(N)}/k_B = \beta \left\langle H^{(N)} \right\rangle + \ln Z^{(N)} \quad \text{with the expectation value}$$

$$\langle \ldots \rangle^{(N)} = \frac{1}{Z^{(N)}} \sum_{Q,S_z,r} e^{-\beta E_N(Q,S_z,r)} {}_N \langle Q, S_z, r| \ldots |Q, S_z, r\rangle_N \quad \text{and} \quad (2.9)$$

$$Z^{(N)} = \sum_{Q,S_z,r} e^{-\beta E_N(Q,S_z,r)} .$$

$S_{tot}(T)$ is the entropy of the full system, $S_{tot}^{(0)}$ the entropy of the system without impurity, N is the iteration and thus indicates the temperature via

$$k_B T_N = \Lambda^{-(N-1)/2}/\bar{\beta} \tag{2.10}$$

with the Boltzmann factor k_B and $\bar{\beta}$ usually chosen $\sim \mathcal{O}(1)$. $\langle \ldots \rangle^{(N)}$ is the expectation value and $Z^{(N)}$ the partition function.

Some quantities require the calculation of local matrix elements, for example ${}_N \langle Q, S_z, r| f_\sigma^\dagger f_\sigma |Q, S_z, r\rangle_N$, which is needed to calculate the occupancy of the impurity level. These elements are calculated from the $(N-1)^{\text{st}}$ step using the basis transformation from the iterative diagonalization and the specific initial values for the matrix elements of the added sites.

It is also possible to calculate dynamical properties, e.g. the Green's function or (of special interest concerning the DMFT in the next section) the self energy. E.g. the spectral function at temperature T, which gives the imaginary part of the Green's function, can be calculated in each iteration using the Lehmann

19

representation

$$A_\sigma^N(\omega, T) = -\frac{1}{\pi}\text{Im}\left[G_{SIAM}(\omega, T)\right]$$

$$= \frac{1}{Z_N(T)}\sum_{rr'}\left|M_{r,r'}^N\right|^2\left(e^{-\beta E_r^N} + e^{-\beta E_{r'}^N}\right)\delta(\omega - (E_{r'}^N - E_r^N)),$$

with $|r\rangle_N$ and E_r^N the eigenfunctions and eigenenergies of the Hamiltonian $H_N|r\rangle = E_r^N|r\rangle$ and the matrix elements $M_{r,r'}^N = {}_N\langle r|f_\sigma|r'\rangle_N$. There exist several possibilities to combine the information from each iteration properly. We use the method described by Bulla et al. in [31]. The resulting discrete spectrum $A_\sigma^N(\omega, T)$ is broadened using smooth distribution functions as Gaussians

$$P_G(\omega \pm E_r^N) = \frac{1}{b\sqrt{\pi}}e^{-\left((\omega \pm E_r^N)/b\right)^2},$$

Lorentzians [31]

$$P_L(\omega \pm E_r^N) = \frac{1}{2\pi}\frac{b}{(\omega \pm E_r^N)^2 + b^2}$$

or, as we use it, logarithmic Gaussians [22, 30, 31]

$$P_{LG}(\omega \pm E_r^N) = \frac{e^{-b^2/4}}{bE_r^N\sqrt{\pi}}e^{-\left(\ln\left(|\omega|/E_r^N\right)/b\right)^2},$$

with properly chosen broadening parameter $b = 0.6$. Applying the Kramers-Kronig transformation, the real part of the Green's function can be calculated

$$\text{Re}\left[G_{SIAM}(\omega, T)\right] = \frac{1}{\pi}\mathcal{P}\int_{-\infty}^{\infty}\frac{\text{Im}\left[G_{SIAM}(\omega', T)\right]}{\omega' - \omega}d\omega',$$

where $\mathcal{P}$ indicates a principal value integral.

An improvement is the method introduced by Hofstetter [32]. The idea is to calculate in a first run through the semi-infinite chain in each step the density matrix

$$\hat{\rho} = \sum_r e^{-\beta E_r}|r\rangle\langle r| \tag{2.11}$$

and in a second run the Green's function, given by

$$G_\sigma(t) = i\Theta(t)\text{Tr}\left(\hat{\rho}_{red}\left[f_\sigma(t), f_\sigma^\dagger(0)\right]\right),$$

where the reduced density matrix $\hat{\rho}_{red}$ is calculated from the density matrix Eq. (2.11) by tracing out the low energy degrees of freedom, i.e. all energy states beyond the actual chain site. This method is only adopted in Chap. 6 for the calculation of the two-impurity Anderson model with the NRG.

One possibility to calculate the self energy $\Sigma_\sigma(z)$ is to adopt the Dyson equation

$$\Sigma_\sigma(z) = G_\sigma^0(z)^{-1} - G_\sigma(z)^{-1} \tag{2.12}$$

i.e. the inverse of the full Green function $G_\sigma(z)$ subtracted from the inverse of the non-interacting Green function $G_\sigma^0(z)$. But building numerical differences is often a source of errors, so it is more convenient to follow Bulla et al. [33] and calculate the self energy via

$$\Sigma_\sigma(z) = U \frac{F_\sigma(z)}{G_\sigma(z)}$$

using the correlation functions $F_\sigma(z) = \langle\langle f_\sigma f_{\bar\sigma}^\dagger f_{\bar\sigma}; f_\sigma^\dagger \rangle\rangle_z$ and $G_\sigma(z) = \langle\langle f_\sigma; f_\sigma^\dagger \rangle\rangle_z$ defined by

$$\langle\langle A; B \rangle\rangle_z := i \int_0^\infty e^{izt} \langle [A(t), B] \rangle dt$$

and the expectation value $\tag{2.13}$

$$\langle \dots \rangle = \frac{1}{Z} \text{Tr}\left(\dots e^{-\beta(H-\mu N)}\right), \quad Z = \text{Tr}\left(e^{-\beta(H-\mu N)}\right).$$

The next chapter will introduce the dynamical mean-field theory (DMFT). The NRG method explained in this chapter is used as impurity solver for the DMFT. Important to remember is that we have a numerical exact method at hand which computes the self energy $\Sigma_\sigma(z)$ for the SIAM with the hybridization function $\Delta_\sigma(z)$ and the impurity parameters only.

3. Heavy Fermions

3.1. Discovery and experimental results

As pointed out before, for more than 30 years physicists are highly interested in heavy fermion (HF) compounds because they show numerous different physical properties and phases as e.g. Fermi liquid and non-Fermi liquid behaviour, different kinds of magnetic ordering, unconventional superconductivity and superconductivity in the vicinity of magnetically ordered phases. They all have in common a diverging effective electron mass m^* up to thousand times the bare electron mass for low temperatures. The effective electron masses can be derived from a huge linear specific heat coefficient and the Pauli susceptibility. Important examples are $CeCu_2Si_2$, $YbRh_2Si_2$ and $CeAl_3$.

Since their first discovery in 1975 by Andres, Graebner and Ott [1] many other heavy Fermion compounds have been found. Their common structure is a metallic host with a dense lattice of 4f- or 5f-orbital atoms, usually rare earth or actinide elements. In the metallic host the electronic wave functions are very widespread, such that the Coulomb interaction between the electrons can be treated perturbatively. This is described within the Fermi-liquid theory, where the electrons are replaced by non-interacting quasiparticles with renormalized masses. The electrons of the rare earth elements are strongly localized and thus are modeled as particles with strong Coulomb interaction. Interactions and hopping between f-orbitals are assumed to be negligible such that they only hybridize with the electrons of the conduction band.

3.2. The periodic Anderson model

The simplest models for these strongly correlated electron systems are lattice version of the Kondo model or the single impurity Anderson model, called the Kondo lattice model and the periodic Anderson model (PAM) respectively.

The PAM consists of four parts:

$$H = H_c + H_f + H_{hyb} + H_{int}$$

$$H_c = \sum_{\mathbf{k},\sigma} \left(\varepsilon_{\mathbf{k}} - \mu \right) c_{\mathbf{k}\sigma}^\dagger c_{\mathbf{k}\sigma}$$

$$H_f = \sum_{\mathbf{k},\sigma} \varepsilon^f f_{\mathbf{k}\sigma}^\dagger f_{\mathbf{k}\sigma}$$

$$H_{hyb} = \sum_{\mathbf{k},\sigma} \left(V_{\mathbf{k}} c_{\mathbf{k}\sigma}^\dagger f_{\mathbf{k}\sigma} + h.c. \right) \quad (3.1)$$

$$H_{int} = U \sum_{\mathbf{i}} n_{\mathbf{i}\uparrow}^f n_{\mathbf{i}\downarrow}^f$$

H_c describes the non-interacting dispersion $\varepsilon_{\mathbf{k}}$ of the conduction band, i.e. the metallic host, where $c_{\mathbf{k}\sigma}^{(\dagger)}$ is the annihilation (creation) operator for the conduction band electrons with momentum $\mathbf{k}$ and spin σ, μ is the chemical potential of the conduction band. In H_f the operators $f_{\mathbf{k}\sigma}^{(\dagger)}$ annihilate (create) electrons at the impurity site and ε^f is the on-site energy of the localized electrons. The hybridization term H_{hyb} models the overlap of the conduction band with the localized f-orbitals. $V_{\mathbf{k}}$ is the hybridization, for simplicity often assumed to be real valued and $\mathbf{k}$-independent. The last term H_{int} with $n_{\mathbf{i}\sigma}^f = f_{\mathbf{i}\sigma}^\dagger f_{\mathbf{i}\sigma}$ is the interaction of the f-electrons, which punishes double occupancy energetically due to the Coulomb repulsion U.

3.3. Perturbative and numerically exact treatments

Unfortunately, due to the non-perturbative structure of these models, there exist no theoretical tool to study them in a systematical manner in finite dimensions larger than one. E.g. perturbative treatments cannot capture strong interactions, resummation of special diagram classes can only privilege special features and mean-field theories are not able to describe spatial or temporal correlations. Bethe ansatz and bosonization techniques work only in one dimensional systems.

Numerical treatments for these lattice systems have also strong limitations. For example quantum Monte-Carlo techniques suffer the sign problem for fermionic lattice problems. With exact diagonalization one is restricted to very small system sizes in the order of ten lattice sites and the density matrix renormalization group method is also restricted to one dimensional systems.

3.4. Dynamical mean-field theory

Since our interest is focused on the low temperature and Fermi-liquid regime of the periodic Anderson model (PAM), the method of choice is the dynamical mean-field theory (DMFT) combined with the numerical renormalization group (NRG) method as impurity solver. In the following the DMFT is introduced as a powerful tool to investigate the low temperature regime of the periodic Anderson model.

The Limit of Infinite Dimensions

The pioneering work of Metzner and Vollhardt [34] in the late 80's started the development of the dynamical mean-field theory which approximates strongly correlated lattice models in a controlled manner. DMFT becomes exact in the limit of infinite lattice connectivity, i.e. especially in the limit of infinite dimensions.

For convenience we assume a d-dimensional hypercubic lattice with nearest neighbour hoppings (indicated by the angular brackets below the sum) and local interactions

$$H = \sum_{\langle \mathbf{i},\mathbf{j} \rangle, \sigma} t c_{\mathbf{i}\sigma}^{\dagger} c_{\mathbf{j}\sigma} + U \sum_{\mathbf{i}} c_{\mathbf{i}\uparrow}^{\dagger} c_{\mathbf{i}\uparrow} c_{\mathbf{i}\downarrow}^{\dagger} c_{\mathbf{i}\downarrow}, \tag{3.2}$$

where $c_{\mathbf{i}\sigma}^{(\dagger)}$ is the annihilation (creation) operator for an electron at site $\mathbf{i}$ with spin σ, t is the tunneling amplitude and U is the on-site interaction strength resulting from the Coulomb interaction. This is the Hubbard model, the simplest model for correlated electron systems. The following line of argument can also be easily extended to other lattices or more complicated models like the PAM.

The dispersion for a non-interacting Hubbard model on a d-dimensional hypercubic lattice with nearest neighbour hopping and unit lattice spacing is

$$\varepsilon_{\mathbf{k}} = -2t \sum_{i=1}^{d} \cos(k_i) .$$

The corresponding density of states (DOS) is

$$\rho(\omega) = \sum_{\mathbf{k}} \delta(\omega - \varepsilon_{\mathbf{k}}),$$

which is nothing but the probability density to find $\omega = \varepsilon_{\mathbf{k}}$ for random $\mathbf{k} = (k_1, \ldots, k_d)$. Under the assumption of randomly chosen k_i, $\varepsilon_{\mathbf{k}}$ is the sum of
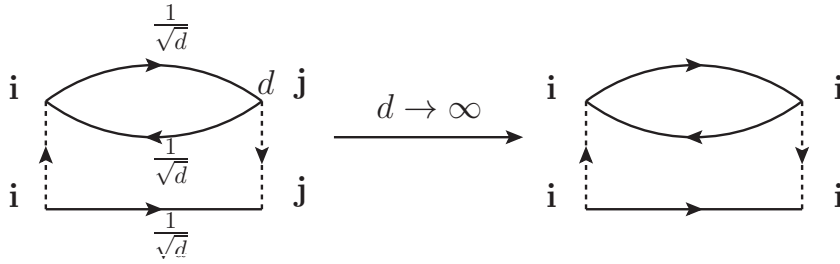
Figure 3.1.: Second order contribution to the self energy. Each free propagator line comes with a prefactor of $d^{-1/2}$ while summation over $\mathbf{j}$ gives a factor d. Thus this diagram vanishes in the limit of $d \to \infty$ if $\mathbf{i} \neq \mathbf{j}$.

independent random numbers and in the limit $d \to \infty$ the central limit theorem states

$$\rho(\omega) \xrightarrow{d \gg 1} \frac{1}{2t\sqrt{\pi d}} \exp\left[-\left(\frac{\omega}{2t\sqrt{d}}\right)^2\right].$$

For the DOS not to be flat, broad and featureless in the limit of infinite dimensions (or coordination), i.e. for a non-trivial DOS, the hopping has to scale as

$$t \to \frac{t^*}{\sqrt{d}}, \quad t^* = \text{const.} \tag{3.3}$$

Because of the local nature of the interaction term, the Coulomb interaction U does not need to be rescaled.

Most importantly this leads to a local, i.e. momentum independent, self energy for infinite dimensions

$$\Sigma_{\mathbf{ij}}(\omega) = \Sigma(\omega)\delta_{\mathbf{ij}}, \quad \text{or} \quad \Sigma_{\mathbf{k}}(\omega) = \Sigma(\omega) \tag{3.4}$$

(cf. [34, 35, 36, 37]). This can be shown rigorously, but it can also be understood qualitatively. Due to the scaling of the hopping amplitude $t = t^*/\sqrt{d}$ the non-interacting Green function for the Hubbard model is

$$G^0_{\mathbf{ij},\sigma} \propto \mathcal{O}\left(1/\sqrt{d}\right).$$

Thus, for example, for the second order self energy contribution $\Sigma^{(2)}_{\mathbf{ij}}(\omega)$ shown in Fig. 3.1 only the local term with $\mathbf{i} = \mathbf{j}$ survives, because each free propagator contributes $\propto d^{-1/2}$ and the sum of nearest neighbour sites $\mathbf{j}$ of $\mathbf{i}$ contributes $\propto d$ for $\mathbf{i} \neq \mathbf{j}$, thus

$$\Sigma^{(2)}_{\mathbf{ij}}(\omega) \propto \frac{1}{\sqrt{d}} \xrightarrow{d \to \infty} 0.$$

It can also be shown that only the local Hubbard interaction term remains dynamic in the limit of infinite dimensions. All non-local interactions contribute only statically via the Hartree-term.

Construction of the DMFT

There are several possibilities to derive the dynamical mean-field equations. Here we will follow the construction used by Georges, Kotliar, Krauth and Rozenberg [38].

The partition function for the Hubbard model, Eq. (3.2), can be rewritten as a functional integral of Grassman variables $\bar{\chi}(\tau)$ and $\chi(\tau)$

$$Z = \int D(\bar{\chi}, \chi) e^{-S[\bar{\chi}_{\mathbf{i}\sigma}(\tau), \chi_{\mathbf{i}\sigma}(\tau)]}$$

with an action

$$S[\bar{\chi}_{\mathbf{i}\sigma}, \chi_{\mathbf{i}\sigma}] = \int_0^\beta d\tau \left(\sum_{\mathbf{i},\sigma} \bar{\chi}_{\mathbf{i}\sigma}(\tau) \left(\partial_\tau - \mu \right) \chi_{\mathbf{i}\sigma}(\tau) - \sum_{\langle \mathbf{i},\mathbf{j} \rangle,\sigma} t_{\mathbf{ij}} \bar{\chi}_{\mathbf{i}\sigma}(\tau) \chi_{\mathbf{i}\sigma}(\tau) \right.$$
$$\left. + U \sum_{\mathbf{i}} \bar{\chi}_{\mathbf{i}\uparrow}(\tau) \chi_{\mathbf{i}\uparrow}(\tau) \bar{\chi}_{\mathbf{i}\downarrow}(\tau) \chi_{\mathbf{i}\downarrow}(\tau) \right). \tag{3.5}$$

The action (3.5) can be split into 3 parts

$$S = S_0 + \Delta S + S^{(0)} \quad \text{with}$$

$$S_0 = \int_0^\beta d\tau \left(\sum_\sigma \bar{\chi}_{0\sigma}(\tau) \left(\partial_\tau - \mu \right) \chi_{0\sigma}(\tau) + U \bar{\chi}_{0\uparrow}(\tau) \chi_{0\uparrow}(\tau) \bar{\chi}_{0\downarrow}(\tau) \chi_{0\downarrow}(\tau) \right)$$

$$\Delta S = - \int_0^\beta d\tau \sum_{\mathbf{i} \neq 0,\sigma} \left(t_{\mathbf{i}0} \bar{\chi}_{\mathbf{i}\sigma}(\tau) \chi_{0\sigma}(\tau) + t_{0\mathbf{i}} \bar{\chi}_{0\sigma}(\tau) \chi_{\mathbf{i}\sigma}(\tau) \right)$$

$$S^{(0)} = \int_0^\beta d\tau \left(\sum_{\mathbf{i} \neq 0,\sigma} \bar{\chi}_{\mathbf{i}\sigma}(\tau) \left(\partial_\tau - \mu \right) \chi_{\mathbf{i}\sigma}(\tau) - \sum_{\langle \mathbf{i},\mathbf{j} \rangle, \mathbf{ij} \neq 0,\sigma} t_{\mathbf{ij}} \bar{\chi}_{\mathbf{i}\sigma}(\tau) \chi_{\mathbf{i}\sigma}(\tau) \right.$$
$$\left. + U \sum_{\mathbf{i} \neq 0} \bar{\chi}_{\mathbf{i}\uparrow}(\tau) \chi_{\mathbf{i}\uparrow}(\tau) \bar{\chi}_{\mathbf{i}\downarrow}(\tau) \chi_{\mathbf{i}\downarrow}(\tau) \right).$$

Here S_0 denotes the action for site zero only, ΔS the part which connects site zero to the remaining lattice and $S^{(0)}$ is the action for a model where site zero and its bonds are removed. Now a series expansion in ΔS reveals that in the limit $d \to \infty$ due to the scaling property (3.3) only the second order contribution survives, thus the effective action after integrating out the bath degrees of freedom is

$$S_{eff}[\bar{\chi}_{0\sigma}, \chi_{0\sigma}] = \int_0^\beta d\tau \sum_\sigma \bar{\chi}_{0\sigma}(\tau_1) \mathcal{G}_\sigma^{-1}(\tau_1 - \tau_2) \chi_{0\sigma}(\tau_2)$$
$$+ U \int_0^\beta d\tau \bar{\chi}_{0\uparrow}(\tau) \chi_{0\uparrow}(\tau) \bar{\chi}_{0\downarrow}(\tau) \chi_{0\downarrow}(\tau) \tag{3.6}$$

with the Weiß mean-field (or effective medium Green function)

$$\mathcal{G}_\sigma^{-1}(\tau_1 - \tau_2) = -\left(\partial_{\tau_1} - \mu\right)\delta_{\tau_1\tau_2} + \sum_{\mathbf{i,j}\neq 0,\sigma} t_{\mathbf{i}0}t_{\mathbf{j}0}G_{\mathbf{ij}\sigma}^{(0)}(\tau_1 - \tau_2)\,. \qquad (3.7)$$

$G_{\mathbf{ij}\sigma}^{(0)}$ is the cavity Green function, where site 0 is removed, and it has to be related to the full lattice Green function, i.e.

$$G_{\mathbf{ij}\sigma}^{(0)} = G_{\mathbf{ij}\sigma} - G_{\mathbf{i}0\sigma}G_{00\sigma}^{-1}G_{0\mathbf{j}\sigma}\,. \qquad (3.8)$$

This equation states that the cavity Green function consists of all paths of the full Green function without the paths going through site 0. And in the limit $d \to \infty$ only paths that go once through 0 have to be counted. Insertion of Eq. (3.8) into Eq. (3.7) and switching to Matsubara frequencies the effective medium can be calculated to

$$\mathcal{G}_\sigma^{-1}(i\omega_n) = \Sigma_\sigma(i\omega_n) + \int_{-\infty}^{\infty} \frac{\rho(\varepsilon)}{i\omega_n - \varepsilon + \mu - \Sigma_\sigma(i\omega_n)}\,.$$

Analytic continuation provides real frequency properties

$$\mathcal{G}_\sigma^{-1}(z) = \Sigma_\sigma(z) + \int_{-\infty}^{\infty} \frac{\rho(\varepsilon)}{z - \varepsilon + \mu - \Sigma_\sigma(z)}\,,$$

with $z = \omega + i\delta$, where a small but finite δ replaces the infinitesimal offset in our numerical calculations. In the next step this result will be compared to the Green function of the SIAM.

Connection to the SIAM

Consider again the Hamiltonian of the single impurity Anderson model (2.1)

$$H = \sum_{\mathbf{k},\sigma}\left(\varepsilon_{\mathbf{k}} - \mu\right)c_{\mathbf{k}\sigma}^\dagger c_{\mathbf{k}\sigma} + \sum_\sigma \varepsilon^f n_\sigma^f + Un_\uparrow^f n_\downarrow^f + \sum_{\mathbf{k},\sigma}\left(V_{\mathbf{k}}f_\sigma^\dagger c_{\mathbf{k}\sigma} + V_{\mathbf{k}}^* c_{\mathbf{k}\sigma}^\dagger f_\sigma\right)$$

and rewrite it as an action for the grand canonical ensemble with Grassmann fields $\bar\chi, \chi$ for the conduction band electrons and $\bar\phi, \phi$ for the impurity

$$S[\bar\chi, \chi, \bar\phi, \phi] = \sum_{\mathbf{k},n,\sigma}\left(-i\omega_n + \varepsilon_{\mathbf{k}}\right)\bar\chi_{\mathbf{k}n\sigma}\chi_{\mathbf{k}n\sigma} + \left(-i\omega_n + \varepsilon^f\right)\bar\phi_{n\sigma}\phi_{n\sigma}$$
$$+ \sum_{\mathbf{k},n,\sigma}\left(V_{\mathbf{k}}\bar\chi_{\mathbf{k}n\sigma}\phi_{n\sigma} + V^*\bar\phi_{n\sigma}\chi_{\mathbf{k}n\sigma}\right) + U\int_0^\beta d\tau n_\uparrow^f(\tau)n_\downarrow^f(\tau)\,. \qquad (3.9)$$

Integrating out the conduction band degrees of freedom results in the action

$$S[\bar\phi, \phi] = \sum_n \bar\phi_{n,\sigma}\left[\mathcal{G}_\sigma^{SIAM}(i\omega_n)\right]^{-1}\phi_{n,\sigma} + U\int_0^\beta d\tau n_\uparrow^f(\tau)n_\downarrow^f(\tau) \qquad (3.10)$$

with

$$\left[\mathcal{G}_\sigma^{SIAM}(i\omega_n)\right]^{-1} = i\omega_n - \varepsilon^f - \Delta^{SIAM}(i\omega_n) \tag{3.11}$$

with

$$\Delta^{SIAM}(i\omega_n) = -\frac{1}{\pi}\int_{-\infty}^{\infty} d\omega \frac{\Delta(\omega)}{i\omega_n - \omega}$$

and the hybridization function $\Delta(\omega)$ is defined as

$$\Delta(\omega) = \pi \sum_{\mathbf{k}} |V_{\mathbf{k}}|^2 \, \delta(\omega + \varepsilon_{\mathbf{k}}) \, . \tag{3.12}$$

The hybridization function $\Delta(\omega)$ solely determines the influence of the bath on the impurity. After analytical continuation, obviously the impurity Green function $\mathcal{G}_\sigma^{SIAM}(z)$ (3.11) has to be compared to the effective medium Green function $\mathcal{G}_\sigma(z)$ of the lattice model and we find

$$\Delta^{SIAM}(z) = z - \varepsilon^f - \Sigma_\sigma(z) - \left[G_\sigma^{lat}(z)\right]^{-1} \, . \tag{3.13}$$

Self-consistent solution

The single impurity problem has strong interactions and is still far from being trivial. However, with the NRG (Chap. 2) at hand, we have a numerical impurity solver that is ideally suited for the exponentially small temperature regime.

Another problem is that the SIAM representing the effective medium for the lattice problem is unknown. A solution is to solve the system self-consistently. I.e. we start for example with an arbitrarily chosen hybridization function, which should be positive and have a finite weight. Then we solve the corresponding SIAM and extract the local self energy $\Sigma_\sigma(\omega)$. Thereafter the knowledge of the self energy $\Sigma_\sigma(\omega)$ is used to calculate the local Green function $G_\sigma^{lat}(\omega)$ and with it we use Eq. (3.13) to finish the loop and recalculate an improved hybridization function $\Delta(\omega)$. This is schematically shown in Fig. 3.2. At this point it should be mentioned that it is also possible to calculate momentum dependent properties. The momentum dependence returns into the Green function by means of the dispersion relation $\varepsilon_{\mathbf{k}}$. In the case of the Hubbard model for example the momentum dependent Green function is

$$G_\sigma(\mathbf{k}, z) = \frac{1}{z + \mu - \varepsilon_{\mathbf{k}} - \Sigma_\sigma(z)} \, .$$
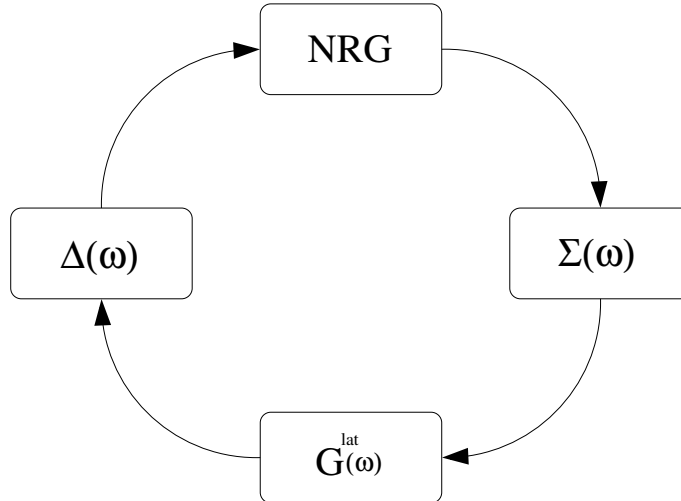
Figure 3.2.: Illustration of the DMFT cycle: Start with a hybridization function $\Delta(\omega)$ as input for the NRG to calculate the self energy $\Sigma(\omega)$, then determine the local lattice Green function and finally recalculate $\Delta(\omega)$ using the self-consistency relation Eq. (3.13). The spin index σ has been dropped because our calculations concentrate on the paramagnetic phase.

DMFT and the most common impurity solvers

The DMFT is a powerful tool to investigate strongly correlated lattice models, because it is non-perturbative and takes temporal correlations into account. Its downside is the negligence of spatial correlations. Thus long-ranged correlation effects as e.g. the emergence of spin ordered phases are not observable. Another point is that DMFT is an approximation for high dimensional system. Thus the DMFT method is not well suited for 1D and 2D systems with small coordination number.

As mentioned before, we have chosen the NRG as impurity solver because it is numerically exact, efficient and gives access to the exponentially low energy scale, i.e. around and below the Kondo respectively coherence scale.

Other common choices with different advantages and regions of applicability are

- Exact diagonalization (ED): This is also a numerically exact method that gives access to the full spectrum of the SIAM. Generally it is possible to compute physical properties at any given temperature. But due to the exponential growth of the Hilbert space with system size, the method is restricted to systems of the order of ten sites. As a result the energy resolution is rather coarse.

- Quantum Monte Carlo (QMC): The Hirsch-Fye QMC [41] method is a successful and widely used tool to investigate impurity problems. It can be applied to a wide range of problems with mostly minor changes in the program. It provides numerically exact results for the imaginary time Green function and other important physical quantities. Its greatest disadvantage is the drastic increase in computation time with $U\beta = U/T$. I.e. this method is not feasible for low temperatures and large interaction strength. Another disadvantage is that the QMC works on the imaginary time axis. Thus analytic continuations have to be performed to obtain real frequency data as spectral functions or self energies. This is also a numerically difficult task.

- Continuous-time (CT) QMC: CT QMC methods are recent improvements of the QMC algorithm by Gull et al. [44]. They are based on a diagrammatic expansion of the partition function in the interaction term or the hybridization term. They combine the advantages of the Hirsch-Fye QMC methods and an improved performance compared to the discrete QMC version such that they allow access to much lower temperatures. But they are still working on the imaginary time axis and thus there still is the difficult task of the analytic continuation.

4. Conduction band depletion and exhaustion in the PAM

In this chapter we study the periodic Anderson model within the framework of the DMFT. The results were obtained using essentially the programs, especially the NRG program, provided by Priv.-Doz. Dr. Ralf Bulla. We investigate the behaviour of this model under strongly increasing interactions for different lattice geometries. The Gaussian DOS, which resembles a hybercubic lattice with nearest neighbour interactions, the semielliptical DOS produced by a Bethe lattice, both in the limit of infinite dimensions, and for a constant DOS.

First we review the possible metallic and insulating phases of the PAM and then the so called exhaustion effect, where only a few conduction electrons are available to screen the local impurities at exponentially small energy scales. Then we show DMFT results for the different densities of states. The last part is concerned with the coherence scale, the temperature scale at which conduction band electrons screen the f-electrons local moment coherently, in connection to the lattice geometry and we show a zero temperature phase diagram for the interaction strength U and the conduction band filling μ.

All DMFT calculations conducted in this and the following chapters are performed at zero temperature and with the following general parameters, which were tested properly.
The discretization parameter $\Lambda = 2$,
maximum number of states kept at each iteration $N_{max} = 500$,
broadening of the discrete NRG data with logarithmic Gaussians $b = 0.6$
and the imaginary offset in $z = \omega + i\delta$, $\delta = 0.004$.
Our calculations are performed in the paramagnetic phase. Therefore the spin index σ can be omitted for the Green functions, self energies, spectral functions and effective mediums.
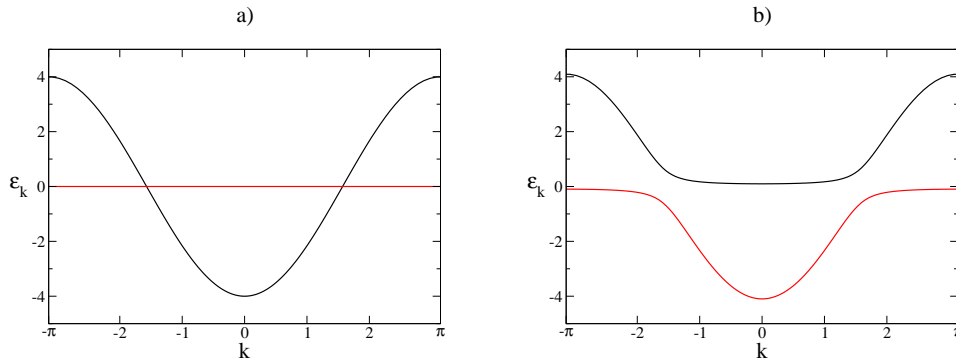
Figure 4.1.: Visualization of the hybridization gap in the PAM. Conduction band (black line) and impurity band (red line) for the symmetric ($\mu = \varepsilon^f = 0$) one dimensional PAM with nearest neighbour hopping $t = 1$ and interaction $U = 0$ for a) $V = 0$ and b) $V = 0.1$.

4.1. Metal–Insulator transitions

In our DMFT calculations we could confirm two different kind of insulating phases for the PAM.

For the canonical choice of a local hybridization, i.e. a hybridization of the local moments with conduction band electrons on the same site only, $V_{\mathbf{k}} = V$, and vanishing interaction, $U = 0$, the one-particle bands can be obtained by diagonalizing the Hamiltonian (3.1),

$$E_{\pm}(\mathbf{k}) = \frac{1}{2} \left(\mu - \varepsilon^f - \varepsilon_{\mathbf{k}} \pm \sqrt{4V^2 + (\varepsilon^f + \mu - \varepsilon_{\mathbf{k}})^2} \right) \qquad (4.1)$$

In the case of half-filling, $\mu = \varepsilon^f = 0$, the Fermi energy lies in between the two bands and thus the system is in a band insulating state, also known as Kondo insulator, illustrated in Fig. 4.1. Switching on interactions U, but keeping the model at half filling, i.e. $\varepsilon^f = -U/2$, correlations cause merely a renormalization of the hybridization gap.

Another insulating state which shows up in the PAM is the Mott insulator. This state was found in a class of materials that should be electrically conducting under standard band theory. But due to odd integer filling and strong Coulomb interactions these materials insulate at low temperatures. For a qualitative understanding consider again the Hubbard model (3.2). Assuming a given lattice structure, the model depends only on the ratio of hopping and Coulomb interaction t/U, the electron density $n = \frac{1}{N} \langle n_{i\uparrow} n_{i\downarrow} \rangle$ and the temperature T.

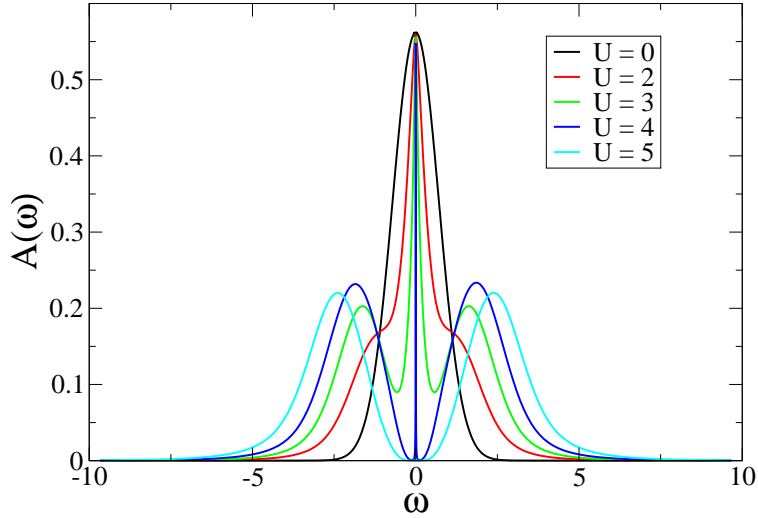At $T = 0$ and a small $n \ll 1$ the interaction term can be treated as perturba-

Figure 4.2.: Evolution of the half-filled Hubbard model with a Gaussian bare DOS for increasing Coulomb repulsion between two conduction electrons on the same site.

tion due to a low density of charge carriers and the system can be described as weakly interacting Fermi liquid. For $n \approx 1$ and $U/t \ll 1$ the system can still be treated within perturbation theory and shows Fermi liquid properties. More interesting is the case $n \approx 1$ and $U/t \gtrsim 1$ where the interaction makes hopping costly and thus the electronic excitation spectrum splits up into two Hubbard bands separated by a charge gap of width $\Delta \approx U$. Finally for half-filling and $U/t \rightarrow \infty$ hopping is completely forbidden due to Coulomb interaction and every neighbouring site is already occupied by one electron. This is the Mott insulating state. More detailed information can be found in [7, 40].

Figure 4.2 shows the zero temperature spectral function for the Hubbard model at half filling calculated using DMFT with the NRG. It shows that for increasing Coulomb interaction a gap of the order of U opens at the Fermi energy and thus the system becomes insulating. The emergence of the Hubbard peaks at $\approx \pm U/2$ can also be seen, where all the spectral weight is shifted in the insulating case.

The PAM shows also a Mott transition for $T \rightarrow 0$, strong Coulomb repulsion on the local orbitals and a total filling of $n_{tot} = 1$ and $n_{tot} = 3$, see e.g. Sordi et al. [42, 43].

4.2. Exhaustion

A different effect we investigate within the DMFT, first mentioned by Nozières [5], is the effect of exhaustion. It is discussed intensively in the last two decades. Exhaustion describes the effect of low conduction band fillings, such that there are much more f-band electrons than electrons in the conduction band. In that case it is assumed that the number of conduction band electrons is not sufficient to screen all local moments of the f-orbital band.

The line of argumentation is as follows: The number of impurities is N_{imp}, while the effective number of electrons N_{eff} available to screen the impurities are in a range of the (single impurity) Kondo temperature T_K, see Eq. (2.3), around the Fermi energy ε_F. So $N_{eff} = \rho(\varepsilon_F)T_K$ with $\rho(\varepsilon_F)$ the DOS at the Fermi energy. The dimensionless number

$$p = \frac{N_{imp}}{N_{eff}} = \frac{N_{imp}}{\rho(\varepsilon_F)\,T_K}$$

is roughly the number of spins a single electron has to screen. The exhaustion is measured by p. Noziéres argued further that the Kondo temperature T_K, reduced by the scattering events necessary to isotropize the local moments spin, gives an upper bound for the coherence scale

$$T_c = \frac{T_K}{p} = \frac{\rho(\varepsilon_F)\,T_K^2}{N_{imp}}\,.$$

Thus, his arguments conclude that there exist two energy scales in the PAM and that the coherence scale T_c is proportional to T_K^2.

4.3. Influence of the DOS

The self-consistency equations for the PAM (3.1) can be calculated in the same manner as for the Hubbard model. A detailed derivation can be found in appendices A and B. The local impurity band Eq. (A.1) and conduction band Green functions Eq. (B.4) are

$$G^f(\omega) = \int_{-\infty}^{\infty} \frac{\rho(\varepsilon)}{\omega - \varepsilon^f - \Sigma(\omega) - \frac{V^2}{\omega - \varepsilon + \mu}}\, d\varepsilon$$

and

$$G^c(\omega) = \int_{-\infty}^{\infty} \frac{\rho(\varepsilon)}{\omega - \varepsilon + \mu - \frac{V^2}{\omega - \varepsilon^f - \Sigma(\omega)}}\, d\varepsilon\,.$$

The Green functions depend on the lattice structure due to the density of states $\rho(\varepsilon)$. In the following we want to address the question how strong the
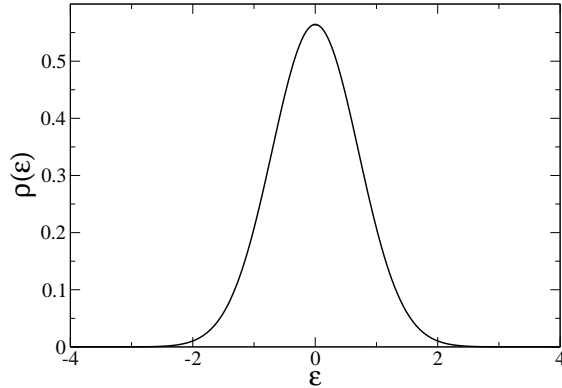
Figure 4.3.: The DOS for an infinite dimensional hypercubic lattice of non-interacting conduction electrons is given by a Gaussian.

scaling properties of the PAM depend on the specific form of the DOS and if we find qualitative differences in the physics of the model. Therefore we use three different kinds of DOS. The first one is a Gaussian, which is an infinitely differentiable function with an infinite support. The second one is a semi-elliptical function, which is continuous, but not differentiable at the band edges and it has a finite support. The third functional form we use is a constant DOS, which has also a finite support but is not continuous at the band edges.

In all cases we have chosen a site independent next nearest neighbour hopping

$$t_{\mathbf{ij}} = \begin{cases} t = 1, & \text{if } |\mathbf{i} - \mathbf{j}| = 1 \\ 0, & \text{else} \end{cases}$$

and a constant local hybridization $V_{\mathbf{k}} = V$. We investigate the behaviour of the system while depleting the conduction band but keeping the impurity band fixed to half filling, i.e. $\varepsilon^f = -U/2$.

4.3.1. Gaussian DOS

The first simulations are conducted with a Gaussian DOS, Fig. 4.3,

$$\rho(\varepsilon) = \frac{1}{t\sqrt{\pi}} e^{-\left(\frac{\varepsilon}{t}\right)^2}. \tag{4.2}$$

This DOS is differentiable on the whole infinite support and has no singularities. As described in Sec. 3.4, the corresponding lattice structure is a hypercubic lattice with infinite coordination number.
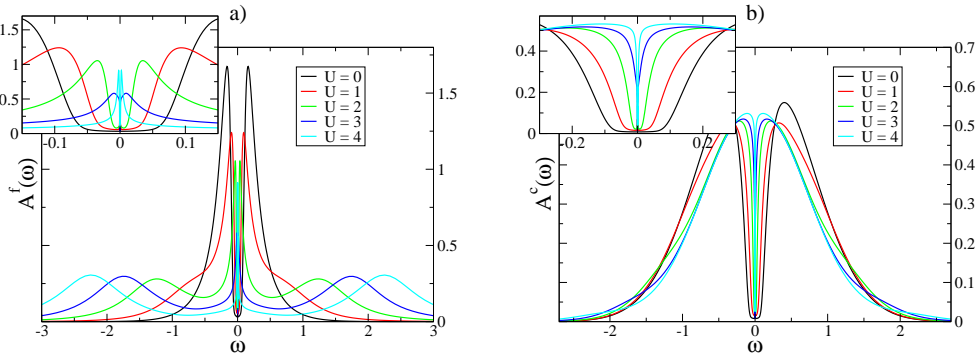
Figure 4.4.: Zero temperature spectral function for the f-band a) (the inset shows an enlargement around the Fermi energy) and conduction band b) for the PAM with $\mu = 0$, $\varepsilon^f = -U/2$, $V = 0.4$. A band gap remains for both spectral functions for all shown Coulomb interactions U. $A^{f,c}(\omega = 0) > 0$ is an artificial remnant from the finite convergence generating factor δ from $z = \omega + i\delta$.

Figure 4.4 depicts the impurity band a) and conduction band spectral function b) in the symmetric case, $\mu = 0$, $\varepsilon^f = -U/2$, and with hybridization $V = 0.4$ at $T = 0$. The gap in the spectral functions around the Fermi energy is clearly visible for all values of U. The finite values of the spectral functions at the Fermi energy, $A^{f,c}(\omega = 0) > 0$, stems from the convergence generating factor δ in $z = \omega + i\delta$. Similar to Fig. 4.2 a shift of the spectral weight to the Hubbard satellites for increasing Coulomb interaction can be observed for the impurity spectral function. The non-vanishing gap for all values of U confirms that the gap is a result of the hybridization of the two bands.

Figure 4.5 shows zero temperature spectral functions for the impurities a) and the conduction electrons b) and the imaginary and real part of the self energy c) and d) for a gradual depletion of the conduction band electrons while the other parameters are fixed $U = 1$, $\varepsilon^f = -U/2$ and $V = 0.4$. Both spectral functions show for $\mu = 0$ the same gap as already mentioned in Fig. 4.4. But reducing the chemical potential below $\mu = -0.4$, $A^f(\omega)$ develops a strong quasiparticle resonance. Although there is no quasiparticle resonance in the conduction band spectral function, we find also a finite number of conduction band electrons around the Fermi energy for $\mu \lesssim -0.4$. This indicates metallic behaviour in this parameter regime. The asymmetry in the conduction band filling also induces an asymmetry in the filling of the impurity band.

The imaginary part of the self energy of the f-states 4.5 c) is quadratic in ω around the Fermi energy for $\mu \lesssim -0.4$, i.e. in the metallic phase. This is accompanied by a linear ω-dependence of the real part d), where the slope
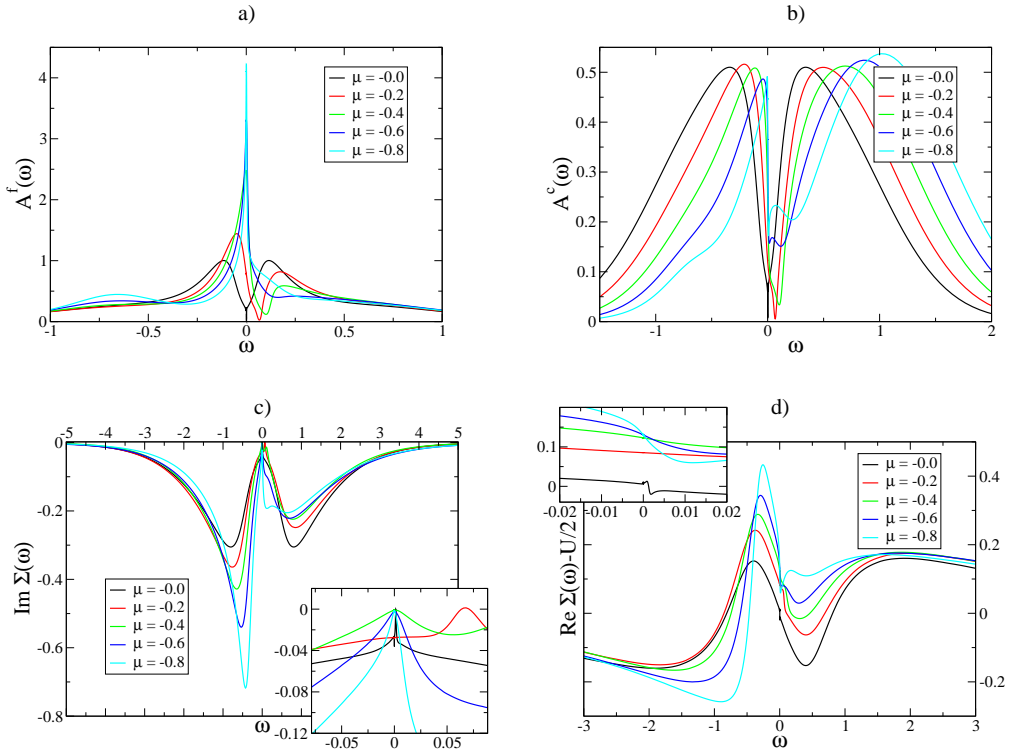
Figure 4.5.: Spectral functions for the impurity band a) and conduction band b) for $U = 1$, $\varepsilon^f = -U/2$ and $V = 0.4$. Depletion of the conduction band filling turns the insulating state $\mu = 0$ into a metallic state at $\mu \approx -0.4$. The asymmetry in the conduction band also introduces an asymmetry in the f-band and a strong quasiparticle peak at the Fermi energy. Fig. c) and d) show Fermi liquid properties for $\mu \lesssim -0.4$ indicated by $\operatorname{Im}\Sigma(\omega) \propto \omega^2$ and the linear behaviour for $\operatorname{Re}\Sigma(\omega)$ with negative slope at $\omega = 0$. (Insets show enlargement around the Fermi energy)

of the linear region is negative. As far as the self energy is concerned, this confirms that the PAM is in a Fermi liquid state in this parameter range. The quasiparticle weight Z for a Fermi liquid is defined as

$$ Z^{-1} = 1 - \left.\frac{d \operatorname{Re}\Sigma(\omega)}{d\omega}\right|_{\omega=0} = \frac{m^*}{m}, \tag{4.3} $$

where m is the bare electron mass and m^* is the quasiparticle mass or effective mass of the quasiparticles. It can already be seen from the figures, that the effective masses increase for a reduced conduction electron density. In Sec. 4.5 we will investigate the quasiparticle weight in more detail. In the band insulating state, i.e. $\mu = 0$, we do not expect Fermi liquid behaviour. This is confirmed by the calculations, in $A^f(\omega)$ there is no sharp quasiparticle peak, the imaginary part of the self energy does not show the parabolic behaviour and the linear part of $\operatorname{Re}\Sigma(\omega)$ has a positive slope.
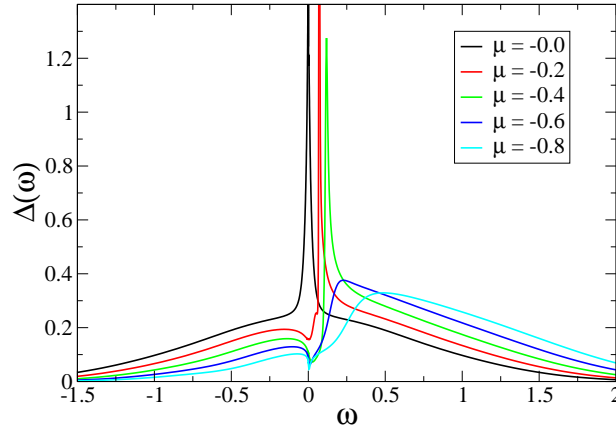
Figure 4.6.: Zero temperature effective hybridization $\Delta(\omega)$ with $U = 1$, $\varepsilon^f = -U/2$ and $V = 0.4$. The depletion of the conduction band leads to a reduction of $\Delta(\omega)$ at $\omega \approx 0$, which is interpreted as hallmark of Nozières exhaustion effect.

At last we want to examine the hybridization function $\Delta(\omega)$, Fig. 4.6. There is a strong peak for $0 \geq \mu \gtrsim -0.4$. Pruschke et al. [9] pointed out that the peak stems from the quasiparticle band with f-character at the Fermi energy. The peak reduces in size and vanishes at about $\mu = -0.6$ for depletion of the conduction electron band, i.e. when the system becomes metallic. Additionally $\Delta(\omega)$ is reduced at $\omega \approx 0$ in the metallic phase. This has been interpreted as a hallmark of Nozières exhaustion effect since the density of medium states available at a given site should be reduced due to the screening at other sites.

Fig. 4.7 illustrates the effect of very strong depletion of the conduction band electrons for $U = 2$, $\varepsilon^f = -U/2$ and $V = 0.4$. For $\mu \lesssim -1.4$ the width of the quasiparticle resonance becomes smaller than the resolution of the NRG around the Fermi energy and thus the low energy structures around the Fermi energy would vanish in all figures a) - d) for numerical reasons for further reduction of conduction band electrons. Therefore $\mu = -1.4$ is the lowest conduction band filling resolvable here. Down to lowest conduction electron densities resolvable we find stable quasiparticle states a) and a finite density of states for the conduction- and the f-band a) and b). Fig. 4.7 c) and d) show also that the self energy is in agreement with Landau's Fermi liquid picture. The main figure and the insets c) show clearly the quadratic behaviour of Im $\Sigma(\omega)$ and in d) the linearity of Re $\Sigma(\omega)$ around $\omega = 0$. The slope in d) decreases enormously while reducing the average number of conduction electrons, which

results in very small quasiparticle weights respectively in huge quasiparticle masses. A detailed discussion of the evolution of the quasiparticle weights will be given in Sec. 4.5. The last figure e) shows the effective hybridization function $\Delta(\omega)$ and the increasing impact of the exhaustion effect in the inset, which shows an enlargement of $\Delta(\omega)$ around the Fermi energy. The dip is getting more pronounced for further reduction of conduction electrons.

Finally we state that the system is in a band insulating state at exactly half filling. But depleting the conduction band leads to a phase transition to a metallic phase and the calculations support the conclusion that we have a Fermi liquid with strongly increased quasiparticle masses down to the lowest fillings feasible with DMFT/NRG.
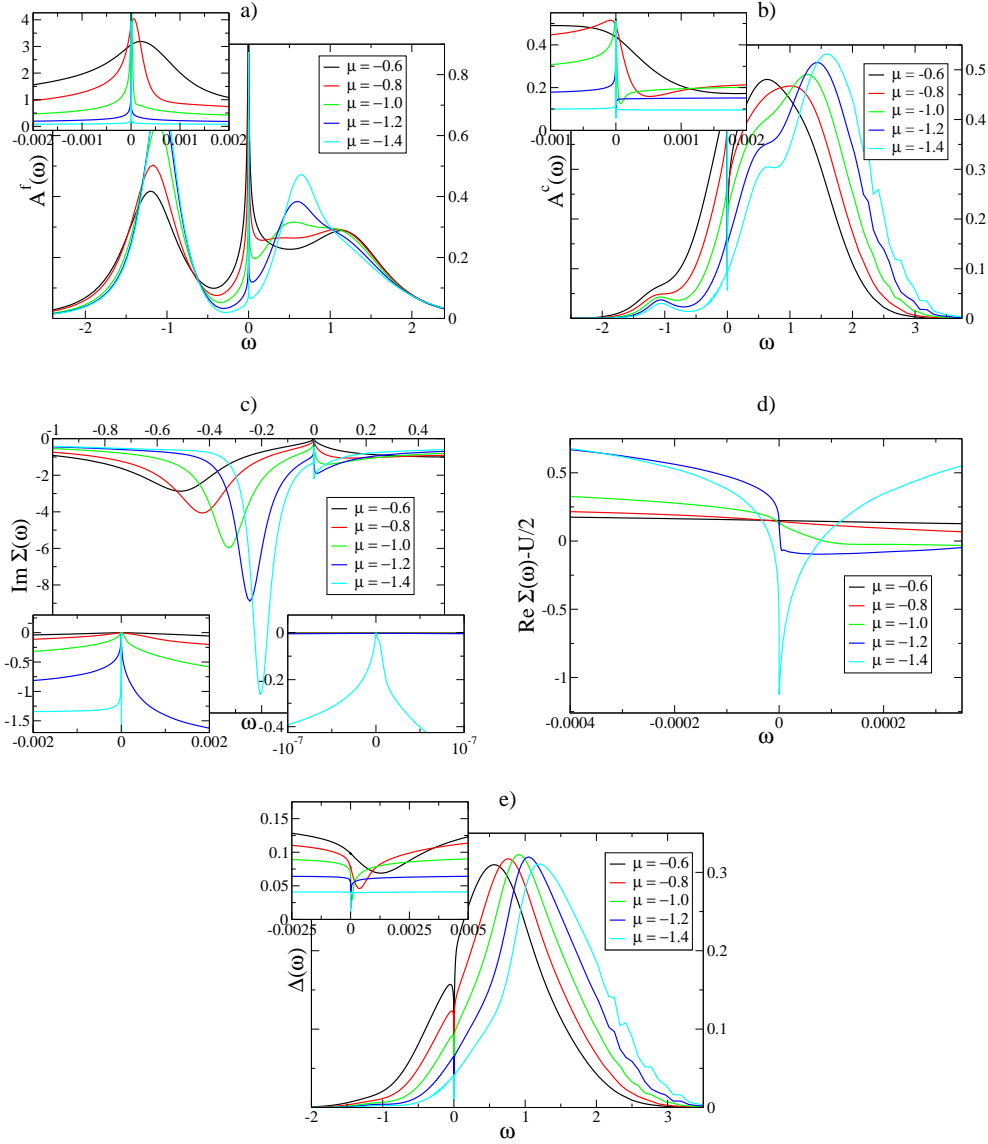
Figure 4.7.: The figures show the influence of the depletion of the conduction band for a Gaussian bare DOS and $U = 2$, $\varepsilon^f = -U/2$ and $V = 0.4$ at $T = 0$. The insets show enlargements around the Fermi energy for the corresponding functions.
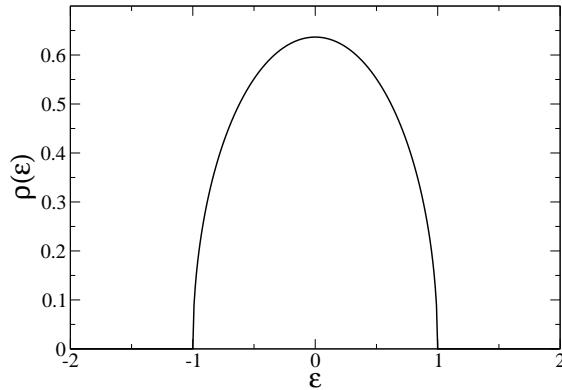
Figure 4.8.: Semi-elliptical DOS for non-interacting conduction electrons on a Bethe lattice with infinite coordination number and a hopping amplitude of $t = 1$.

4.3.2. Semi-circular DOS

Now we investigate the behaviour of the PAM on a Bethe lattice with infinite coordination number and hopping amplitude $t = 1$. The bare density of states is a normalized semi-circular function and not differentiable at the band edges $\omega = \pm 1$, see Fig. 4.8.

The spectral functions for the impurity- and the conduction band in Fig. 4.9 show again the hybridization gap in the half filled case $\mu = 0$ and $\varepsilon^f = -U/2$, except for the small offset due to the convergence generating factor. This is shown exemplarily for $V = 0.4$ and increasing Coulomb interaction U. Fig. 4.9 a) depicts again the high energy Hubbard satellites at $\approx \pm U/2$. In 4.9 b) we observe that the general semi-elliptical structure of $A^c(\omega)$ is preserved apart from the hybridization gap. But both spectral functions lose their non-differentiable behaviour at the band edges due to the renormalizations of the Coulomb interaction.

Starting from $U = 2$, $\varepsilon^f = -U/2$, $\mu = 0$ and $V = 0.4$ and reducing the number of conduction band electrons drives the system also away from the band insulating to a metallic phase, see Fig. 4.10. The transition is between $-0.4 \lesssim \mu \lesssim -0.2$ and is indicated by the emerging strong quasiparticle resonance at the Fermi energy of the spectral functions $A^{f,c}(\omega)$, in Fig. 4.10 a) and b). In the metallic phase the imaginary and real part of the self energy, c) and d), are also in agreement with Fermi liquid theory. The f-band spectral function $A^f(\omega)$ also shows the high-energy charge excitations at $\pm U$.

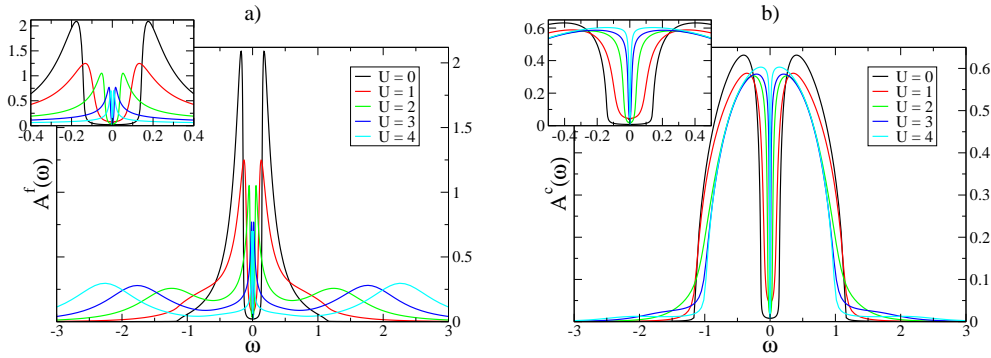Further reduction of the conduction electron filling reduces the width of the

Figure 4.9.: Zero temperature spectral function for the f-band a) and conduction band b) (the insets show enlargements around the Fermi energy) for the PAM with $\mu = 0$, $\varepsilon^f = -U/2$, $V = 0.4$ and a semi-elliptical bare DOS. A band gap remains for both spectral functions for all shown Coulomb interactions U. $A^{f,c}(\omega = 0) > 0$ is an artificial remnant from the finite convergence generating factor δ in $z = \omega + i\delta$.

quasiparticle resonance until it vanishes at a critical chemical potential μ and finite U. Fig. 4.11 shows the electron densities for the impurity and conduction electrons. The parameters are chosen as before, i.e. $U = 2$, $\varepsilon^f = -U/2$ and $V = 0.4$. The spectral functions are finite at the Fermi energy, thus show metallic behaviour for $\mu \geq -1.1$. But for $\mu \leq -1.2$ a gap around the Fermi energy has emerged, which is more apparent in the insets, where the positive energy part of the function is shown on a logarithmic scale. Unfortunately, even though the zero temperature Mott metal-to-insulator transition is of first order, we were not able to resolve a hysteresis. Fig. 4.12 shows clearly the reduction of the conduction band filling (red line), while the impurity band is roughly half filled (black line). Thus in total the system is on average filled with one electron per unit cell (green line) in the insulating phase. This is in agreement with a Mott insulating phase, which can only be realized for integer filling.

Conclusively we can say that within the DMFT the PAM has a hybridization gap for the Bethe lattice at half filling. Reducing the number of conduction band electrons, the system becomes metallic, shows enhanced quasiparticle masses and exhibits signs of the Nozières exhaustion scenario. Due to Coulomb interactions the spectral weight is shifted in such a way that the conduction band filling is still finite even though the Fermi energy is set below the band edge of the bare DOS. But for a critical chemical potential the system crosses a first order transition to the Mott insulating phase.
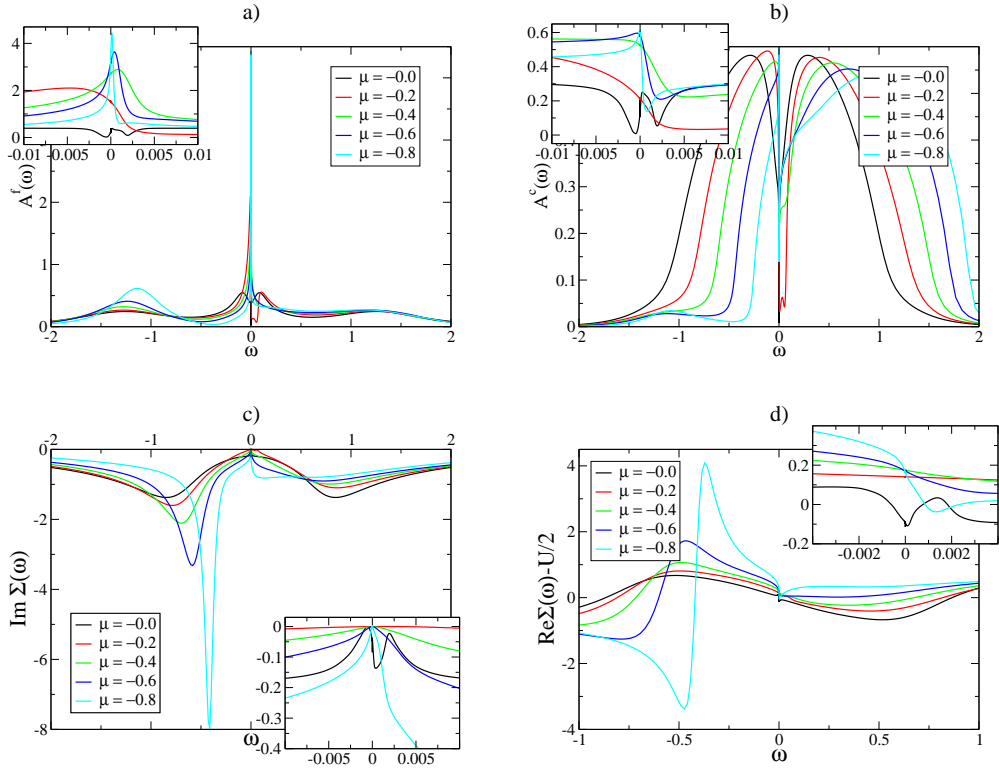
Figure 4.10.: $T = 0$ spectral functions for the impurity band a) and conduction band b) for $U = 2$, $\varepsilon^f = -U/2$ and $V = 0.4$ for a semi-elliptical bare DOS. Depletion of the conduction band filling turns the insulating state $\mu = 0$ into a metallic state for $\mu \lesssim -0.4$. The asymmetry in the conduction band spectral function also introduces an asymmetry in the f-band spectral function. Also a strong quasiparticle peak at the Fermi energy emerges in a). Fig. c) and d) show Fermi liquid properties for $\mu \lesssim -0.4$ indicated by $\mathrm{Im}\,\Sigma(\omega) \propto \omega^2$ and the linear behaviour for $\mathrm{Re}\,\Sigma(\omega)$ with negative slope at $\omega = 0$ (Insets show enlargement around the Fermi energy).
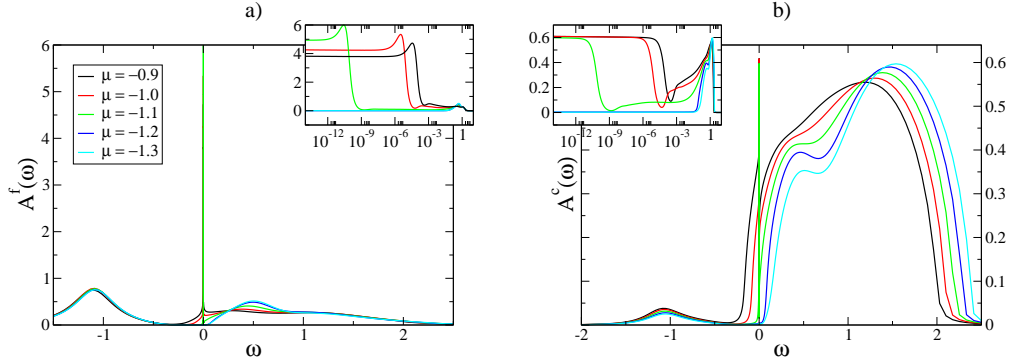
Figure 4.11.: Zero temperature impurity band a) and conduction band b) spectral function for $U = 2$, $\varepsilon^f = -U/2$ and $V = 0.4$ for the Bethe lattice with infinite connectivity. The logarithmic plot in the insets displays the sudden disappearance of the quasiparticle peak for $\mu \lesssim -1.2$.
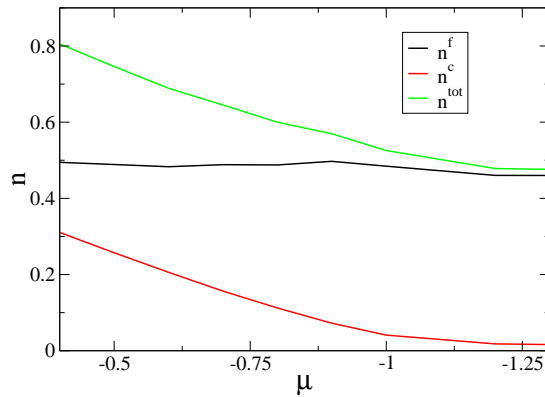

Figure 4.12.: Impurity band n^f, conduction band n^c and total filling $n^{tot} = n^f + n^c$ of the PAM for $U = 2$, $\varepsilon^f = -U/2$ and $V = 0.4$.
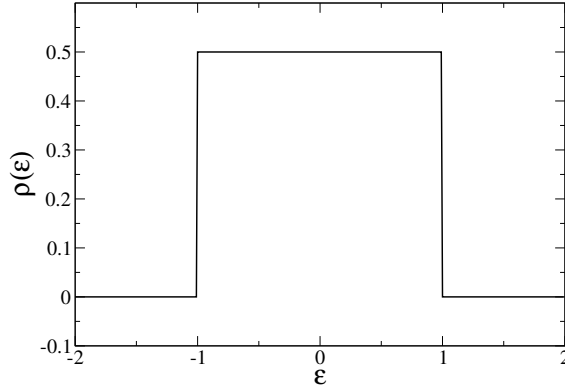
Figure 4.13.: Constant DOS for the DMFT for the PAM.

4.3.3. Constant DOS

In this section we explore the PAM for a constant bare DOS (Fig. 4.13),

$$\rho(\varepsilon) = \frac{1}{2} \left(\Theta \left(\varepsilon + 1 \right) - \Theta \left(\varepsilon - 1 \right) \right) .$$

Due to the discontinuous behaviour of the DOS $\rho(\varepsilon)$ at the band edges $\varepsilon = \pm 1$, the model is expected to show unconventional properties, especially when the Fermi energy approaches the lower band edge. In this situation the effects of exhaustion are expected to have a stronger influence.

The main opportunity of a constant DOS is the possibility to observe the coherence scale of the periodic Anderson model upon depleting the conduction band without changing the Kondo scale (defined for the single impurity Kondo model, Eq. (2.3))

$$T_K \propto \exp \left(-\frac{U}{4V^2 \rho(\varepsilon_F)} \right) .$$

Thus we are able to isolate the effects of exhaustion from the effects of a reduced DOS at the Fermi energy ε_F.

But it turns out that the behaviour of the system with a constant DOS is qualitatively the same as for the semi-elliptical DOS. Therefore we only show exemplarily the spectral functions, Fig. 4.14, of the impurity band a) and conduction band b), and discuss the main properties. For a discussion of the coherence scale and its connection to the Kondo scale see section 4.5. The hybridization function, self energy and fillings are in qualitative accordance to the ones for a Bethe lattice DOS in Sec. 4.3.2. The logarithmic scale of ω in the insets of Fig. 4.14 reveals the low energy behaviour more clearly. The parameters are chosen $U = 2$, $\varepsilon^f = -U/2$ and $V = 0.4$. The conduction band filling is reduced starting out from half filling, i.e. $\mu = 0$ to $\mu = -1.2$.
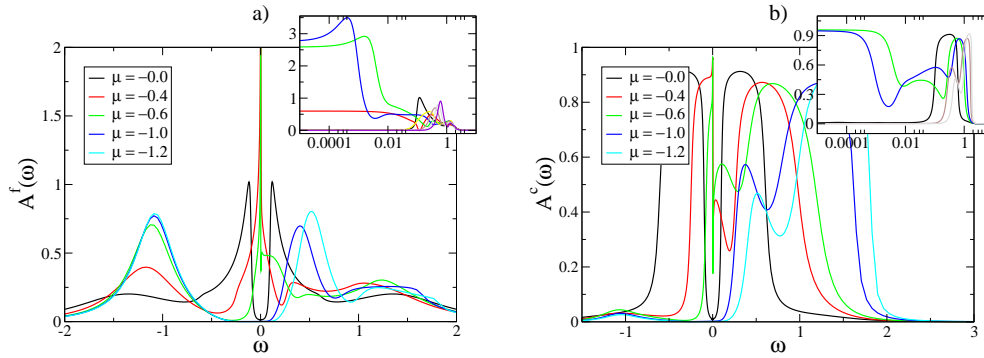
Figure 4.14.: Zero temperature impurity band a) and conduction band b) spectral function for $U = 2$, $\varepsilon^f = -U/2$ and $V = 0.4$ using a constant density of states.

Most important, we observe that the spectral functions have lost their discontinuity at the band edges, they are even differentiable due to the finite interaction term U. Furthermore, Fig. 4.14 b) shows clearly on the logarithmic scale in the inset, that in the metallic regime $-1 < \mu < -0.4$ the spectral function $A^c(\omega)$ is fixed to its non-interacting value at the Fermi energy, $\rho(\omega = 0)$.

For $\mu = 0$ (black line) the system is band insulating, for $-1 < \mu < -0.4$ it shows a finite DOS at the Fermi energy, i.e. metallic phase and for $\mu < -1$ it is Mott insulating. Depleting the conduction band shifts spectral weight of $A^f(\omega)$ from the resonance at the Fermi energy to the Hubbard satellites at $\pm U/2 = \pm 1$.

4.4. Phase diagram for the PAM

In the last section we saw three different possible phases for the paramagnetic PAM with different lattice types. With these results it is possible to construct a phase diagram. Fig. 4.15 depicts the zero temperature phase boundaries in a (U, μ)-diagram. Here the remaining parameters are $\varepsilon^f = -U/2$, i.e. f-band filling $n_f \approx 1$, and $V = 0.4$. For $\mu \approx 0$, i.e. conduction band filling $n_c \approx 1$, the systems with Gaussian, semi-elliptical and constant DOS all show a band insulating phase. They also show a phase transition between the band insulating (BI) and heavy Fermion (HF) phase between $-0.5 \lesssim \mu \lesssim -0.25$ for all values of Coulomb interactions U investigated. For intermediate conduction band fillings, $-1.2 \lesssim \mu \lesssim -0.5$ all systems show a Fermi liquid phase with more pronounced heavy Fermion (HF) properties for increasing Coulomb inter-
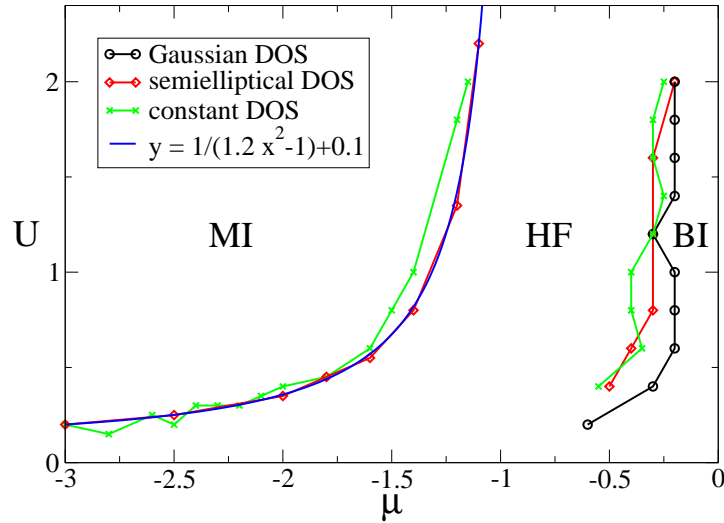
Figure 4.15.: Zero temperature (U, μ)-phase diagram of the periodic Anderson model for decreasing conduction band occupation and three different bare DOS with $V = 0.4$ and $\varepsilon^f = -U/2$. On the right hand side is a band insulating (BI) phase for each model. The Mott insulating (MI) phase on the left hand side is only realized for the model with a semi-elliptical or a constant DOS. Each model shows a metallic heavy Fermion (HF) phase. The blue line shows a fit to the phase boundary between the HF and the MI phase for the semi-elliptical DOS

actions. Only for the semi-elliptical and the constant DOS the phase diagram shows a parameter regime where the system is in a Mott insulating (MI) state. The phase boundaries follow roughly $U \propto 1/(\mu^2 - 1)$, the blue line shows a fit to the HF-MI phase boundary for the PAM with a Bethe lattice. For a hypercubic lattice the system showed no sign of a MI phase.

Thus we conclude that the finite tails of the Gaussian DOS prevents the system from a transition to the Mott insulating phase. Sharp band edges are an essential ingredient for the diluted PAM to become Mott insulating.

4.5. Coherence scale

As mentioned before, the PAM follows Landau's Fermi liquid picture in the metallic phase. I.e. below a certain temperature scale, the coherence scale T_c, which is proportional to the quasiparticle weight (4.3), the effective quasiparticles have the quantum numbers of the original electrons (charge, spin, momen-
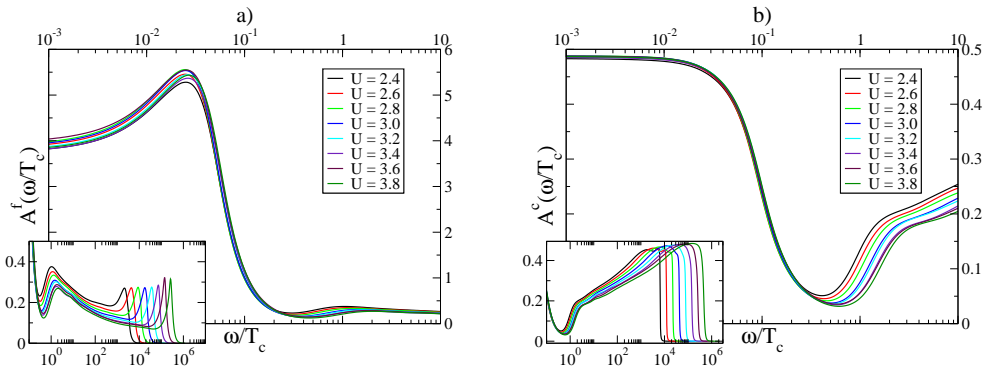
Figure 4.16.: Spectral functions for the impurity band a) and conduction band b) for $\varepsilon^f = -U/2$, $\mu = -1$, $V = 0.4$ and a constant DOS. The frequencies are rescaled by the coherence temperature T_c.

tum) but show renormalized parameters, as e.g. strongly enhanced masses m^*. Fig. 4.16 depicts spectral functions for the impurity band a) and the conduction band b) for $\varepsilon = -U/2$, $\mu = -1$, $V = 0.4$ and a constant DOS. The system is metallic for all values of the Coulomb interaction shown. The energies are rescaled by the coherence temperature extracted from the self energy using Eq. (4.3). The rescaled spectral functions fit excellent on top of each other in the low energy range, i.e. the quasiparticle peak structure below $\omega \approx T_c$. The high energy features as the Hubbard satellites are not scale invariant for values $\omega/T_c \gtrsim 1$ as can be seen in the insets, where the rescaled high energy regions are depicted. We could not identify an energy scale which scales the spectral functions properly for $\omega/T_c \gtrsim 1$.

Fig. 4.17 comprises the evolution of the coherence scale T_c for four different fillings and three different density of states. The hybridization strength is $V = 0.4$. For vanishing interaction strength the coherence scale is always of the order of one since there is no interaction reliable for any renormalizations.

The slope of the coherence scales for the different lattice structures is for small values of U identical. But we observe that the fewer conduction electrons are available for screening, the steeper the slope.

For very low conduction band fillings, $\mu = -1.5$ and $\mu = -2.0$, the coherence scales for the constant and the Bethe lattice DOS drop off faster than exponentially beyond the Mott transition. The reason is obviously that in the Mott phase the Fermi liquid picture is not valid and the particles are completely localized. The coherence scale for the PAM on a hypercubic lattice, which does not show a Mott insulating phase, follows an exponential law as suggested in Eq. (4.3) down to lowest energy scales resolvable.
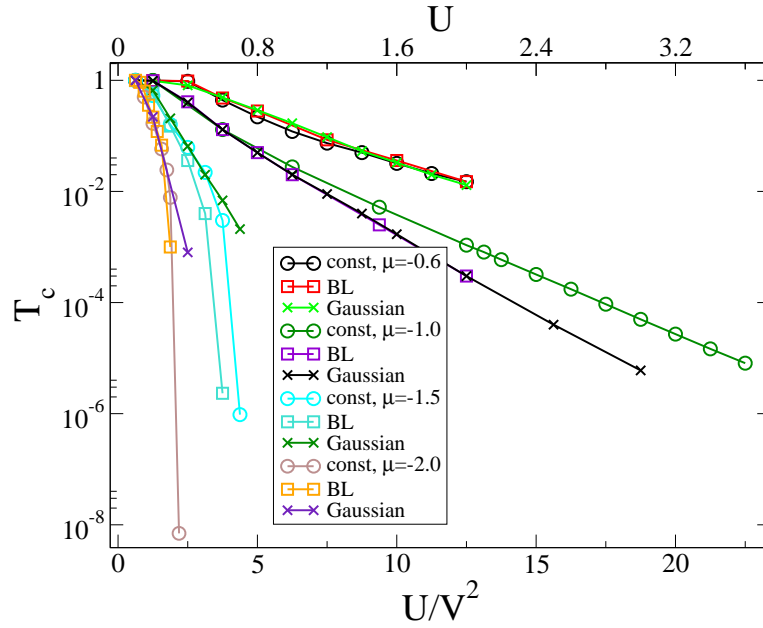
Figure 4.17.: Evolution of the coherence scale T_c for increasing Coulomb interaction U for different fillings. We have chosen a constant DOS and the hybridization is fixed to $V = 0.4$.

In the case of higher conduction band fillings, $\mu = -0.6$, all three coherence scales are equal. For $U \lesssim 0.4$ the system is band insulating and thus T_c is not well defined and the coherence scales show a kink at $U \approx 0.4$. Beyond $U \approx 0.4$ the coherence scales fall off exponentially. For $\mu = -0.6$ we did not observe a transition to the Mott insulating phase (compare Fig. 4.15) for the tested DOS.

Shifting the Fermi energy to the band edge of the semi-elliptical DOS, i.e. $\mu = -1$, we observe a linear, negative slope for the Gaussian and the Bethe lattice coherence scale. The constant DOS behaves identical up to $U \approx 0.8$ but shows a kink at that point and thereafter a slightly increased slope. Thus the coherence scale for the hypercubic and the Bethe lattice follows an exponential law. The reason is yet unknown, but it might stem from the fact that the Fermi energy is shifted exactly to the discontinuity in the constant DOS.

Fig. 4.18 depicts the conduction band (black line), impurity band (red line) and the total filling (green line) for four different chemical potentials μ for the Gaussian (crosses), semi-elliptical (circles) and the constant (squares) bare density of states. The figures show that the fillings depend only weakly on the underlying bare DOS. Only for $\mu = -1$ for the constant DOS, where the Fermi energy is positioned at a discontinuity, the conduction band filling n^c_{const} and
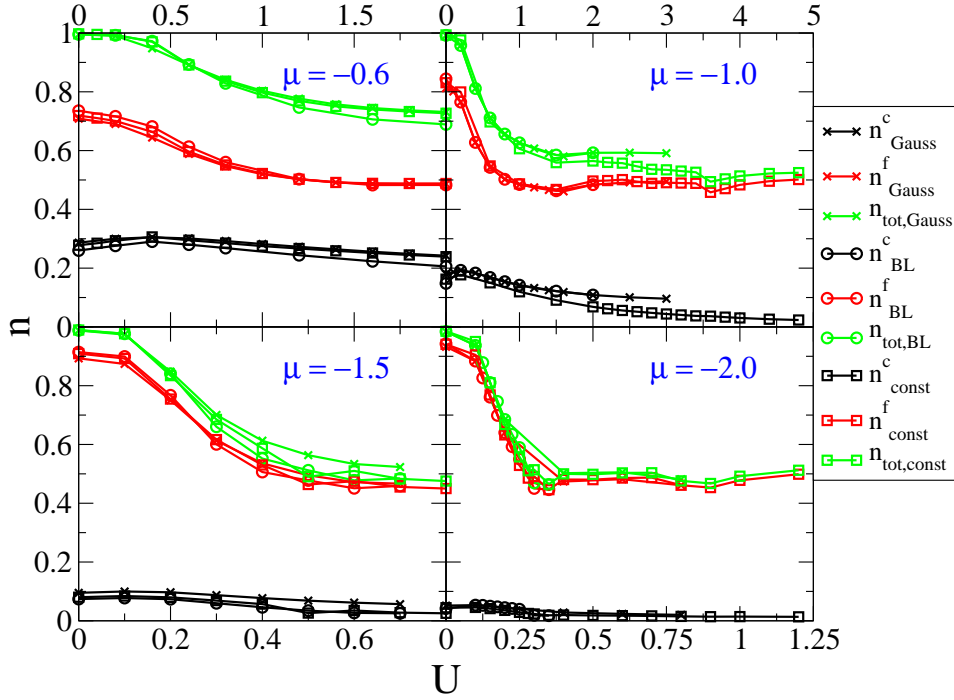
Figure 4.18.: Conduction band (black), impurity band (red) and total filling (green) of the PAM for different models - Gaussian DOS (crosses), semi-elliptical (circles) and constant DOS (squares) - and four different chemical potentials μ.

as a result the total filling $n_{tot,const}$ is reduced compared to the other two cases. This, together with the results from Fig. 4.17, stands in contrast to the idea of exhaustion, because from exhaustion we would expect for a reduced filling also a reduced coherence scale and not an increased one.

Conclusions

Within the DMFT approximation for the PAM with symmetric impurity band, i.e. $\varepsilon^f = -U/2$, the form of the bare DOS is important for the realization of a metal-Mott insulator transition. Only a DOS with a finite support gives rise to a Mott insulating phase. Contrary to that, the form of the DOS has in general a negligible influence on the band insulating - metal transition and also on the Fermi liquid properties in the metallic phase. Thus the scaling for a single impurity model at half filling, i.e. $\varepsilon^f = -U/2$, Eq. 2.3

$$T_K = \frac{D}{k_B} e^{-\frac{V^2}{4U\rho(\varepsilon_F)}},$$

is not completely valid for the concentrated model, because although T_c scales with $\exp(-U/V^2)$, the scaling does not depend on the form of the DOS $\rho(\omega)$

in the metallic phase. We found an exception to the last statement, when the Fermi energy is situated at a discontinuity of the DOS. However, we were not able to identify a second energy scale which could be related to the Kondo scale as predicted by Nozières.

5. PAM on a bipartite lattice

In this chapter we investigate the periodic Anderson model (PAM) on a bipartite hypercubic lattice. First we will introduce the model and set up the DMFT equations. Then we investigate the case of equal sublattices and whether the model reduces to the standard PAM. Thereafter our research concentrates on the model with one sublattice of f-orbitals with strong Coulomb interactions and the other one with weak interactions. And finally we investigate the behaviour of the system while decoupling one sub lattice.

5.1. Introduction

The periodic Anderson model was proposed to describe heavy fermion compounds, where a local spin-$\frac{1}{2}$ moment per unit cell is embedded in a host of conduction electrons. There are two main reasons to extend this model onto bipartite lattice systems.

On the one hand materials with two inequivalent f-shell ions per unit cell have been discovered, e.g. $Ce_3Pd_{20}Si_6$ by Kitagawa et al. [45]. These compounds feature two inequivalent local spin-$\frac{1}{2}$ moments per unit cell. We will model these systems with the PAM on a bipartite hypercubic lattice, where we have the possibility to tune the impurity parameters for the sublattices independently.

Another reason these models attract much attention is the possibility to explore the crossover from single impurity behaviour to the behaviour of a lattice impurity system, to understand the development of the Kondo scale T_K when more and more impurities added to a metallic host. Does the coherence scale T_c emerge from the the Kondo scale or is it independent from T_K? If the latter is the case, how does the coherence scale emerge? Therefore, setting up a bipartite lattice for the PAM and decoupling the impurities of one sublattice in our model is the first step to simulate the crossover to the diluted system.

5.2. Model and method

The Hamiltonian for the PAM is

$$H = \sum_{\langle ij \rangle, \sigma} t_{ij}\, c_{i\sigma}^\dagger c_{j\sigma} + \sum_{i\sigma} \left(\varepsilon_c\, c_{i\sigma}^\dagger c_{i\sigma} + \varepsilon_f^i\, f_{i\sigma}^\dagger f_{i\sigma} + \frac{1}{2}\, U_i\, n_{i\uparrow}^f n_{i\downarrow}^f + V_i\, c_{i\sigma}^\dagger f_{i\sigma} + h.c. \right)$$

(5.1)

where t_{ij} is the hopping amplitude for the conduction electrons from site i to site j, $c_{i\sigma}^\dagger$ creates and $c_{i\sigma}$ destroys a conduction electron on site i with spin σ, $f_{i\sigma}^\dagger$ and $f_{i\sigma}$ work analogue for the f-electrons, ε_c is an energy shift for the conduction electrons, $\varepsilon_f^i = \varepsilon_f^A$ if i on sublattice A and ε_f^B if i on sublattice B is the on-site energy for the f-electrons, $U_{A,B}$ is the Coulomb repulsion on sublattice A respectively B and $V_{A,B}$ determines the hybridization between conduction and impurity electrons on sublattice A respectively B. As usual $t_{ij} = t$ the hopping amplitude is site independent and only non-zero between nearest neighbours.

The model is solved with the DMFT method (refer Chap. 3) and as impurity solver we employ the NRG method (Chap. 2) from Priv.-Doz. Dr. Ralf Bulla with the numerical parameters as in Chap. 4. The effective medium is (see appendix D)

$$\mathcal{G}^\alpha(z) = \frac{1}{\left(\sum_k \tilde{G}_k^{f,\alpha}(z) \right)^{-1} + \Sigma^\alpha(z)}$$

$$\tilde{G}_k^{f,\alpha}(z) = \frac{\varepsilon_k V_\alpha V_{\bar\alpha} - z_c V_{\bar\alpha}^2 + z_{\bar\alpha}(z_c^2 - \varepsilon_k^2)}{V_\alpha^2 V_{\bar\alpha}^2 - z_c z_\alpha V_{\bar\alpha}^2 - z_c z_{\bar\alpha} V_\alpha^2 - z_\alpha z_{\bar\alpha}(z_c^2 - \varepsilon_k^2)}$$

(5.2)

with

$$\alpha \in \{A, B\} \text{ and } \bar\alpha = \begin{cases} B, & \text{if } \alpha = A \\ A, & \text{if } \alpha = B \end{cases}$$

$$z_\alpha = z - \varepsilon_\alpha - \Sigma_\alpha(z)$$

$$z_c = z - \varepsilon_c.$$

The self-consistency condition is given by

$$[\mathcal{G}^\alpha(z)]^{-1} \stackrel{!}{=} \left[G_0^{SIAM}(z) \right]^{-1} = z - \varepsilon_\alpha - \Delta^\alpha(z)$$

which concludes the hybridization functions for the two sublattices as

$$\Delta^\alpha(z) = z - \varepsilon_\alpha - \Sigma^\alpha(z) - \left[G^{f,\alpha}(z) \right]^{-1} \text{ with } G^{f,\alpha}(z) = \sum_k \tilde{G}_k^{f,\alpha}(z).$$
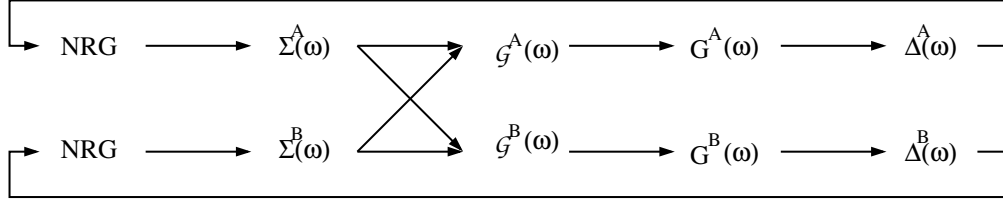
Figure 5.1.: DMFT cycle for the PAM on a bipartite lattice.

The self-consistent DMFT cycle for the PAM on a bipartite lattice is pictured in Fig. 5.1. As starting point we choose proper hybridization functions $\Delta^\alpha(\omega)$ for each sublattice, then compute the self energies for each $\Delta^\alpha(\omega)$ using the NRG. Both self energies then contribute to each effective medium $\mathcal{G}^\alpha(\omega)$ (i.e. we cannot split the calculations up into two independent DMFT cycles). To close the cycle the sublattice Green functions and then the hybridization functions have to be calculated using Eq. 5.2.

Limit of equal sublattices

Now using the limit, where all parameters on both sublattices are the same, Eq. 5.2 yield

$$
\begin{aligned}
\mathcal{G}(z) &= \frac{1}{\left(\sum_k \tilde{G}_k^f(z)\right)^{-1} + \Sigma(z)} \ , \\
\tilde{G}_k^f(z) &= \frac{1}{z - \varepsilon^f - \Sigma(z) - \frac{V^2}{z - \varepsilon_k - \varepsilon_c}} \ ,
\end{aligned}
\tag{5.3}
$$

which is the self-consistency condition for the PAM without sublattice structure. Also numerically this could be verified. Fig. 5.2 shows the f-electron spectral functions for the homogeneous PAM (full lines) and the PAM with a bipartite lattice, but all sublattice parameters are the same (dotted lines). Since the spectral functions of the A and B sublattices are the same the sublattice index is omitted. The inset shows an enlargement of the quasiparticle peaks. The numerical results show that using the more complicated formula Eq. 5.2 does not introduce additional numerical issues compared to the simpler form Eq. 5.3.

5.3. Energy scales

Specific theories, e.g. slave Boson mean-field theory, predict two energy scales for the Kondo lattice model, a Kondo scale T_K and a coherence scale T_c at
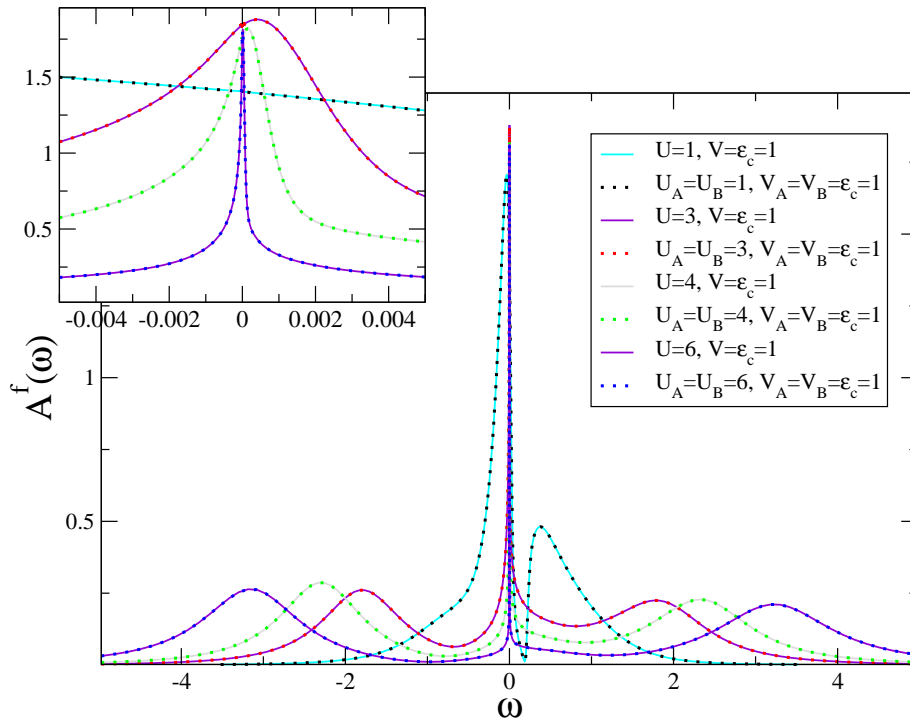
Figure 5.2.: The figure shows a comparison between the homogeneous PAM (straight lines) and the PAM with a bipartite lattice (dotted lines) where $\varepsilon^f = -U/2$ respectively $\varepsilon_\alpha = -U_\alpha/2$.

much lower temperatures (e.g. Burdin et al. [10]). Solving the model within the DMFT method did not reveal a second energy scale up to now (see e.g. Pruschke et al. [9], Chap. 4). For the Kondo lattice model with a bipartite lattice Benlagra et al. [8] found even four distinct energy scales, a Kondo scale and a coherence scale for each sublattice. We will investigate the PAM on a bipartite lattice first by varying the Coulomb interaction on one sublattice and later while varying the hybridization between the conduction band and one sublattice.

5.3.1. Varying the Coulomb interaction on one sublattice

In this section we investigate the systems behaviour upon changing the Coulomb interaction on one sublattice and focus our attention on the energy scales of the system.

The applied DMFT method is described in Sec. 5.2. Because we have

severe convergence problems within the DMFT method with a bipartite lattice, we start from a point in parameter space where the model reduces to the homogeneous case, i.e. $U_A = U_B$, $V_A = V_B$ and $\varepsilon_A = \varepsilon_B = -U_A/2$, where we find appropriate convergence, and change only one parameter at a time and in small steps. In this case it is the Coulomb interaction U_A and therewith $\varepsilon_A = -U_A/2$, such that we have nearly half filled f-bands.

Fig. 5.3 shows the development of the f-electron spectral functions for both sublattices with parameters $U_B = 2$ and $V_A = V_B = \varepsilon_c = 0.4$. In all figures appears the general three peak structure, the two charge excitation peaks at $\omega \approx \pm U/2$ and the Abrikosov-Suhl resonance at $\omega = 0$. The charge excitation peaks Fig. 5.3 a) and c) move away from the Fermi level with increasing U_A as expected, whereas the Hubbard satellites in b) and d) are fixed. I.e. that one sublattice has no effect on the high energy excitations of the spectral function of the other sublattice. But Fig. 5.3 a)-d) points out that the Abrikosov-Suhl resonance at low energies changes drastically the low energy excitations on both sublattices upon the variation of U_A. That implies, of course, a strong influence of U_A on both sublattices at low energies. The spectral function on sublattice A, $A^{f,A}(\omega)$ shows a decreasing width for increasing U_A, but while the full width at half max (FWHM) decreases continuously, the height decreases until it starts to increase at $U_A \gtrsim 2.0$. The Kondo resonance of the f-electron spectral function $A^{f,B}(\omega)$ shows at first a decreasing broad structure slightly below the Fermi energy (inset Fig. 5.3 b)) for increasing U_A, and develops a small quasiparticle resonance at $\omega = 0$ up to $U_A \approx 2.0$. Then the new quasiparticle peak sharpens, i.e. becoming thinner and increases for $U_A > 2$.

For all parameters the hybridization function Fig. 5.4 shows the bare density of states (DOS) with additional structures due to interaction effects. Important is the behaviour around the Fermi level. Since a reduction of $\Delta(0)$ is interpreted as a hallmark of exhaustion physics, because the reduction of effective medium DOS available at a special site is strongly reduced due to screening effects at the other impurities, this dip in $\Delta(\omega)$ is very interesting. Analogue to the spectral function $A^{f,A}(\omega)$ the hybridization function $\Delta^A(\omega)$ (5.4 a) and b)) shows a continuously narrowing dip for increasing U_A around the Fermi energy, whereas its height, $\Delta^A(0)$, first increases up to $U_A \approx 2$ and then decreases again for increasing U_A. $\Delta^B(\omega)$ has a broad dip below the Fermi energy which vanishes for increasing U_A and reveals a narrower and continuously deepening dip at $\omega = 0$. The dip below the Fermi level has completely vanished at $U_A = 2$.

Now let us take a brief look on the self energies $\Sigma^\alpha(\omega)$ in Fig. 5.5. All self en-
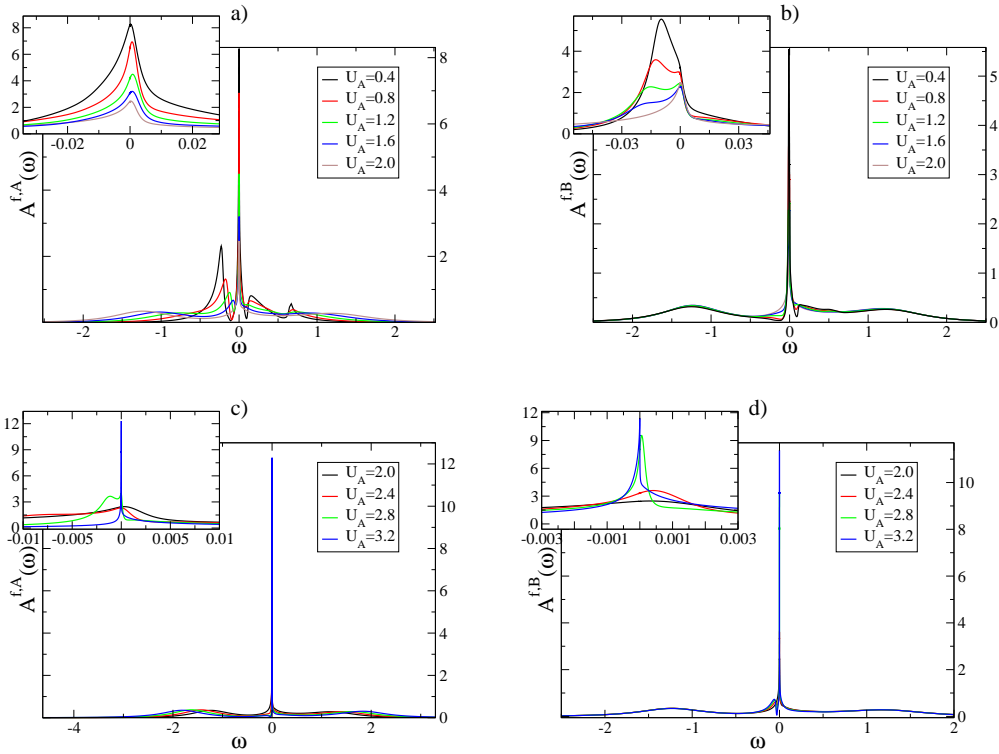
Figure 5.3.: Evolution of the f-electron spectral function for the A and B sublattices upon changing Coulomb interaction U_A, $U_B = 2$, $V_A = V_B = \varepsilon_c = 0.4$ and $\varepsilon_\alpha = -U_\alpha/2$ with $\alpha \in \{A, B\}$.

ergies show a quadratically vanishing imaginary part (insets show enlargement of $\Sigma(\omega)$ around the Fermi level) which is common in Fermi liquids. Another property of Fermi liquids is a linear real part of the self energy around $\omega = 0$ in a region proportional to the FWHM of the Abrikosov-Suhl resonance of the f-electron spectral function. This linear behaviour is also found in the bipartite PAM, shown in Fig. 5.5.

Since the system depicts Fermi liquid behaviour with sharp quasiparticles for each sublattice, we can properly define the quasiparticle weight Z or respectively the quasiparticle mass m_α^* for sublattice $\alpha \in \{A, B\}$

$$Z_\alpha = \frac{m}{m_\alpha^*} = \frac{1}{1 - \left.\frac{\partial \Sigma^\alpha(\omega)}{\partial \omega}\right|_{\omega \to 0}} \tag{5.4}$$

and we assign an energy scale, the coherence scale $T_{\alpha,c} \propto Z_\alpha^{-1}$, to the corresponding sublattice.

In Fig. 5.6 the quasiparticle masses for the two different sublattices and different U_B are plotted against U_A. The dark green line shows data for equal sublattices, i.e. the homogeneous PAM. In this case, the coherence scale de-
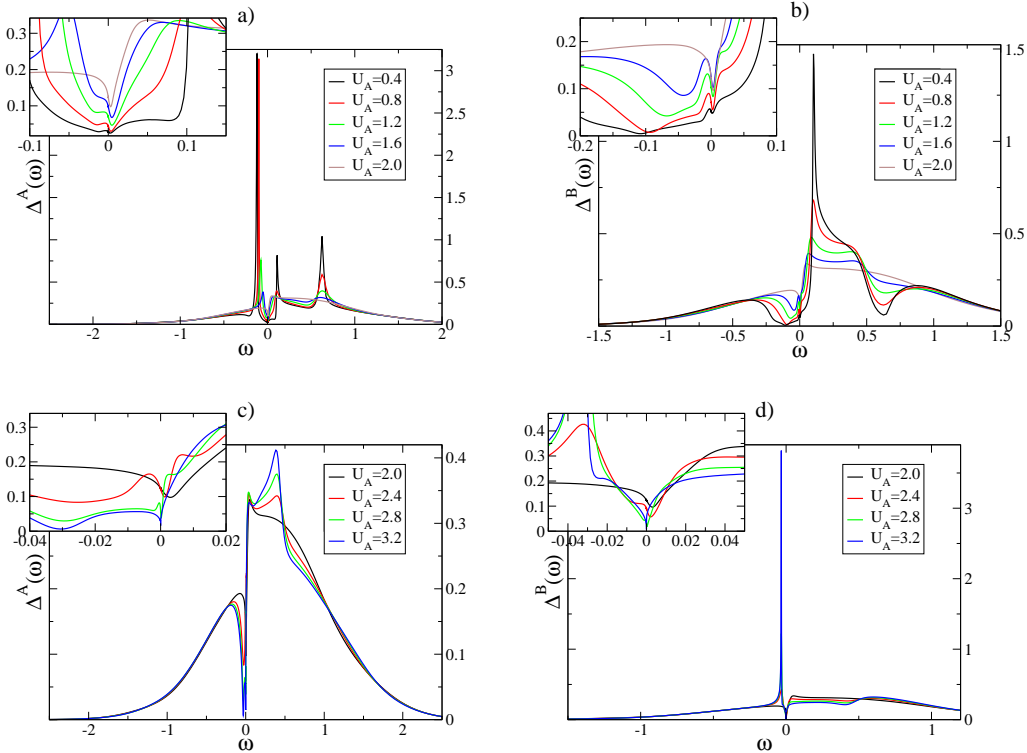
Figure 5.4.: Evolution of the hybridization functions $\Delta^\alpha(\omega)$ for the A and B sublattices upon changing Coulomb interaction U_A, $U_B = 2$, $V_A = V_B = \varepsilon_c = 0.4$ and $\varepsilon_\alpha = -U_\alpha/2$ with $\alpha \in \{A, B\}$.

creases exponentially in the whole parameter space as already shown in Fig. 4.17. The coherence scale for $U_B = 1.5$ and $U_B = 2.0$ is almost linear and identical for the two sublattices between $1 < U_A \lesssim 2$. From this we conclude, that the system has still only one energy scale in this parameter regime. This behaviour of the energy scales does not apply for $U_B = 2.5$, where severe convergence problems made it impossible to investigate a larger parameter range. Even though the point of highest symmetry is $U_A = 2.5$ and there the DMFT converges, there is no convergence beyond this point for varying U_A in either direction.

Beyond $U_A \approx 2$ the behaviour of the scales for the two sublattices changes drastically for $U_B = 1.5$ and $U_B = 2.0$. The energy scales on sublattice A, $T_{A,c}$, drop and has a nearly linear but steeper slope on a log-scale, whereas the energy scale on sublattice B has a pronounced local minimum. The region where this behaviour of the energy scales sets in, denoted as U_A^1, depends on U_B.
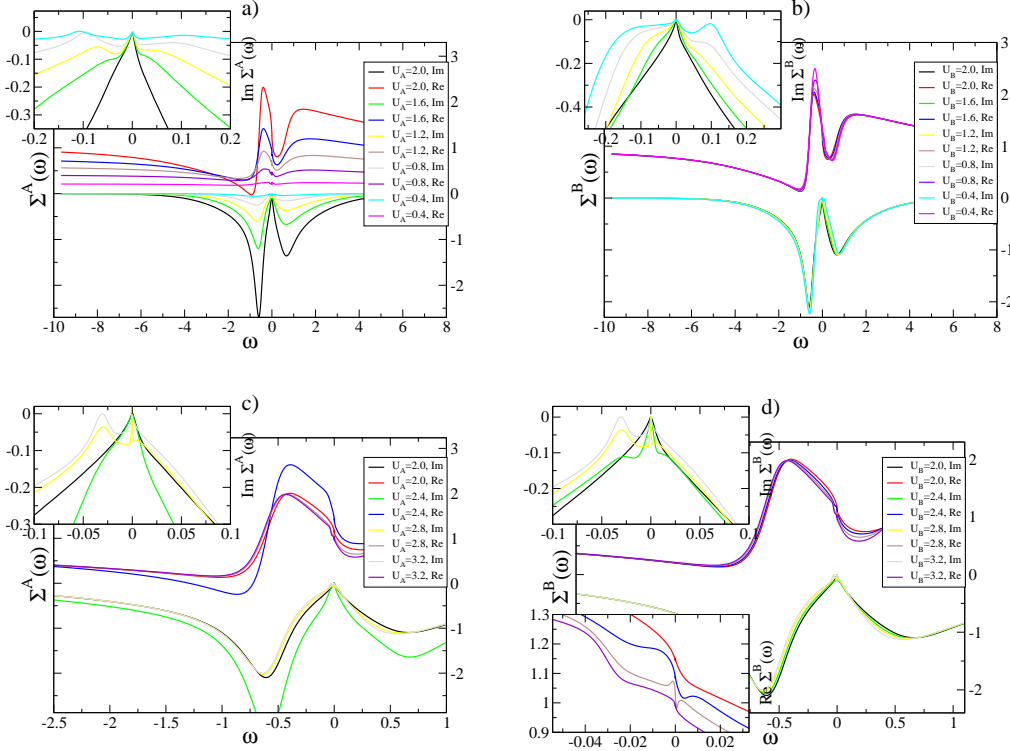
Figure 5.5.: Evolution of the Self energy $\Sigma^\alpha(\omega)$ for the A and B sublattices upon changing Coulomb interaction U_A, $U_B = 2$, $V_A = V_B = \varepsilon_c = 0.4$ and $\varepsilon_\alpha = -U_\alpha/2$ with $\alpha \in \{A, B\}$. The functions below zero show the real part of the self energy Re $\Sigma^\alpha(\omega)$ and the other ones the imaginary part Im $\Sigma^\alpha(\omega)$. The upper insets show an enlargement of Im $\Sigma^\alpha(\omega)$ and the lower inset depicts Re $\Sigma^\alpha(\omega)$.

Possible physical origin

For $U_A \lesssim U_B \leq 2$ the coherence scales for the PAM on a bipartite lattice are almost identical on each sublattice and have a reduced slope compared to the coherence scale of the homogeneous model. The quasiparticles on the two sublattices influence each other in a way that they build one coherent Fermi liquid upon both sublattices with a coherence scale which corresponds to a homogeneous system with $\overline{U} = \frac{1}{2}(U_A + U_B)$. This is possible because the coherence scales of the two sublattices are of the same order. The result is that the slopes for the coherence scales of the bipartite lattice model as a function of U_A are equal, $T_{A,c}(U_A) = T_{B,c}(U_A) \propto e^{-\gamma U_A/2}$, and have half the slope of the homogeneous model $T_c \propto e^{-\gamma U_A}$. Here γ is a proportionality factor. That would also explain why the slopes for $U_B = 1.5$ and $U_B = 2$ essentially match.

This simple reasoning is obviously wrong for very strong interactions as can be seen for $U_A > U_B$. In this regime the scales are strongly separated. It seems
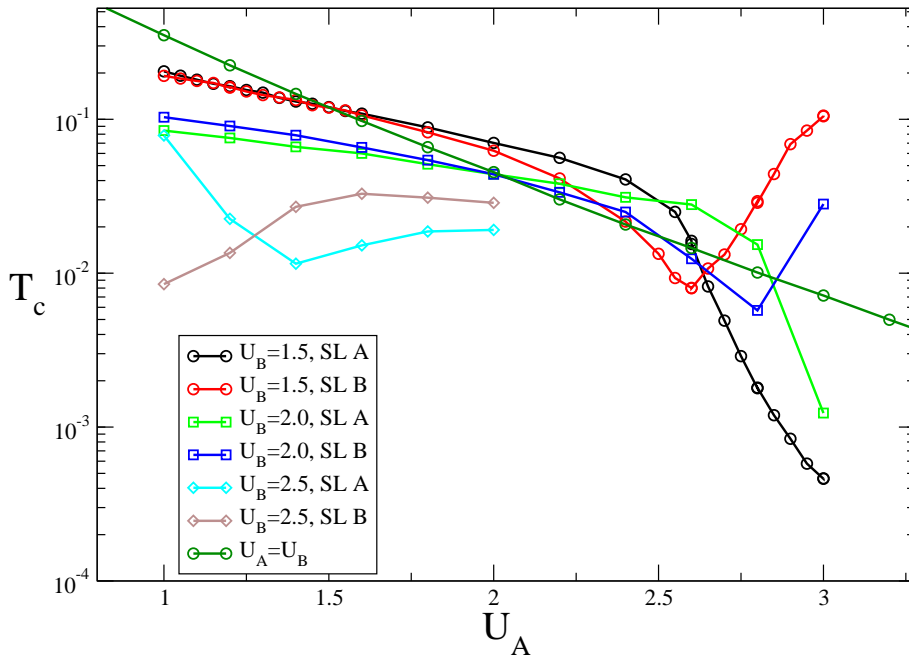
Figure 5.6.: Behaviour of the coherence temperature $T_{\alpha,c}$ on the sublattices (SL) $\alpha \in \{A, B\}$ as function of the Coulomb interaction U_A, $V_A = V_B = \varepsilon_c = 0.4$ and $\varepsilon_\alpha = -U_\alpha/2$.

that $T_{B,c}$ returns to its initial value while $T_{A,c}$ turns downwards and has a slope much smaller than for the homogeneous model. As a result the sublattices are decoupled and the electrons of sublattice A have no influence on the electrons of sublattice B and vice versa. The distinct energy scales do not allow for a single global coherent state and thus two independent Fermi liquids arise.

For $U_B = 2.5$ the scales for the sublattices are separated and approach each other while approaching the point of high symmetry, i.e. $U_A = U_B$. Due to convergence problems we were not able to approach $U_A = U_B$ any further. But here the energy scales of the two sublattices also split up for $U_A \ll U_B$ and, using the same line of argumentation as before, we end up with two independent Fermi liquids.

5.3.2. Varying the hybridization on one sublattice

Now we will investigate the bipartite system upon reducing the hybridization on one sublattice, here V_B, until it vanishes. In the case of $V_B = 0$ the impu-
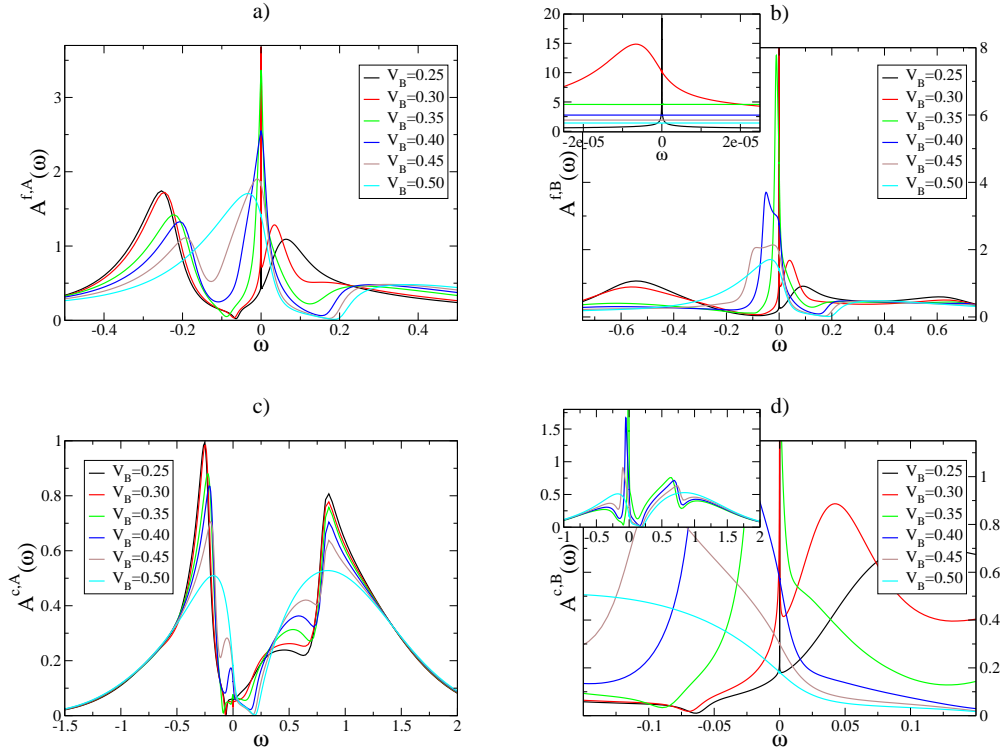
Figure 5.7.: Evolution of the impurity and conduction band spectral function for the A and B sublattices upon changing the hybridization V_B, $U_A = U_B = 1$, $V_A = \varepsilon_c = 0.5$ and $\varepsilon_\alpha = -U_\alpha/2$ with $\alpha \in \{A, B\}$.

rities of sublattice B are completely decoupled and thus the system shows the behaviour of a system with only half the number of impurity sites compared to the conduction electron sites.

Fig. 5.7 depicts the impurity and conduction band spectral functions, where the hybridization V_B ranges from 0.25 to 0.5 and the other parameters are fixed at $U_A = U_B = 1$, $V_A = \varepsilon_c = 0.5$ and $\varepsilon_\alpha = -U_\alpha/2$ with $\alpha \in \{A, B\}$. Again, for $V_B < 0.2$, the DMFT calculations suffer from convergence problems and we are not able to get results below $V_B = 0.25$ but $V_B = 0$.

In general, we can again identify the three-peak structure typical for Hubbard- and periodic Anderson models except for the A-sublattice spectral function for the conduction electrons (Fig. 5.7 c)), where we find nearly a gap, especially for $V_B < 0.3$. However, the width of the quasiparticle resonance is strongly reduced for $V_B < 0.3$ in Fig. a), b) and c). And although the conduction band spectral function $A^{c,A}(\omega)$ has not the general three-peak structure, it has still a small but finite amount of quasiparticle states at the Fermi energy and thus shows metallic behaviour.
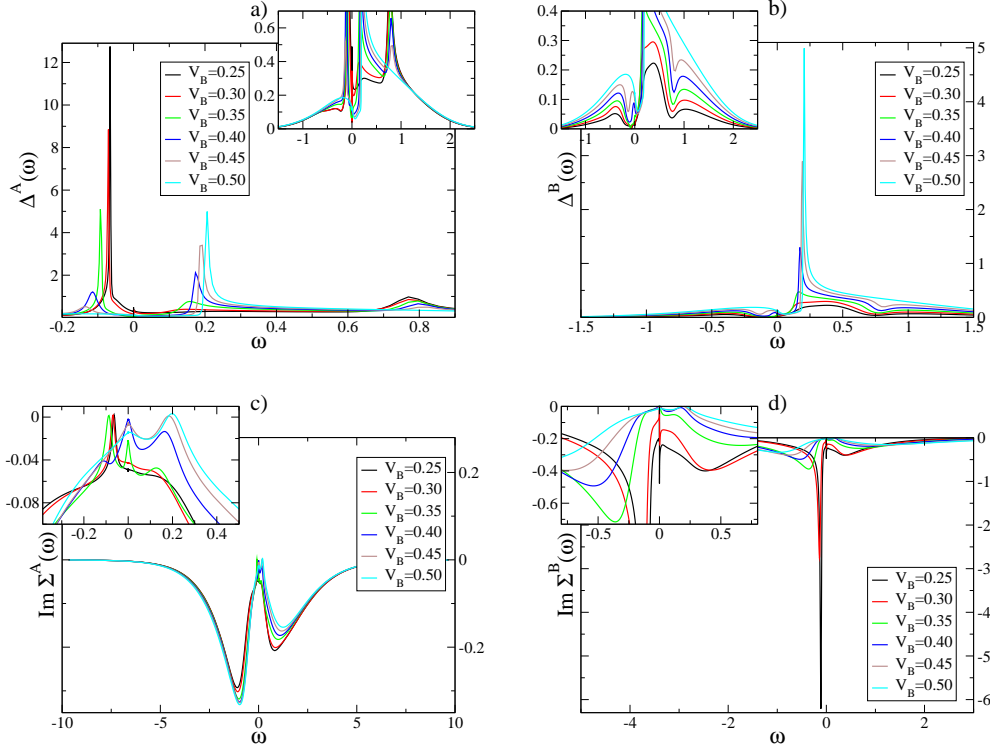
Figure 5.8.: Hybridization function $\Delta^\alpha(\omega)$ and imaginary part of the self energy $\mathrm{Im}\,\Sigma^\alpha(\omega)$ for the A and B sublattices upon changing the hybridization V_B, $U_A = U_B = 1$, $V_A = \varepsilon_c = 0.5$ and $\varepsilon_\alpha = -U_\alpha/2$ with $\alpha \in \{A, B\}$.

In Fig. 5.8 the hybridization functions a), b) and the imaginary part of the self energies c), d) for the A respectively B sublattices are shown. The hybridization functions show strong peaks around $\omega \approx -0.07$ and $\omega \approx 0.2$ for sublattice A and $\omega \approx 0.2$ for sublattice B. Due to the logarithmic discretization of the energy band the peaks have a crude resolution and are not smooth, which is already the case for $V_B = 0.5$, which resembles the case of the homogeneous PAM. Because of the high energies where the peaks are situated and their rough resolution we refrain to comment on them in the following. At the Fermi energy the hybridization function reduces for decreasing V_B as expected. The imaginary part of the self energies in figures c) and d) show the quadratic ω-dependence around the Fermi energy expected for Fermi liquids. The maxima of $\mathrm{Im}\,\Sigma^A(\omega)$ at $\omega \approx -0.07$ and $\omega \approx 0.2$ are remnants of the strong peaks in the hybridization function, mentioned earlier.

Again, using the real part of the self energy to determine the quasiparticle weight (Eq. 5.4) for each sublattice and using $Z_\alpha^{-1} \propto T_{\alpha,c}$, we can investigate the coherence scale of the PAM while successively decoupling one sublattice,
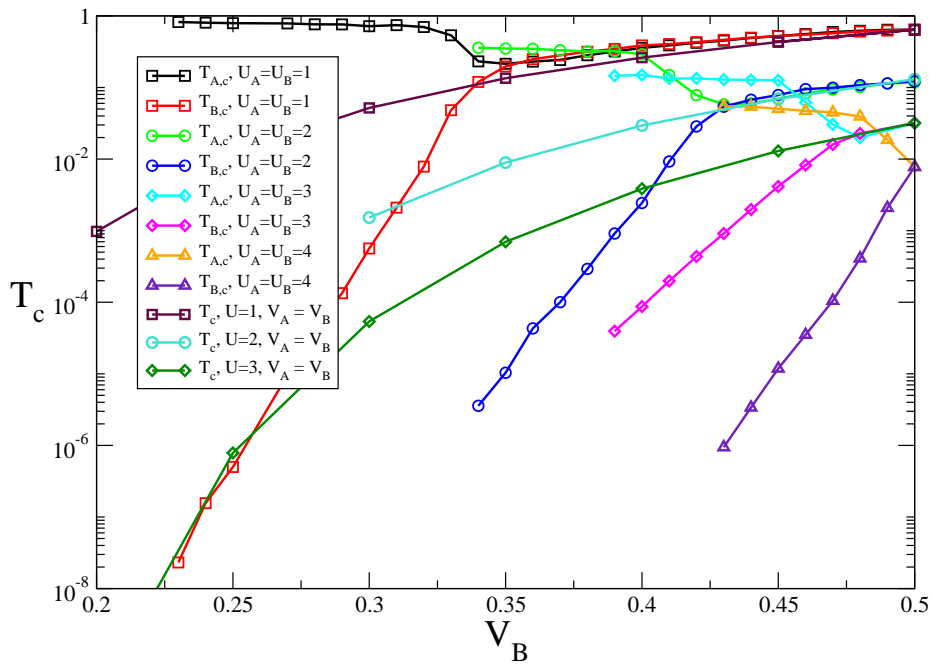
Figure 5.9.: Coherence scale for $V_A = \varepsilon_c = 0.5$. From right to left we start from a homogeneous PAM and reduce the hybridization V_B such that we approach the lattice where every second impurity is decoupled. Results for a homogeneous model, i.e. $V_A = V_B$, are also added.
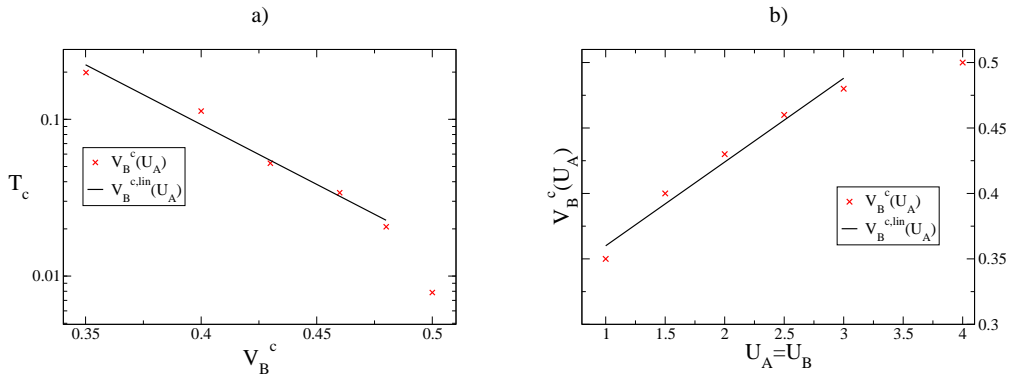
Figure 5.10.: Fig. a) depicts the coherence scale upon V_B^c, which shows good agreement with an exponential decrease. The data are extracted from Fig. 5.9. The last point is omitted in the linear regression as explained in the Text. Fig. b) shows that V^c might depend linear on the Coulomb interaction. Parameters are the same as in Fig. 5.9.

i.e. $V_B \to 0$ (see Fig. 5.9). Starting from the homogeneous PAM with $V_A = V_B = \varepsilon_c = 0.5$ and $U_A = U_B$, where the coherence scales have to be the same, i.e. $T_{A,c} = T_{B,c}$, we find that the scales for the two sublattices coincide upon decreasing V_B until V_B reaches a critical value V_B^c. For $U_A = U_B = 1 : V_B^c = 0.35$, for $U_A = U_B = 2 : V_B^c = 0.43$, for $U_A = U_B = 3 : V_B^c = 0.48$ and for $U_A = U_B = 1 : V_B^c = 0.5$. The scales are also slightly decreasing down to the critical V_B^c. Below that critical hybridization between the conduction band and the impurities on sublattice B, the coherence scales of the two sublattices split up. While $T_{A,c}$ increases a little bit higher than its initial value at $V_B = 0.5$ and then remains essentially constant, $T_{B,c}$ decreases exponentially. For different Coulomb interactions, the coherence scales $T_{B,c}$ have the same slope below V_B^c, except for $U_A = U_B = 3$, which we are not able to explain so far. We added also the results for $V_A = V_B$, i.e. the homogeneous PAM. Obviously the coherence scale is for $V_B^c < V_B < V_A$ nearly the same as for the bipartite lattice. For $U_A = U_B = 4$ the coherence scale for the different sublattices split as soon as we move away from $V_B = 0.5$. We assume that in this case $V_B^c \gtrsim 0.5$.

In Fig. 5.10 we depict the points (red crosses), where the coherence scales split up, i.e. $T_c(V_B^c)$. The black line is a linear regression and shows the exponential decrease of V_B^c with increasing Coulomb interaction $U_A = U_B$. We excluded $U_A = U_B = 4$ for the reason explained before, namely that we expect $V_{B,c} \gtrsim 0.5$. Fig. 5.10 b) depicts that V_B^c is almost proportional to $U_A = U_B$, where again the last data point is excluded. Extrapolating the black line to $U_A = U_B = 4$ shows that V_B^c would be larger than 0.5.
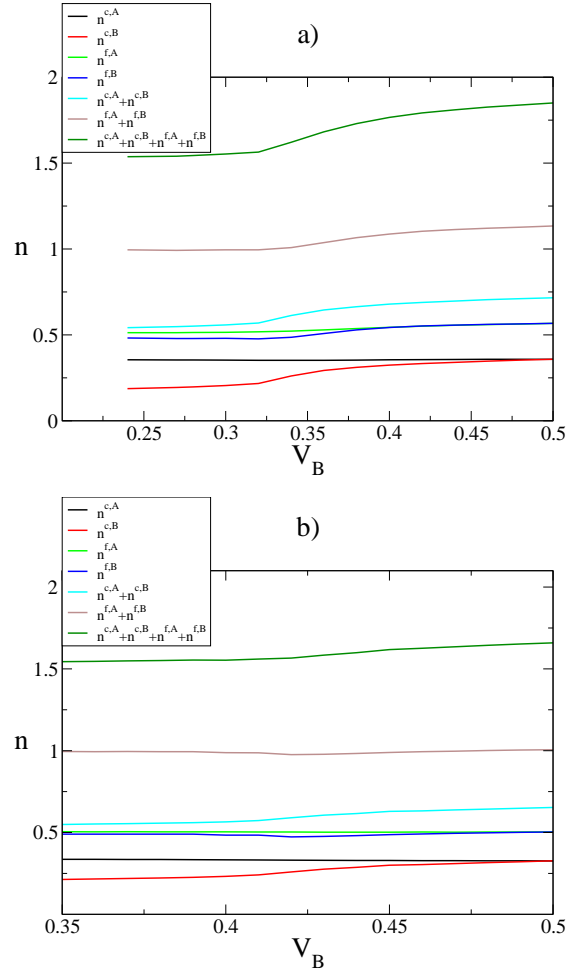
Figure 5.11.: Filling of the sublattices for f- and c-band, f- and c-band filling for the whole lattice and total filling as function of V_B for a) $U_A = U_B = 1$ and b) $U_A = U_B = 2$.

Taking a look at the fillings in Fig. 5.11 for different Coulomb interactions, we observe a strong influence on the c-band filling $n^{c,B}$ and the f-band filling $n^{f,B}$ for sublattice B (red and blue lines) and almost no influence for these quantities on sublattice A (black and green lines) upon reducing V_B. This coincides with the results of Fig. 5.9, where $T_{A,c}$ shows only minor changes compared to $T_{B,c}$. The total f-band filling $n^f_{tot} = n^{f,A} + n^{f,B}$ is close to one as expected, since we use $2\varepsilon_\alpha + U_\alpha = 0$ with $\alpha \in \{A, B\}$, and is even closer to one for small values of V_B, because then the system gains less energy for hopping processes from and to the impurity site compared to the cost from the Coulomb repulsion. V_B^c is also reflected in the fillings of the sublattices in Fig. 5.11 a) and b) such that upon decreasing V_B the fillings stop decreasing and stay essentially constant below V_B^c.

Possible physical origin

From Fig. 5.9 we learn that for $V_B^c < V_B < V_A$ the energy scales for the two sublattices are identical. I.e. a coherent Fermi liquid arises, which includes both sublattices. It might again be possible to describe the single coherence scale with an averaged parameter, i.e. in this case the hybridization average $\overline{V} = \frac{1}{2}(V_A + V_B)$.

For $V_B < V_B^c$ the energy scales of the two sublattices separate. While $T_{B,c}$ falls off rapidly for decreasing V_B, much faster than T_c for the homogeneous model, $T_{A,c}$ is essentially constant. I.e. the sublattices are again decoupled and the system hosts two independent Fermi liquids.

Again we find that for small interactions and for parameters describing the bipartite PAM are close to the homogeneous PAM, the system is described by a single energy scale. The larger the coherence scale of the corresponding homogeneous model, the longer the scales of the two sublattices coincide. Accordingly we observe to independent scales rather soon when at least one sublattice coherence scale becomes very small and parameters are varied.

5.4. Conclusions

In this chapter we investigated the behaviour of the PAM on a bipartite lattice for two different cases. On the one hand upon increasing the Coulomb interaction U_A on sublattice A and on the other hand on progressively decoupling one sublattice, which means in our case reducing the hybridization V_B on sublattice B. The development of the coherence temperature $T_{A/B,c}$ for sublattice A respectively B, was of special interest, especially for $V_B \to 0$, i.e. sublattice B is fully decoupled and we have effectively a system with half the number of impurity sites. But again convergence problems prohibited calculations for V_B down to zero.

The numerical investigation revealed that it is possible to find two distinct coherence scales, but not in all parameter regimes. Starting from the case of equal sublattices with a relatively large initial coherence scale, we only find a single energy scale which seems to be the same as for the homogeneous PAM but with averaged parameters $\bar{U} = \frac{1}{2}(U_A + U_B)$ and $\bar{V} = \frac{1}{2}(V_A + V_B)$. The system develops one coherent Fermi liquid for both sublattices.

On the other hand we found critical values for the hybridization and the Coulomb interaction, beyond which the picture of a single coherent Fermi liquid failed. We observed that two independent energy scales emerge. The

coherence scale on the sublattice where the parameters are varied show a strong influence on the parameter change. Whereas the coherence scale on the opposite sublattice is essentially independent upon the parameter change.

In the extreme case of $V_B \to 0$ we can extrapolate the coherence scales in Fig. 5.9 and assume that $T_{B,c}$ vanishes while $T_{A,c}$ stays constant. That would mean in this limit again only one energy scale exists. But this is just understandable, because for $V_B = 0$ the impurities on sublattice B have no influence on the system.

The convergence of the DMFT can be improved by using not only the last hybridization function to calculate the next cycle, but to use a linear combination of the last n functions.

In this thesis we only scratched the tip of the iceberg. For example, it would be interesting to know where the critical hybridization V_B^c stems from. Or in general, why two independent scales emerge. For example a simple second order perturbation theory might shed some light on this issue.

It would also be interesting to extend this method to more than two sublattices.

6. DMFT for the two-impurity Anderson model

In the last chapter we investigated a version of the PAM where we have the possibility to decouple half of the impurities from the conduction band. This was a first step to dilute the PAM towards the SIAM. In this chapter we develop a DMFT approach for two-impurity Anderson models (2IAM). The results can be compared to numerically exact NRG calculations which provides us with the opportunity to test the viability of this approach. But the important point is an easy expandability of this approach to multi-impurity systems which is less demanding than a direct multi-impurity NRG calculation.

6.1. Introduction

We investigate the 2IAM for two different lattice structures exemplarily. The first one is a semi-infinite chain of conduction electrons with two impurities coupled to the same end of the chain. The second configuration is an infinite chain where two impurities couple to different lattice sites with an even number of sites separating the impurities. We start by setting up the self-consistency equations for a general two-impurity Anderson model, then we derive the non-interacting Green functions for the concrete models. Then we show the DMFT results and compare the results for the second model to exact solutions from NRG calculations. The two-impurity NRG calculations for the comparison were performed by Dr. Andrew Mitchell. The NRG uses the z-trick with three different z, at most 10.000 energy states and the density matrix method to calculate dynamic quantities. Here also logarithmic Gaussians are used to broaden the δ-peaks for the dynamic quantities.

6.2. Effective medium for the 2IAM

To set up the DMFT cycle we first calculate the effective medium for a general two-impurity system, the impurities are labeled with A and B. Therefore we adopt Eq. (C.2)

$$
\mathcal{G}_{ii}^{eff} = G_{ii}^{lat} + \sum_j G_{ij}^{lat} \Sigma_{jj}^{lat} \mathcal{G}_{ji}^{eff} - G_{ii}^{lat} \Sigma_{ii}^{lat} \mathcal{G}_{ii}^{eff} \, .
$$

The equations simplify due to the fact that there are only two impurity sites, i.e. there are only four non-interacting Green functions $G_{\alpha\beta}(z)$ and effective mediums $\mathcal{G}_{\alpha\beta}^{eff}(z)$ and two self energies $\Sigma_\alpha(z)$, where $\alpha, \beta \in \{A, B\}$ refer to impurity A and B.

Eq. (C.2) yields a system of coupled linear equations

$$
\mathcal{G}_{AA}^{eff}(z) = G_{AA}(z) + G_{AB}(z) \, \Sigma_B(z) \, \mathcal{G}_{BA}^{eff}(z)
$$
$$
\mathcal{G}_{AB}^{eff}(z) = G_{AB}(z) + G_{AA}(z) \, \Sigma_A(z) \, \mathcal{G}_{AB}^{eff}(z)
$$
$$
\mathcal{G}_{BA}^{eff}(z) = G_{BA}(z) + G_{BB}(z) \, \Sigma_B(z) \, \mathcal{G}_{BA}^{eff}(z)
$$
$$
\mathcal{G}_{BB}^{eff}(z) = G_{BB}(z) + G_{BA}(z) \, \Sigma_A(z) \, \mathcal{G}_{AB}^{eff}(z)
$$

which is solved to

$$
\begin{aligned}
\mathcal{G}_{\alpha\alpha}^{eff}(z) = {} & \frac{1}{1 - G_{\bar\alpha\bar\alpha}(z) \, \Sigma_{\bar\alpha}(z)} \times \\
& \times \left(G_{\alpha\alpha}(z) + \Sigma_{\bar\alpha}(z) \left(G_{\alpha\bar\alpha}(z) G_{\bar\alpha\alpha}(z) - G_{\alpha\alpha}(z) G_{\bar\alpha\bar\alpha}(z) \right) \right) \, ,
\end{aligned}
\tag{6.1}
$$

where α labels one impurity and $\bar\alpha$ the residual one.

Thus the hybridization functions are

$$
\Delta_\alpha(z) = z - \varepsilon^f - \Sigma_\alpha(z) - \left[\mathcal{G}_{\alpha\alpha}^{eff}(z) \right]^{-1} \, .
$$

Since both self energies contribute to each hybridization function, the DMFT cycle follows exactly the scheme from Chap. 5, which is illustrated in Fig. 5.1.

6.3. Infinite chain

The first model we analyze consists of a one-dimensional, infinite conduction band and the impurity sites couple to different conduction band sites and have an even number of conduction band sites in between. Fig. 6.1 illustrates the model with $2n$ conduction band sites between the impurities. For this model
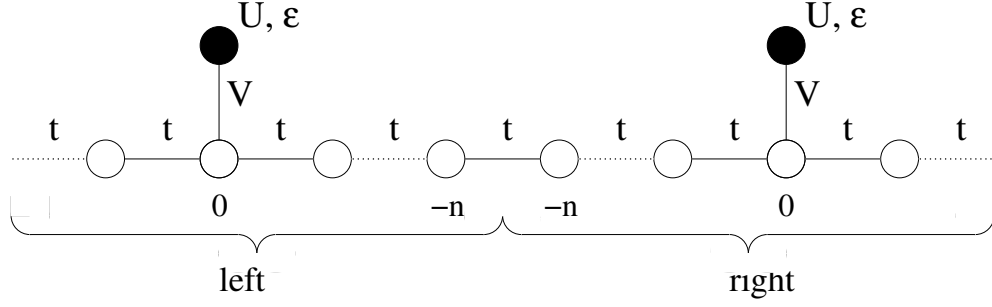
Figure 6.1.: A version of a one dimensional two-impurity Anderson model with an infinite conduction band with hopping amplitudes t and the impurities couple to different sites via a hybridization V with an even number of conduction band sites in between. U is the on-site Coulomb repulsion and ε is the on-site energy per electron. The model can be naturally divided into a left and a right part.

the Hamiltonian is

$$
\begin{aligned}
H = & \sum_{\substack{i=-n \\ \sigma,\alpha}}^{\infty} t \left(c_{i\sigma\alpha}^{\dagger} c_{i+1\sigma\alpha} + c_{i+1\sigma\alpha}^{\dagger} c_{i\sigma\alpha} - \mu c_{i\sigma\alpha}^{\dagger} c_{i\sigma\alpha} \right) \\
& + \sum_{\sigma} t \left(c_{-n\sigma L}^{\dagger} c_{-n\sigma R} + c_{-n\sigma R}^{\dagger} c_{-n\sigma L} \right) + \sum_{\sigma\alpha} V \left(f_{\sigma\alpha}^{\dagger} c_{0\sigma\alpha} + c_{0\sigma\alpha}^{\dagger} f_{\sigma\alpha} \right) \quad (6.2) \\
& + \sum_{\sigma\alpha} \varepsilon f_{\sigma\alpha}^{\dagger} f_{\sigma\alpha} + \sum_{\alpha} U f_{\uparrow\alpha}^{\dagger} f_{\uparrow\alpha} f_{\downarrow\alpha}^{\dagger} f_{\downarrow\alpha} \,,
\end{aligned}
$$

where $c_{i\sigma\alpha}^{(\dagger)}$ annihilates (creates) an electron on site i with spin σ and $\alpha \in \{L, R\}$ labels the left or right hand site. Accordingly the $f_{\sigma\alpha}^{(\dagger)}$ is the annihilation (creation) operator for an electron at the left or right hand site with spin σ. t is the nearest neighbour hopping amplitude, V the hybridization strength between the impurity site and the conduction band, ε the on-site energy for each electron on the f-level and U is the on-site Coulomb repulsion for a doubly occupied impurity. The f-levels couple always to conduction band site zero, and the number of conduction band sites in between the impurity sites is $2n$.

For the DMFT equations we need the non-interacting Green functions

$$
G_{\alpha\beta} = \langle\langle f_{\alpha}; f_{\beta}^{\dagger} \rangle\rangle_z, \quad \text{with } \alpha, \beta \in \{L, R\} \,.
$$

The spin indices are skipped as usual.

Performing a basis transformation to even and odd operators

$$
c_{i,e/o}^{(\dagger)} = \frac{1}{\sqrt{2}} \left(c_{iL}^{(\dagger)} \pm c_{iR}^{(\dagger)} \right) \quad \text{and}
$$

$$
f_{e/o}^{(\dagger)} = \frac{1}{\sqrt{2}} \left(f_{L}^{(\dagger)} \pm f_{R}^{(\dagger)} \right),
$$

the left and right hand site of the non-interacting Hamiltonian (6.2) decouple to

$$H^0 = \sum_{\substack{i=-n \\ \sigma,\alpha\in\{e,o\}}}^{\infty} t \left(c_{i\sigma\alpha}^\dagger c_{i+1\sigma\alpha} + c_{i+1\sigma\alpha}^\dagger c_{i\sigma\alpha} - \frac{\mu}{t} c_{i\sigma\alpha}^\dagger c_{i\sigma\alpha} \right) \tag{6.3}$$

$$+ \sum_{\sigma,\alpha\in\{e,o\}} \left[+\varepsilon f_{\sigma\alpha}^\dagger f_{\sigma\alpha} + V \left(f_{\sigma\alpha}^\dagger c_{0\sigma\alpha} + c_{0\sigma\alpha}^\dagger f_{\sigma\alpha} \right) \right] \tag{6.4}$$

$$+ t \left(c_{-n\sigma e}^\dagger c_{-n\sigma e} - c_{-n\sigma o}^\dagger c_{-n\sigma o} \right). \tag{6.5}$$

Introducing Green functions for the even/odd-basis

$$G_{\gamma\delta(z)} = \langle\langle f_\gamma; f_\delta^\dagger \rangle\rangle_z, \quad \gamma, \delta \in \{e,o\},$$

the non-interacting Green functions in the left/right-basis can be expressed as

$$G_{LL}(z) = G_{RR}(z) = \frac{1}{2} \left(G_{ee}(z) + G_{oo}(z) \right) \text{ and}$$

$$G_{LR}(z) = G_{RL}(z) = \frac{1}{2} \left(G_{ee}(z) - G_{oo}(z) \right).$$

Due to the decoupling of the Hamiltonian in the even/odd-basis, $G_{eo}(z)$ and $G_{oe}(z)$ vanish. Employing the equations of motion (B.3) we find

$$
\begin{aligned}
[G_{ee}(z)]^{-1} &= z - \varepsilon - \frac{V^2}{z + \mu - X_n^-(z) - X(z)} \text{ and} \\
[G_{oo}(z)]^{-1} &= z - \varepsilon - \frac{V^2}{z + \mu - X_n^+(z) - X(z)}
\end{aligned}
\tag{6.6}
$$

where $X(z)$ is defined self-consistently and $X_n^\pm(z)$ are continued fractions of depth n

$$X(z) = \frac{t^2}{z + \mu - X(z)}$$

$$X_n^\pm(z) = \frac{t^2}{z + \mu - \dfrac{t^2}{z+\mu-\cdots\frac{t^2}{z+\mu\pm t}}}.$$

DMFT results for the infinite chain 2IAM

With the knowledge of the Green functions (6.6) and the self-consistency condition (6.1) the DMFT method can be applied. Fig. 6.2 shows the resulting spectral a) and hybridization b) function for $V = 0.5$, $\varepsilon = -U/2$ and $t = 1$. Due to the symmetry of the Hamiltonian the results are only shown for one impurity.
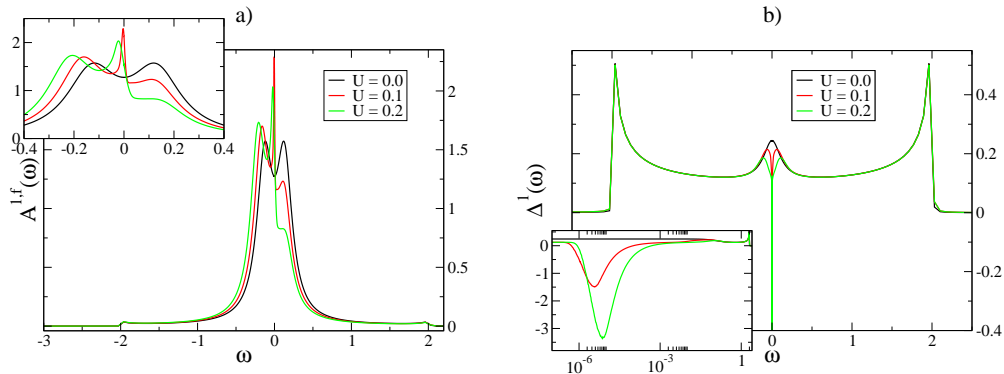
Figure 6.2.: The spectral function a) and the hybridization function b) for the 2IAM with an infinite chain and the impurities are separated by two conduction band sites (compare to Fig. 6.1, $n = 0$). $V = 0.5$, $\varepsilon = -U/2$ and $t = 1$.

In the non-interacting case the spectral function is as expected symmetric around the Fermi energy. But for increasing interactions it becomes asymmetric and develops a peak around the Fermi energy. The inset shows an enlargement around $\omega = 0$.

The origin of the unphysical asymmetry in the impurity spectral function is found in the hybridization function depicted in b). The inset shows the positive frequency axis on a logarithmic scale. The peaks at the band energies $\omega \pm 2$ with its coarse resolution due to the logarithmic discretization are not causing the unphysical behaviour. The problems stem from the negative double peak close to $\omega = 0$. Calculating the on-site- and hopping energies, ε_n and t_n, from the hybridization function for the NRG involves taking square roots, e.g. see [25], which happen to be negative for negative spectral function values. Therefore the DMFT cannot update the self energy and the method breaks down.

The spectral- and hybridization functions in Fig. 6.2 for $U = 0.1$ and $U = 0.2$ thus do not show converged results. The simplest way to resolve this problem is to cut off negative values. But after convergence the results had still all low energy features cut off and the results are unimportant if correct at all.

Fig. 6.3 shows the spectral function a) and the hybridization function b) for the 2IAM with an infinite chain. The impurities are separated by 22 conduction band sites, $V = 0.5$, $\varepsilon = -U/2$ and $t = 1$. Of course the DMFT converged in the non-interacting case. But it breaks down already for $U = 0.2$, with negative sections in the effective hybridization. The inset depicts the hybridization function on a logarithmic scale. It shows that the hybridization function for
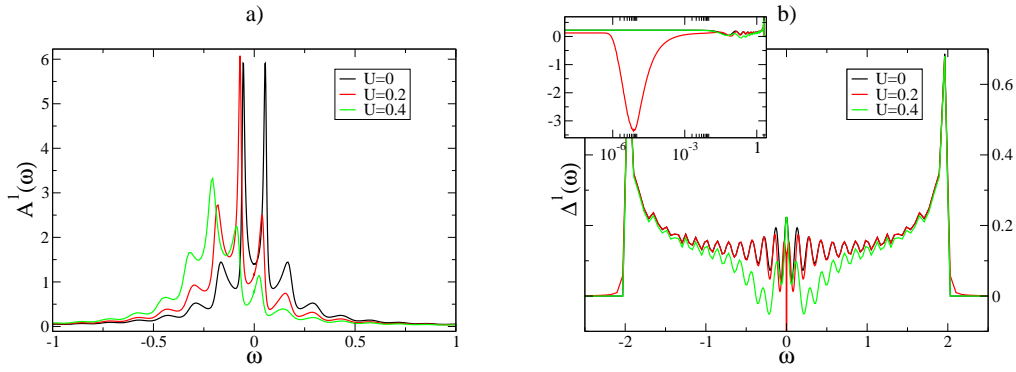
Figure 6.3.: The spectral function a) and the hybridization function b) for the 2IAM with an infinite chain and the impurities are separated by 22 conduction band sites (confer to Fig. 6.1, $n = 20$). $V = 0.5$, $\varepsilon = -U/2$ and $t = 1$.

$U = 0.2$ at $\omega = 0$ is continuous.

At last we want to point out that the negative parts in the spectral function are smooth and seem not to be numerical artifacts. We conclude that the non-local parts of the self energy, which are missing in the DMFT approximation, are important to capture the essential physics.

6.4. Semi-infinite chain

The second model we investigate is also one-dimensional, but the conduction band is a semi-infinite chain with constant nearest neighbour hopping t, where two impurities couple to the first site of the chain via a hybridization strength V_α. The impurities have as usual an on-site Coulomb interaction U_α, which energetically disfavours double occupation, and an on-site energy ε_α. The second quantized Hamiltonian for this model is

$$H = \sum_{i=0,\sigma}^{\infty} t \left(c_{i\sigma}^{\dagger} c_{i+1\sigma} + c_{i+1\sigma}^{\dagger} c_{i\sigma} \right)$$
$$+ \sum_{\alpha \in \{A,B\}} \left(\sum_{\sigma} \left[V_\alpha \left(c_{0\sigma}^{\dagger} f_{\alpha\sigma} + f_{\alpha\sigma}^{\dagger} c_{0\sigma} \right) + \varepsilon_\alpha f_{\alpha\sigma}^{\dagger} f_{\alpha\sigma} \right] + U_\alpha f_{\alpha\uparrow}^{\dagger} f_{\alpha\uparrow} f_{\alpha\downarrow}^{\dagger} f_{\alpha\downarrow} \right),$$

$$(6.7)$$

where $c_{i\sigma}^{(\dagger)}$ is the annihilation (creation) operator for a conduction electron on site i with spin σ and $f_{\alpha\sigma}^{(\dagger)}$ is the annihilation (creation) operator for an electron on the impurity site $\alpha \in \{A, B\}$. For convenience, the model is chosen to be symmetric, i.e. $V_A = V_B = V$, $\varepsilon_A = \varepsilon_B = \varepsilon$ and $U_A = U_B = U$. Fig. 6.4
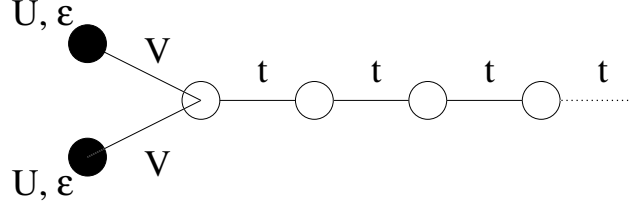
Figure 6.4.: Semi-infinite chain of non-interacting electrons with a nearest neighbour hopping amplitude t. On the left hand site two identical impurity sites are coupled to the chain with a hybridization strength V. On the impurity sites the electrons experience an on-site energy ε and suffer an energy penalty U for double-occupation.

illustrates the semi-infinite chain model.

Using the equations of motion (B.3), the non-interacting Green functions of the simplified version are

$$\langle\langle f_\alpha; f_\alpha^\dagger\rangle\rangle_z = G_{\alpha\alpha}(z) = \frac{1}{z - \varepsilon - \tilde{\Delta}(z)}$$

$$\langle\langle f_\alpha; f_{\bar\alpha}^\dagger\rangle\rangle_z = G_{\alpha\bar\alpha}(z) = \frac{\tilde{\Delta}(z)}{z - \varepsilon} G_{\alpha\alpha}(z) \quad \text{with}$$

$$\tilde{\Delta}(z) = \frac{V^2}{z - \frac{V^2}{z-\varepsilon} - t^2 X(z)} = \frac{V^2 X(z)(z - \varepsilon)}{z - \varepsilon - V^2 X(z)} \quad \text{and}$$

$$X(z) = \frac{1}{z - t^2 X(z)},$$

where $\bar\alpha = B$ if $\alpha = A$ and vice versa. We dropped the spin indices because our calculations are performed in the paramagnetic phase.

Now we have all ingredients to do a full self-consistent DMFT calculation. Adopting the Dyson equation

$$\underline{\underline{G}}^{-1} = \left[\underline{\underline{G}}^0\right]^{-1} - \underline{\underline{\Sigma}}, \tag{6.8}$$

where the matrix form of the non-interacting Green function $\left[\underline{\underline{G}}^0\right]^{-1}$ and the local self energy $\underline{\underline{\Sigma}}$ are

$$\underline{\underline{G}}^0 = \begin{pmatrix} G_{AA} & G_{AB} \\ G_{BA} & G_{BB} \end{pmatrix} \quad \text{and} \quad \underline{\underline{\Sigma}} = \begin{pmatrix} \Sigma_{AA} & 0 \\ 0 & \Sigma_{BB} \end{pmatrix},$$

we can calculate the full interacting Green functions for the impurity sites.

DMFT results for the semi-infinite chain 2IAM

Fig. 6.5 depicts the spectral function a) and hybridization function b) for the 2IAM for $V = 0.5$, $\varepsilon = -U/2$ and $t = 1$. Obviously the DMFT breaks down
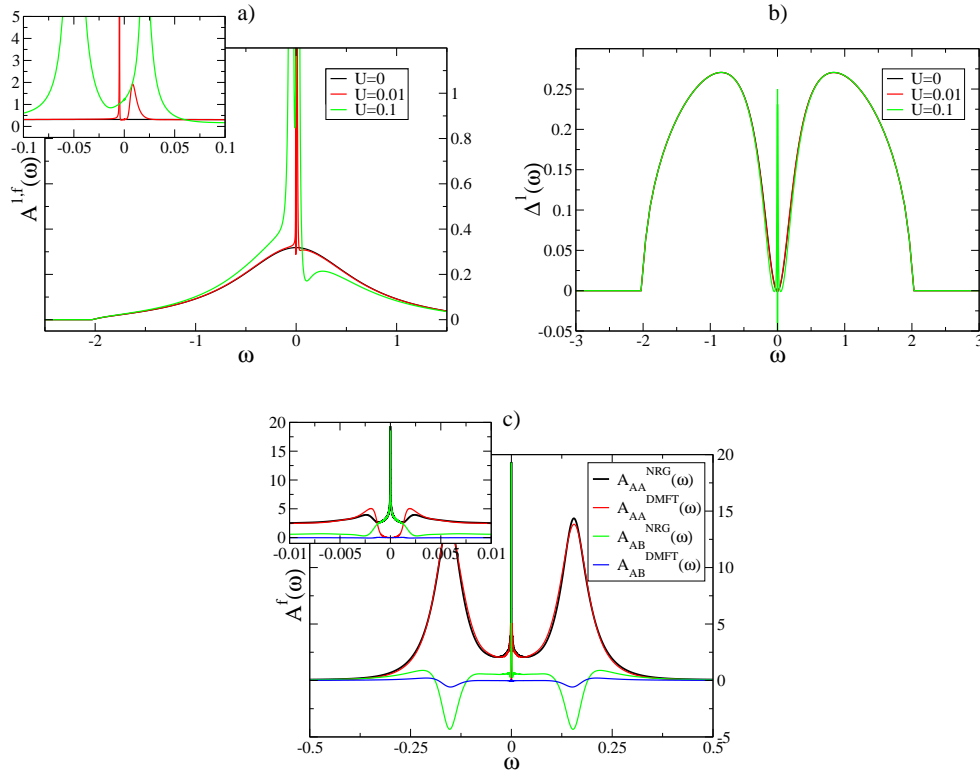
Figure 6.5.: The spectral function a) and the hybridization function b) for the 2IAM with a semi-infinite chain computed with the DMFT. $V = 0.5$, $\varepsilon = -U/2$ and $t = 1$. Fig. c) compares the spectral functions from exact NRG calculations with (NRG) and without (DMFT) the non-local self energy components. Here $U = 0.3$, $V = 0.08$, $\varepsilon = -U/2$ and $t = 0.5$.

due to negative parts in the hybridization function. Thus the spectral function shows the unphysical asymmetry. Fig. c) compares the spectral functions $A_{AA}(\omega)$ and $A_{AB}(\omega)$, calculated from exact NRG self energy results, with (black and green line) and without (red and blue line) the off-diagonal self energy contributions with parameters $U = 0.3$, $V = 0.08$, $\varepsilon = -U/2$ and $t = 0.5$. Obviously, the diagonal and the off-diagonal spectral functions are missing the resonance at the Fermi energy in the local self energy approximation used in the DMFT. Thus we conclude that the failure of the DMFT is originated in the negligence of the off-diagonal terms $\Sigma_{AB} = \Sigma_{BA}$ in the DMFT approximation.

A solution for this problem is to perform again a basis transformation to even and odd operators

$$f_{e/o}^{(\dagger)} = \frac{1}{\sqrt{2}} \left(f_A^{(\dagger)} \pm f_B^{(\dagger)} \right)$$

$$c_{i,e/o}^{(\dagger)} = \frac{1}{\sqrt{2}} \left(c_{iA}^{(\dagger)} \pm c_{iB}^{(\dagger)} \right).$$

The Dyson equation simplifies to

$$\underline{\underline{G}}^{-1} = \begin{pmatrix} G_{ee} & 0 \\ 0 & G_{oo} \end{pmatrix}^{-1} - \begin{pmatrix} \Sigma_{ee} & 0 \\ 0 & \Sigma_{oo} \end{pmatrix}, \tag{6.9}$$

where $G_{LL} = G_{RR} = G_{ee} + G_{oo}$ and $G_{LR} = G_{RL} = G_{ee} - G_{oo}$. Important is that the self energy has a diagonal form in the new basis. The off-diagonal self energies are absorbed into $\Sigma_{ee} = \Sigma_{LL} + \Sigma_{LR}$ and $\Sigma_{oo} = \Sigma_{LL} - \Sigma_{LR}$. The self-consistency conditions are

$$\Delta_\alpha = z - \varepsilon - \Sigma_\alpha - \left[\mathcal{G}_\alpha^{eff} \right]^{-1} \quad \text{with}$$

$$\mathcal{G}_\alpha^{eff} = \frac{G_\alpha - G_\alpha \, G_{\bar\alpha} \, \Sigma_{\bar\alpha}}{1 - G_{\bar\alpha} \, \Sigma_{\bar\alpha}}, \tag{6.10}$$

where $\bar\alpha = oo$ if $\alpha = ee$ and vice versa. Even though the Dyson equation Eq. (6.9) seem to decouple, the DMFT equations do not because both self energies contribute in the effective hybridization function Δ_α (6.10).

Fig. 6.6 shows the NRG and DMFT results in the even/odd-basis. In a) the even and odd spectral functions $A_{ee}(\omega)$ and $A_{oo}(\omega)$ computed with the NRG are compared to results from the DMFT for $U = 0.3$, $V = 0.08$, $\varepsilon = -U/2$ and $t = 0.5$. Figure b) depicts the corresponding hybridization functions. All spectral functions show the same high energy features at roughly $\pm U/2$. The even spectral functions show a qualitative agreement, but the DMFT result is smaller and has a broader quasiparticle peak at the Fermi energy than the NRG result. The odd spectral functions are in good quantitative agreement
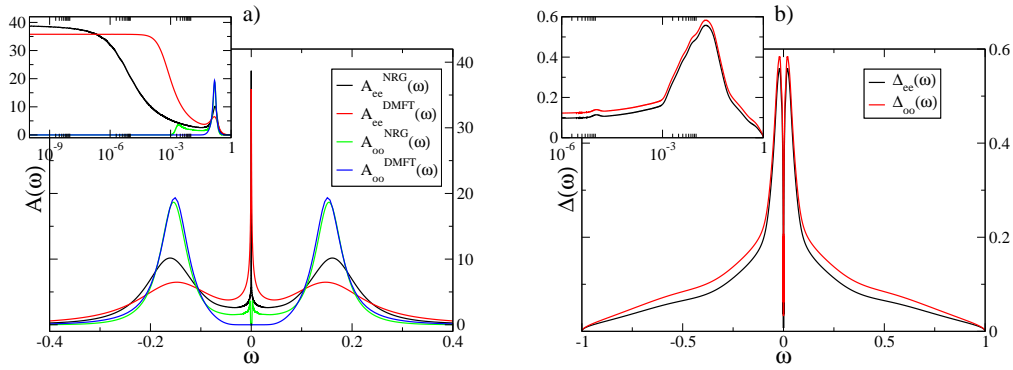
Figure 6.6.: a) Numerically exact (NRG) and approximated (DMFT) even and odd spectral functions for the 2IAM with $U = 0.3$, $V = 0.08$, $\varepsilon = -U/2$ and $t = 0.5$. b) shows the converged even- and odd spectral functions.

except for $0.001 \lesssim \omega \lesssim 0.1$, where the NRG result shows a very broad and relative small peak structure which is completely absent in the DMFT. Finally the hybridization function in Fig. b) is positive in the whole support and the DMFT converged.

6.5. Conclusions

In this chapter we have performed DMFT calculations for two different 2IAM's. We observed that unphysical negative values in the hybridization function usually led to a breakdown of the DMFT calculations. For the second model we performed also NRG calculations which provided us with the full self energy Matrix. We observed from comparison of the spectral functions, computed from the self energy from the NRG, that the negligence of the off-diagonal self energy contributions lead to wrong low energy physics. Without the off-diagonal self energy contributions the Kondo resonance at $\omega = 0$ vanishes. This suggests that the local self energy approximation, central to the DMFT, neglects important interactions between the two impurities and thus produces unphysical negative values in the hybridization function, resulting in the breakdown of the DMFT.

A basis transformation for the second model, such that the Dyson equation becomes diagonal, and rewriting the self-consistency equations in terms of the Green functions for the new basis turns out to reduce the problems we encountered so far. The hybridization function stays positive and the DMFT converges. The resulting Green function is in qualitative agreement with the

the numerical exact results from the NRG calculations.

We showed that it is possible to capture the essential physics of the 2IAM within the DMFT. In future work this method could be extended in several ways. Our calculations concentrated on models with a high symmetry, where a simple basis transformation to an even/odd-basis removed off-diagonal self energy terms, such that the self energy became diagonal. This is not possible for two inequivalent impurities. Another possibility is to extend this method to multi-impurity models or change the geometry of the bath.

A. f-band Green function for the PAM

To apply the DMFT calculations for the PAM we need the self-consistency equation for the given Hamiltonian (3.1), i.e. especially the local f-band Green function. We want to use the results for the Hubbard model (see Chap. 3.4), so we just integrate out the conduction band degrees of freedom of the PAM.

We start out with an action representation for the Hamiltonian of the PAM in the grand canonical ensemble in k-space and using Matsubara frequencies. Assuming the self energy is known, the action is

$$S_{PAM}[\bar{\chi}, \chi, \bar{\phi}, \phi] = \sum_{\mathbf{k},n,\sigma} \Big[\bar{\chi}_{\mathbf{k},n,\sigma} \left(-i\omega_n + \varepsilon_{\mathbf{k}} - \mu \right) \chi_{\mathbf{k},n,\sigma} +$$
$$+ \bar{\phi}_{\mathbf{k},n,\sigma} \left(-i\omega_n + \varepsilon^f + \Sigma(\mathbf{k}, i\omega_n) \right) \phi_{\mathbf{k},n,\sigma} +$$
$$+ V \left(\bar{\chi}_{\mathbf{k},n,\sigma} \phi_{\mathbf{k},n,\sigma} + \bar{\phi}_{\mathbf{k},n,\sigma} \chi_{\mathbf{k},n,\sigma} \right) \Big].$$

The action can be rewritten as

$$S_{PAM}[\bar{\chi}, \chi, \bar{\phi}, \phi] = \sum_{\mathbf{k},n,\sigma} \Big[\bar{\chi}_{\mathbf{k},n,\sigma} \left(-i\omega_n + \varepsilon_{\mathbf{k}} - \mu \right) \chi_{\mathbf{k},n,\sigma} +$$
$$+ \bar{\phi}_{\mathbf{k},n,\sigma} \left(-i\omega_n + \varepsilon^f + \Sigma(\mathbf{k}, i\omega_n) - \frac{V^2}{-i\omega_n + \varepsilon_{\mathbf{k}} - \mu} \right) \phi_{\mathbf{k},n,\sigma} \Big]$$

where the fields for the conduction band have been rescaled to

$$\bar{\chi}_{\mathbf{k},n,\sigma} \to \bar{\chi}_{\mathbf{k},n,\sigma} + \bar{\phi}_{\mathbf{k},n,\sigma} \frac{V}{-i\omega_n + \varepsilon_{\mathbf{k}} - \mu} \quad \text{and}$$
$$\chi_{\mathbf{k},n,\sigma} \to \chi_{\mathbf{k},n,\sigma} + \frac{V}{-i\omega_n + \varepsilon_{\mathbf{k}} - \mu} \phi_{\mathbf{k},n,\sigma}.$$

Integrating out the conduction band degrees of freedom, the effective action is

$$S_{eff}[\bar{\phi}, \phi] = \sum_{\mathbf{k},n,\sigma} \bar{\phi}_{\mathbf{k},n,\sigma} \left(-i\omega_n + \varepsilon^f + \Sigma(\mathbf{k}, i\omega_n) + \frac{V^2}{i\omega_n - \varepsilon_{\mathbf{k}} + \mu} \right) \phi_{\mathbf{k},n,\sigma}$$

and the f-band Green function after analytical continuation, $i\omega_n \to z = \omega + i\delta$, is

$$G^f(\mathbf{k}, z) = \frac{1}{z - \varepsilon^f - \Sigma(\mathbf{k}, z) - \frac{V^2}{z - \varepsilon_{\mathbf{k}} + \mu}} \, .$$

A. f-band Green function for the PAM

Introducing again the DOS $\rho(\varepsilon) = \sum_{\mathbf{k}} \delta(\varepsilon - \varepsilon_{\mathbf{k}})$ and using the locality of the self energy the local f-band Green function for the PAM is

$$G^f(z) = \int_{-\infty}^{\infty} \frac{\rho(\varepsilon)}{z - \varepsilon^f - \Sigma(z) - \frac{V^2}{z - \varepsilon + \mu}} d\varepsilon , \qquad (A.1)$$

and the self-consistency condition is

$$\Delta(z) = z - \varepsilon^f - \Sigma(z) - \left[G^f(z) \right]^{-1} .$$

B. Equation of motion and the conduction band Green function for the PAM

The retarded Green function for a given Hamiltonian $H(c_{\mathbf{k},\sigma}, c_{\mathbf{k},\sigma}^\dagger)$ consisting of creation and annihilation operators $c_{\mathbf{k},\sigma}^\dagger$, $c_{\mathbf{k},\sigma}$ with momentum $\mathbf{k}$ and spin σ is defined as

$$G_\sigma(\mathbf{k}, z) = \langle\langle c_{\mathbf{k},\sigma}; c_{\mathbf{k},\sigma}^\dagger \rangle\rangle_z, \tag{B.1}$$

with

$$\langle\langle A; B\rangle\rangle_z := -i \int_{-\infty}^\infty \Theta(t) e^{izt} \langle [A(t), B]_\eta \rangle dt \tag{B.2}$$

where $\Theta(t)$ is the Heaviside theta-function, $\eta = \pm$ for fermions/bosons, A, B are operators, where $A(t)$ refers to the Heisenberg representation and $z = \omega + i0^+$ is a frequency with an additional convergence-generating factor. The expectation value $\langle \ldots \rangle$ is as usual

$$\langle \ldots \rangle = \frac{Tr(\ldots \exp(-\beta(H - \mu N)))}{Tr(\exp(-\beta(H - \mu N)))}.$$

Using Eq. (B.1), (B.2) and the equations of motion (EOM) Eq. (B.3)

$$
\begin{aligned}
\langle [A, B]_\eta \rangle &= z\langle\langle A; B\rangle\rangle_z + \langle\langle [H, A]_- ; B\rangle\rangle_z \\
&= z\langle\langle A; B\rangle\rangle_z - \langle\langle A; [H, B]_-\rangle\rangle_z
\end{aligned}
\tag{B.3}
$$

we are able to establish a connection between the Green function for the impurity band $G_\sigma^f(\mathbf{k}, z) = \langle\langle f_{\mathbf{k},\sigma}; f_{\mathbf{k},\sigma}^\dagger \rangle\rangle_z$ and the conduction band $G_\sigma^c(\mathbf{k}, z) = \langle\langle c_{\mathbf{k},\sigma}; c_{\mathbf{k},\sigma}^\dagger \rangle\rangle_z$ of the periodic Anderson model (3.1):

$$
\begin{aligned}
G_\sigma^c(\mathbf{k}, z) &= \frac{1}{z - \varepsilon_{\mathbf{k}} + \mu} + \frac{V^2}{(z - \varepsilon_{\mathbf{k}} + \mu)^2} G_\sigma^f(\mathbf{k}, z) \\
&= \frac{1}{z - \varepsilon_{\mathbf{k}} + \mu - \frac{V^2}{z - \varepsilon^f - \Sigma(\mathbf{k}, z)}}
\end{aligned}
$$

Using the locality of the self energy and the DOS $\rho(\varepsilon)$, the local spin-independent conduction band Green function for the periodic Anderson model is

$$G^c(z) = \int_{-\infty}^{\infty} \frac{\rho(\varepsilon)}{z - \varepsilon + \mu - \frac{V^2}{z - \varepsilon^f - \Sigma(z)}} d\varepsilon. \tag{B.4}$$

C. A further DMFT self-consistence scheme

In the following we introduce another way to compute the self-consistent DMFT equations which is more adapted for our purpose. The ideas are brought forward by Priv.-Doz. Dr. Ralf Bulla.

In Chap. 3 we learned that in the limit of infinite dimensions a given lattice model can be mapped onto a single impurity Anderson model. In this case there exists a SIAM with a self energy $\Sigma^{SIAM}(z)$ exactly the same as for the lattice model $\Sigma_{ii}^{lat}(z)$. Viewed as a functional, the lattice model self energy can be considered as the single impurity model in terms of a given effective medium $\mathcal{G}^{eff}(z)$,

$$\Sigma_{ii}^{lat}(z) = \Sigma^{SIAM}[\mathcal{G}^{eff}(z), U, T], \tag{C.1}$$

where U and T are the Coulomb interaction and the temperature of the system. This functional dependence can be understood by writing down the diagrams for the SIAM and the lattice model.

First take a look at the single impurity model. After integrating out the conduction band degrees of freedom of the SIAM the impurity Green function is purely local and thus the diagrammatic representation of the self energy $\Sigma^{SIAM}(z)$ carries no spatial indices. Fig. C.1 a) shows first, second and fourth order contributions to the self energy of the SIAM. The full lines represent the non-interacting Green functions G_0^{SIAM} and the dotted lines the interaction vertex.

On the other hand Fig. C.1 b) shows the diagrammatic expansion of the lattice self energy Σ_{ij}^{lat}. As explained in Chap. 3.4 only local diagrams contribute to the self energy of a given lattice model with infinite coordination number. Thus we only need to consider a local self energy $\Sigma_{ij}^{lat} = \Sigma_{ii}^{lat}\delta_{ij}$. The straight lines here represent the non-interacting Green functions of the lattice model G_{ij}^{lat}. The dotted lines represent the interaction vertices at site i. The difference between a) and b) is that the self energy of the SIAM consists of purely local terms while the lattice self energy contains non-local virtual processes.
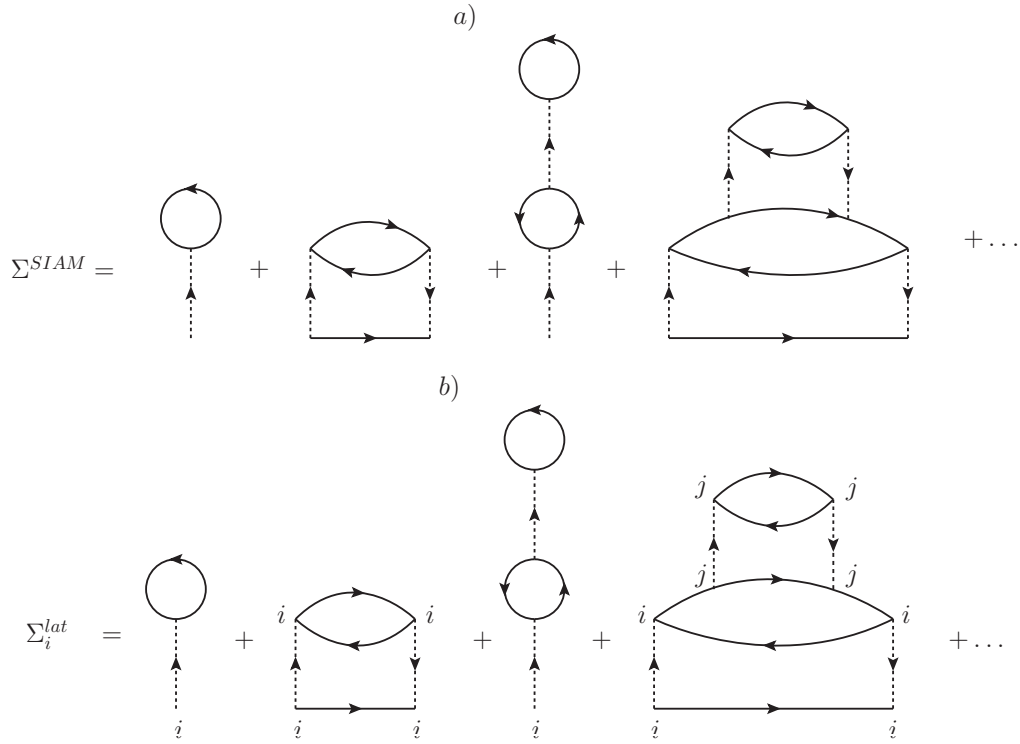
Figure C.1.: First, second and fourth order contributions to the self energy Σ^{SIAM} of the SIAM and the self energy Σ^{lat} of the given lattice model. Straight lines represent the non-interacting Green functions and the dotted lines the interaction term of the corresponding model.

From the diagrammatic evaluation it can be seen that the lattice self energy can be reproduced by the self energy of the SIAM if we replace G^{SIAM} by an appropriate effective medium Green function

$$\mathcal{G}_{ii}^{eff} = G_{ii}^{lat} + \sum_{j} G_{ij}^{lat} \Sigma_{jj}^{lat} \mathcal{G}_{ji}^{eff} - G_{ii}^{lat} \Sigma_{ii}^{lat} \mathcal{G}_{ii}^{eff} . \tag{C.2}$$

Then Eq. (C.1) applies because the first two terms on the right hand site reproduce all the non-local diagrams of the lattice and the third term corrects the over counting of the contributions of the local diagrams, which are already included in Σ^{SIAM} in Fig. C.2 a).

With Eq. (C.2) we can calculate the effective medium for a given lattice model. Assuming we have calculated the effective medium for the lattice model, we have learned in Chap. 3 that the corresponding SIAM is completely determined by the hybridization function, which can be determined using Eq. (3.11). With $\mathcal{G}^{eff}$ we can calculate the hybridization function which determines the effective SIAM for the lattice problem via

$$\Delta^{SIAM}(z) = z - \varepsilon^f - \left[\mathcal{G}^{eff}(z) \right]^{-1} .$$

The index i has been skipped because the lattice problem is translational invariant.

D. DMFT for the bipartite PAM

To solve the self-consistency equation for the bipartite PAM (Chap. 5) we adopt the method described in Appendix C, which means we have to solve

$$\mathcal{G}_{ij} = G_{ij}^f + \sum_{lj} G_{il}^f \Sigma_{ll} \mathcal{G}_{lj} - G_{ij}^f \Sigma_{jj} \mathcal{G}_{jj} \tag{D.1}$$

for the effective medium $\mathcal{G}_{ij}$ between site i and j, where G_{ij}^f is the non-interacting Green function for the f-electrons and Σ_{jj} the local self energy. The spin indices are skipped.

A Fourier transformation in i and j yields

$$\mathcal{G}_{kq} = G_{kq}^f + \underbrace{\sum_{ijl} e^{ikR_i - iqR_j} G_{il}^f \Sigma_{ll} \mathcal{G}_{lj}}_{=F_{kq}^1} - \underbrace{\sum_{ij} e^{ikR_i - iqR_j} G_{ij}^f \Sigma_{jj} \mathcal{G}_{jj}}_{=F_{kq}^2}. \tag{D.2}$$

In section D.1 the non-interacting Green function is calculated using the equations of motion (see B.3). Then, in D.2, the effective medium for sublattice A and B is calculated.

D.1. The non-interacting Green function

The full Hamiltonian for the PAM on a bipartite lattice is (see Chap. 5)

$$H = \sum_{\langle ij \rangle, \sigma} t_{ij} \, c_{i\sigma}^\dagger c_{j\sigma} + \sum_{i\sigma} \left(\varepsilon_c \, c_{i\sigma}^\dagger c_{i\sigma} + \varepsilon_f^i \, f_{i\sigma}^\dagger f_{i\sigma} + \frac{1}{2} U_i \, n_{i\uparrow}^f n_{i\downarrow}^f + V_i \, c_{i\sigma}^\dagger f_{i\sigma} + h.c. \right) \tag{D.3}$$

and the Green function for a given Hamiltonian can be calculated via the equations of motion (eom) (B.3).

In order to adopt the eom to the given Hamiltonian a Fourier transformation

$$f_{k\sigma} = \frac{1}{\sqrt{N}} \sum_j f_{j\sigma} e^{ikR_j} \qquad\qquad f_{j\sigma} = \frac{1}{\sqrt{N}} \sum_k f_{k\sigma} e^{-ikR_j} \tag{D.4}$$

is performed. And since only the non-interacting Green function is necessary, the interaction term $\sum_i U_i n^f_{i\uparrow} n^f_{i\downarrow}$ can be neglected.

$$
\begin{aligned}
H = &\sum_{k,\sigma} (\varepsilon_k + \varepsilon_c) c^\dagger_{k\sigma} c_{k\sigma} \\
&+ \sum_{kq,\sigma} f^\dagger_{k\sigma} f_{q\sigma} \sum_i \varepsilon^i_f e^{i(k-q)R_i} \\
&+ \sum_{kq,\sigma} (c^\dagger_{k\sigma} f_{q\sigma} \sum_i V_i e^{i(k-q)R_i} + h.c.)
\end{aligned}
\tag{D.5}
$$

The middle term (analogue for the last term) of Eq. D.5 can be rewritten as

$$
\sum_i \varepsilon^i_f e^{i(k-q)R_i} = \frac{\varepsilon^f_A + \varepsilon^f_B}{2} \sum_i e^{i(k-q)R_i} + \frac{\varepsilon^f_A - \varepsilon^f_B}{2} \sum_i e^{i(k-q)R_i - iQR_i}
$$

where the factor $\exp(-iQR_i)$ with $Q = (\pi, \dots, \pi)$ is responsible to choose the correct sublattice. In this case the origin of the lattice is placed in sublattice A. We define

$$
\bar{\varepsilon}^f = \frac{\varepsilon^f_A + \varepsilon^f_B}{2}, \quad \Delta\varepsilon^f = \frac{\varepsilon^f_A - \varepsilon^f_B}{2}, \quad \bar{V} = \frac{V_A + V_B}{2}, \quad \Delta V = \frac{V_A - V_B}{2}
$$

and knowing that

$$
\sum_i e^{i(k-q)R_i} = \delta_{k,q}
$$

the Fourier transformation of Eq. D.5 is

$$
\begin{aligned}
H = \sum_{k,\sigma} \Big[&(\varepsilon_k + \varepsilon_c) c^\dagger_{k\sigma} c_{k\sigma} \\
&+ \bar{\varepsilon} f^\dagger_{k\sigma} f_{k\sigma} + \Delta\varepsilon f^\dagger_{k\sigma} f_{k+Q\sigma} + (\bar{V} c^\dagger_{k\sigma} f_{k\sigma} + \Delta V c^\dagger_{k\sigma} f_{k\sigma} + h.c.) \Big].
\end{aligned}
\tag{D.6}
$$

With Hamiltonian D.6 and the eom (Eq. B.3) we can derive a system of linear equations

$$
\begin{aligned}
z \ll f_k, f^\dagger_q \gg_z &= \delta_{kq} + \bar{\varepsilon} \ll f_k, f^\dagger_q \gg_z + \Delta\varepsilon \ll f_k, f^\dagger_{q+Q} \gg_z \\
&+ \bar{V} \ll f_k, c^\dagger_q \gg_z + \Delta V \ll f_k, c^\dagger_{q+Q} \gg_z \\
z \ll f_k, c^\dagger_q \gg_z &= (\varepsilon_q + \varepsilon_c) \ll f_k, c^\dagger_q \gg_z \\
&+ \bar{V} \ll f_k, f^\dagger_q \gg_z + \Delta V \ll f_k, f^\dagger_{q+Q} \gg_z
\end{aligned}
$$

and therefrom deduce the non-interacting Green function

$$\ll f_k, f_q^\dagger \gg_z = G_{kq}^{f,A} = -G_{kq}^{1,f,A}\delta_{kq} - G_{kq}^{2,f,A}\delta_{kq+Q}$$

$$G_{kq}^{1,f,A} = \frac{(V_A^2 + V_B^2)(z_q^c + z_{q+Q}^c) + 2(\varepsilon_A + \varepsilon_B)z_q^c z_{q+Q}^c - 2V_A V_B(\varepsilon_q - \varepsilon_{q+Q}) - 4zz_q^c z_{q+Q}^c}{4z_A z_B z_q^c z_{q+Q}^c + 4V_A^2 V_B^2 - 2(z_A V_B^2 + z_B V_A^2)(z_q^c + z_{q+Q}^c))}$$

$$G_{kq}^{2,f,A} = \frac{(V_B^2 - V_A^2)(z_q^c + z_{q+Q}^c) - 2z_q^c z_{q+Q}^c(\varepsilon_A - \varepsilon_B)}{4z_A z_B z_q^c z_{q+Q}^c + 4V_A^2 V_B^2 - 2(z_A V_B^2 + z_B V_A^2)(z_q^c + z_{q+Q}^c))}$$

<div align="right">(D.7)</div>

where we introduced the abbreviations

$$z_q^c = z - \varepsilon_q - \varepsilon_c,$$

$$z_A = z - \varepsilon_A \text{ and}$$

$$z_B = z - \varepsilon_B.$$

The calculation for the Green function where the origin of the lattice is on sublattice B follows analogous to that of sublattice A:

$$\ll f_k, f_q^\dagger \gg_z = G_{kq}^{f,B} = -G_{kq}^{1,f,B}\delta_{kq} - G_{kq}^{2,f,B}\delta_{kq+Q}$$

$$G_{kq}^{1,f,B} = \frac{(V_A^2 + V_B^2)(z_q^c + z_{q+Q}^c) + 2(\varepsilon_A + \varepsilon_B)z_q^c z_{q+Q}^c - 2V_A V_B(\varepsilon_q - \varepsilon_{q+Q}) - 4zz_q^c z_{q+Q}^c}{4z_A z_B z_q^c z_{q+Q}^c + 4V_A^2 V_B^2 - 2(z_A V_B^2 + z_B V_A^2)(z_q^c + z_{q+Q}^c))}$$

$$G_{kq}^{2,f,B} = \frac{(V_A^2 - V_B^2)(z_q^c + z_{q+Q}^c) - 2z_q^c z_{q+Q}^c(\varepsilon_B - \varepsilon_A)}{4z_A z_B z_q^c z_{q+Q}^c + 4V_A^2 V_B^2 - 2(z_A V_B^2 + z_B V_A^2)(z_q^c + z_{q+Q}^c))}$$

<div align="right">(D.8)</div>

D.2. Self-consistency equation

Effective medium for sublattice A

Since the self energy Σ_{ll} is assumed to be purely local, we can rewrite F_1 and F_2 of Eq. D.2 to:

$$F_{kq}^1 = \sum_{ijl} e^{ikR_i - iqR_j} G_{il}^f \frac{1}{2}\left[\left(1 + e^{iQR_l}\right)\Sigma_A + \left(1 - e^{iQR_l}\right)\Sigma_B\right]\mathcal{G}_{lj} \qquad (D.9)$$

$$= \sum_{ijlm} e^{ikR_i - iqR_j} G_{il}^f \delta_{lm} \frac{1}{2}\left[\left(1 + e^{iQR_m}\right)\Sigma_A + \left(1 - e^{iQR_m}\right)\Sigma_B\right]\mathcal{G}_{mj} \quad (D.10)$$

In the second line we introduced an additional one, written as a sum over Kronecker-Deltas. Here the origin of the lattice is on sublattice A and $Q = (\pi, \ldots, \pi)^T$. Rewriting the Kronecker-Delta to

$$\delta_{lm} = \sum_p e^{-ip(R_l - R_m)} \qquad (D.11)$$

we get

$$F^1_{kq} = \sum_p \left(G^{f,A}_{kp} \bar{\Sigma} \mathcal{G}_{pq} + G^{f,A}_{kp} \Delta\Sigma \mathcal{G}_{p+Qq} \right), \tag{D.12}$$

$$\text{with } \bar{\Sigma} = \frac{1}{2}(\Sigma_A + \Sigma_B), \quad \Delta\Sigma = \frac{1}{2}(\Sigma_A - \Sigma_B).$$

In the same way F^2_{kq} can be calculated to

$$F^2_{kq} = G^{f,A}_{kq} \left(\bar{\Sigma}\bar{\mathcal{G}} + \Delta\Sigma\Delta\mathcal{G} \right) + G^{f,A}_{kq+Q} \left(\bar{\mathcal{G}}\Delta\Sigma + \bar{\Sigma}\Delta\mathcal{G} \right), \tag{D.13}$$

$$\text{with } \bar{\mathcal{G}} = \frac{1}{2} \left(\mathcal{G}^A + \mathcal{G}^B \right), \quad \Delta\mathcal{G} = \frac{1}{2} \left(\mathcal{G}^A - \mathcal{G}^B \right) \text{ and}$$

$$\mathcal{G}_{jj} = \begin{cases} \mathcal{G}^A, & \text{if } j \in \text{ sublattice } A \\ \mathcal{G}^B, & \text{if } j \in \text{ sublattice } B \end{cases}.$$

$$\mathcal{G}_{kq} = G^{f,A}_{kq} + \sum_p \left(G^{f,A}_{kp} \bar{\Sigma} \mathcal{G}_{pq} + G^{f,A}_{kp} \Delta\Sigma \mathcal{G}_{p+Qq} \right)$$
$$+ G^{f,A}_{kq} \left(\bar{\Sigma}\bar{\mathcal{G}} + \Delta\Sigma\Delta\mathcal{G} \right) + G^{f,A}_{kq+Q} \left(\Delta\Sigma\bar{\mathcal{G}} + \bar{\Sigma}\Delta\mathcal{G} \right) \tag{D.14}$$

From Sec. D.1 we know that the non-interacting Green function is not diagonal in momentum space, more precisely:

$$G^{f,A}_{kq} = G^{1,f,A}_k \delta_{kq} + G^{2,f,A}_{k+Q} \delta_{kq+Q} \tag{D.15}$$

$$\Rightarrow \mathcal{G}_{k0} \left(1 - G^{1,f,A}_k \bar{\Sigma} - G^{2,f,A}_{k+Q} \Delta\Sigma \right)$$
$$= \mathcal{G}_{k+Q0} \left(G^{2,f,A}_{k+Q} \bar{\Sigma} + G^{1,f,A}_k \Delta\Sigma \right) + \left(G^{1,f,A}_k + G^{2,f,A}_{k+Q} \right) \left(1 - \Sigma_A \mathcal{G}^A \right) \tag{D.16}$$

Now shifting k in Eq. D.16 to $k+Q$ and inserting the result in Eq. D.16 again and doing an inverse Fourier transformation at site 0, i.e. just a sum over k, the effective medium for sublattice A is

$$\mathcal{G}_{00} = \mathcal{G}^A = \frac{1}{\left(\sum_k \tilde{G}^A_k \right)^{-1} + \Sigma^A}, \tag{D.17}$$

where

$$\tilde{G}^A_k = \frac{\varepsilon_k V_A V_B - z_c V^2_B + z_B \left(z^2_c - \varepsilon^2_k \right)}{V^2_A V^2_B - z_c z_A V^2_B - z_c z_B V^2_A - z_A z_B (z^2_c - \varepsilon^2_k)}$$

and

$$z_A = z - \varepsilon_A - \Sigma_A$$
$$z_B = z - \varepsilon_B - \Sigma_B$$
$$z_c = z - \varepsilon_c .$$

Effective medium for sublattice B

The calculation for the effective medium for sublattice B is essentially the same as before. The only difference now is that the origin of the lattice is chosen to be on sublattice B. Thus analogue to Eq. D.10 we get

$$
F_{kq}^1 = \sum_{ijlm} e^{ikR_i - iqR_j} G_{il}\delta_{lm}\frac{1}{2}\left[\left(1 - e^{iQR_m}\right)\Sigma_A + \left(1 + e^{iQR_m}\right)\Sigma_B\right]\mathcal{G}_{mj}
$$

$$
= \sum_p \left(G_{kp}\bar{\Sigma}\mathcal{G}_{pq} - G_{kp}\Delta\Sigma\mathcal{G}_{p+Qq}\right) \quad \text{and}
$$

$$
F_{kq}^2 = G_{kq}\left(\bar{\Sigma}\bar{\mathcal{G}} + \Delta\Sigma\Delta\mathcal{G}\right) - G_{kq+Q}\left(\bar{\mathcal{G}}\Delta\Sigma + \bar{\Sigma}\Delta\mathcal{G}\right) .
$$

And the effective medium for sublattice B finally is

$$
\mathcal{G}^B = \frac{1}{\left(\sum_k \tilde{G}_k^B\right)^{-1} + \Sigma^B} , \tag{D.18}
$$

where

$$
\tilde{G}_k^B = \frac{\varepsilon_k V_A V_B - z_c\, V_A^2 + z_A\left(z_c^2 - \varepsilon_k^2\right)}{V_A^2 V_B^2 - z_c z_A V_B^2 - z_c z_B V_A^2 - z_A z_B(z_c^2 - \varepsilon_k^2)} .
$$

Bibliography

[1] K. Andres, J. Graebner and H. R. Ott, *Phys. Rev. Lett.*, **35**, 1779, (1975)

[2] F. Steglich, J. Aarts, C. D. Bredl, W. Leike, D. E. M. W. Franz and H. Schäfer, *Phys. Rev. Lett.*, **43**, 1892, (1976)

[3] J. Kondo, *Prog. Theo. Phys.*, **28**, 772, (1962)

[4] J. Kondo, *Prog. Theo. Phys.*, **32**, 37, (1964)

[5] P. Nozières, *Ann. Phys. Fr.*, **10**, 19, (1985)

[6] P. Nozières, *Eur. Phys. B*, **6**, 447, (1998)

[7] A. Altland and B. Simons, *Condensed Matter Field Theory*, Cambridge University Press, first edition, (2006)

[8] A. Benlagra, L. Fritz and M. Vojta, *Phys. Rev. B*, **84**, 075126, (2011)

[9] T. Pruschke, R. Bulla and M. Jarrell, *Phys. Rev. B*, **61**, 12799, (2000)

[10] S. Burdin and V. Zlatić, *Phys. Rev. B*, **79**, 115139 (2008)

[11] W. J. de Haas, J. H. de Boer and G. J. van den Berg, *Physica*, **1**, 1115, (1934)

[12] P. W. Anderson, *Phys. Rev.*, **124**, 41, (1961)

[13] J. Schrieffer, P. Wolff, *Phys. Rev.*, **149**, 491, (1966)

[14] A. C. Hewson, *The Kondo Problem to Heavy Fermions*, Cambridge University Press, (1993)

[15] R. Bulla, *Entwicklung neuer Methoden zur Untersuchung des Anderson-Modells*, Dissertation, Universität Regensburg, (1994)

[16] K. G. Wilson, *Rev. Mod. Phys.*, **47**, 773, (1975)

[17] S. Ma, *Rev. Mod. Phys.*, **45**, 589, (1973)

[18] H. R. Krishna-murthy, J. W. Wilkins and K. G. Wilson, *Phys. Rev. B*, **21**, 1003, (1980)

[19] C. M. Hurd, *Phys. Rev. Lett.*, **18**, 1127, (1967)

[20] H. R. Krishna-murthy, J. W. Wilkins and K. G. Wilson, *Phys. Rev. B*, **21**, 1044, (1980)

[21] H. O. Frota and L. N. Oliveira, *Phys. Rev. B*, **33**, 7871, (1986)

[22] O. Sakai, Y. Shimizu and T. Kasuya, *J. Phys. Soc. Jpn.*, **58**, 3666, (1989)

[23] T. A. Costi and A. C. Hewson, *Physica B Condensed Matter*, **163**, 179, (1990)

[24] T. A. Costi and A. C. Hewson, *Journal of Physics Condensed Matter*, **5**, L361, (1993)

[25] R. Bulla, T. A. Costi, T. Pruschke, *Rev. Mod. Phys.*, **80**, 395, (2008)

[26] R. Bulla, T. Pruschke and A. C. Hewson, *J. Phys.: Condens. Matter*, **9**, 10463, (1997)

[27] W. C. Oliveira and L. N. Oliveira, *Phys. Rev. B*, **49**, 11986, (1994)

[28] V. L. Campo, Jr. and L. N. Oliveira, *Phys. Rev. B*, **72**, 104432, (2005)

[29] R. Bulla, H.-J. Lee, N.-H. Tong and M. Vojta, *Phys. Rev. B*, **71**, 045122, (2005)

[30] T. A. Costi, A. C. Hewson and V. Zlatić, *J. Phys.: Condens. Matter*, **6**, 2519, (1994)

[31] R. Bulla, T. A. Costi and D. Vollhardt, *Phys. Rev. B*, **64**, 045103, (2001)

[32] W. Hofstetter, *Phys. Rev. Lett.*, **85**, 1508, (2000)

[33] R. Bulla, A. C. Hewson and T. Pruschke, *J. Phys.: Condens. Matter*, **10**, 8365, (1998)

[34] W. Metzner, D. Vollhardt, *Phys. Rev. Lett.*, **62**, 324, (1989)

[35] E. Müller-Hartmann, *Z. Phys. B*, **74**, 407, (1989)

[36] E. Müller-Hartmann, *Z. Phys. B*, **76**, 211, (1989)

[37] W. Metzner, *Z. Phys. B*, **77**, 253, (1989)

[38] A. Georges, G. Kotliar, W. Krauht, M. J. Rozenberg, *Rev. Mod. Phys.*, **68**, 13, (1996)

[39] D. Vollhardt, *ArXiv:1004:5069v1*, (2010)

[40] K. Yosida, *Theory of Magnetism*, Springer series in solid state sciences, (1996)

[41] J. E. Hirsch, R. M. Fye *Phys. Rev. Lett.*, **56**, 2521, (1986)

[42] G. Sordi, A. Amaricci, M. J. Rozenberg *Phys. Rev. Lett.*, **99**, 196403, (2007)

[43] G. Sordi, A. Amaricci, M. J. Rozenberg *Phys. Rev. B*, **80**, 035129, (2009)

[44] E. Gull, P. Werner, A. Millis, M. Troyer *Phys. Rev. B*, **76**, 235123 (2007)

[45] J. Kitagawa, N. Takeda, M. Ishikawa *J. Alloys Compounds*, **256**, 48, (1997)

Acknowledgements

I would like to use the last words to thank all persons who supported me while working and writing on my thesis.

First of all, I would like to thank my thesis supervisor Priv.-Doz. Dr. *Ralf Bulla* for giving me the opportunity to work on a versatile and fascinating PhD project in Cologne. I also want to thank him for his guidance, always being available to answer urgent questions, for fruitful discussions about physical intriguing problems and of course for providing me with all the essentials I needed for my progress.

Special thanks goes also to Prof. Dr. *Simon Trebst*, who agreed to be the second advisor for this thesis. In this sense, I also want to thank Prof. Dr. *Markus Grüninger* as chairman of the examination committee and the assessor Priv.-Doz. Dr. *Markus Garst*.

Furthermore, I want to thank Dr. *Andrew Mitchell* for helping me during the last two years of my PhD with uncountable discussions, explanations and suggestions for my projects. Similarly I want to thank *Etienne Gärtner* for fertile discussions and advice, and especially for proof reading my thesis.

My gratitude as well to all other colleagues I did or did not share a room with, for the nice and friendly atmosphere, their patience and helpfulness and also the great deal of fun we enjoyed together. Here especially *Alexander Wollny, Mario Zacharias, Stephan Mandt, Tobias Meng, Carolin Küppersbusch, David Rasch, Karin Everschor-Sitte, Matthias Sitte, Stefan Buhrandt, Mascha Baedorf, Robert Bamler, Christoph Schütte, Akos Rapp, Lars Fritz, Michael Becker, Johannes Waizner* and many more.

Last but not least, I thank my *parents*, my sister *Judith* and all of my *friends* for making the last three years such a great time.

Erklärung

Ich versichere, dass ich die von mir vorgelegte Dissertation selbständig angefertigt, die benutzten Quellen und Hilfsmittel vollständig angegeben und die Stellen der Arbeit – einschließlich Tabellen, Karten und Abbildungen –, die anderen Werken im Wortlaut oder dem Sinn nach entnommen sind, in jedem Einzelfall als Entlehnung kenntlich gemacht habe; dass diese Dissertation noch keiner anderen Fakultät oder Universität zur Prüfung vorgelegen hat; dass sie – abgesehen von unten angegebenen Teilpublikationen – noch nicht veröffentlicht worden ist sowie, dass ich eine solche Veröffentlichung vor Abschluss des Promotionsverfahrens nicht vornehmen werde. Die Bestimmungen der Promotionsordnung sind mir bekannt. Die von mir vorgelegte Dissertation ist von Priv.-Doz. Dr. Ralf Bulla betreut worden.

Köln, 26. September 2012
Lucas Hollender

Curriculum Vitae

PERSÖNLICHE ANGABEN

Name: Lucas Hollender

Anschrift: Koelhoffstr. 1

50676 Köln

Deutschland

Staatsangehörigkeit: deutsch

Geburtsdatum und -ort: 01.12.1982 in Köln

Familienstand: ledig

BERUFSPRAXIS

07/2009 – 10/2012	Wissenschaftlicher Mitarbeiter am Institut für theoretische Physik an der Universität zu Köln
	Promotionsstudium am Institut für theoretische Physik an der Universität zu Köln

SCHULE & STUDIUM

06/2009	Diplom Physik (1,8)
10/2003 – 06/2009	Studium der Physik Universität zu Köln
10/2002 – 09/2003	Studium der Physik Rheinische Friedrich-Wilhelms-Universität Bonn
08/1999 – 05/2002	Abitur (2,3) Ernst-Mach Gymnasium in Hürth
08/1993 – 07/1999	Hildegard-von-Bingen Gymnasium in Köln

Köln, 26. September 2012